UNIVERSITY OF OKLAHOMA

GRADUATE COLLEGE

INVESTIGATION OF FAULTING PROCESSES OF TWO M5 EARTHQUAKE SEQUENCES IN OKLAHOMA

A THESIS

SUBMITTED TO THE GRADUATE FACULTY

in partial fulfillment of the requirements for the

Degree of

MASTER OF SCIENCE

By

COLIN PENNINGTON
Norman, Oklahoma
2017

INVESTIGATION OF FAULTING PROCESSES OF TWO M5 EARTHQUAKE SEQUENCES IN OKLAHOMA

A THESIS APPROVED FOR THE
CONOCOPHILLIPS SCHOOL OF GEOLOGY AND GEOPHYSICS

BY

_____
Dr. Xiaowei Chen, Chair

_____
Dr. Norimitsu Nakata

_____
Dr. Brett Carpenter

Acknowledgements

I would like to thank my family for their endless encouragement and support throughout my time at the University of Oklahoma. I would also like to thank the Oklahoma Geologic Survey, and the United States Geological Survey, for the use of their earthquake catalogs. I would especially like to thank Nicole McMahon for sharing her dataset with me. I would also like to thank my committee members for their patience in answering my many questions, especially my advisor Xiaowei Chen.

Table of Contents

List of Tables

List of Figures

Abstract

I investigate the stress interaction inside different earthquake clusters to better understand the factors that might drive and control seismicity. I examine a catalog of 6226 events that have been relocated using the GrowClust method. The relocated earthquakes show that the Prague earthquake sequence occurred on a number of anastomosing faults, I also find that the fault propagates up into the Arbuckle formation and shows a pattern that mimics observed structure in the Hunton formation. I then examine the stress drop of the Prague earthquake sequence and find a median stress drop of 2.21 MPa, with low stress drop occurring in the shallow region of 1.8 to 3 km, as well as higher overall stress drops located on the fault activated by the aftershock. I then examine the Pawnee cluster, specifically within the Watchorn, Labette, and Sooner Lake fault systems and the effect of precursory activities on the September 3, 2016 M5.8 Pawnee earthquake. I obtain fault plane solutions for earthquakes with sufficient azimuthal coverage using the HASH algorithm, and then performed Coulomb stress analysis on both seismogenic faults and individual nodal planes. Our results found that the three M≥3.0 foreshocks exerted a cumulative Coulomb stress change increase of 68 to 198 kPa at the mainshock hypocenter and promoted failure for most aftershocks within 2 km of the mainshock. The Coulomb stress change of 500 kPa exerted by the mainshock also promoted failure for most aftershocks within the conjugate fault system. The combined results of these studies suggest that earthquake interaction should be fully considered in hazard assessment for induced seismicity.

Chapter 1: Introduction

The seismicity of Oklahoma historically has been more active than other regions in the central United States, with a M7 earthquake occurring along the Meers fault 1100 years ago [*Luza et al.*, 1987]. In recent history, Oklahoma has experienced five M5 events. The earliest event of these was the 1952 M5.5 El Reno earthquake, then there was a 59-year gap before the next event which was the Mw 5.7 Prague earthquake in 2011. This was the first event that indicated that it might have been induced by injection [*Keranen et al.*, 2013a]. The last three events occurred in 2016. The first was the Mw 5.1 Fairview earthquake preceded by a series of M4 earthquakes, and then there was the largest event in state seismic network history the Mw 5.7 Pawnee earthquake, which had no M4 earthquakes preceding or following its rupture. This event was followed by the Mw 5.0 Cushing earthquake that was proceeded by five magnitude Mw 4+ events, however it has been a year since the last foreshock occurred.

The reason for the rapid increase in seismicity after the Prague earthquake has been debated and the common consensus is that the seismicity can be linked to the injection of wastewater into the Arbuckle formation [*Keranen et al.*, 2014; *McGarr*, 2014; *Murray*, 2014]. The Arbuckle formation rests on top of the basement rock, is highly permeable, and is under-pressured throughout Oklahoma making it the preferred formation to inject waste water [*Murray*, 2014]. The seismicity in Oklahoma, when compared to the injected volume of waste water, shows an average time delay of 300 days (Figure 1) *Chen et al.*, [2017 in review].

Even though all the largest earthquakes have been linked to injection, they exhibit differences in their spatial-temporal response to injection compared to smaller

earthquake clusters that sometimes show clear diffusion patterns. When comparing different earthquake sequences, the varied nature of each sequence becomes apparent, making it a challenge to properly understand each cluster and the dynamics that shaped it. The Fairview cluster had multiple M4+ foreshocks and aftershocks that occurred around the eventual Mw5.1 mainshock [*Yeck et al.*, 2016b]. The Prague earthquake sequence also had a similar pattern with a Mw 4.1 earthquake a year before and a Mw 4.8 earthquake one day before the mainshock. It was followed by a Mw 4.8 magnitude aftershock [*Keranen et al.*, 2013b]. The Pawnee earthquake sequence had no M4+ foreshock or aftershocks, which makes it quite unusual when compared to the other sequences in Oklahoma.

The earthquake sequences vary in how they respond to injection as well. The Prague earthquakes sequence is possibly the most studied of the sequences next to the Pawnee earthquake, but given the lack of well data and detailed injection history, as well as the limited seismic network when the injection began, it is difficult to understand how Prague initially responded to injection. There are multiple different theories that will be discussed in the next section.

Fairview however shows a clear response to injection (Figure 2b). *Yeck et al.*, [2016b] examined the sequence and found that it responded to a group of wells to its northeast and showed a delayed response of about 4 years. The Pawnee earthquake showed a similar response to injection. Its response time in the years preceding the mainshock was 643 days, however in the months preceding the mainshock the response time dropped to almost 0 [*Chen et al.*, 2017 in review], indicating a change in the response of injection fluid in the region.

All three of these sequences are quite complex and are different from one another in many ways. To understand all the complex interactions observed in these sequences, it is important to try and understand each component they are reacting to. The Prague earthquake sequence has been the subject of a few studies that revolve around its reaction to injection, the Coulomb Stress interactions inside of the cluster, stress drop estimates, and a finite fault model. [*Keranen et al.*, 2013b; *McGarr*, 2014; *Sumy et al.*, 2014, 2017; *Sun and Hartzell*, 2014; *Boyd et al.*, 2017; *Yenier et al.*, 2017] In this paper, I will consider both the Prague and Pawnee earthquake sequences and try to determine the stress interactions occurring before and after their respective mainshocks. For the Prague earthquake sequence, I will examine the fault structures observed from earthquake relocation, and calculate stress drop for the overall cluster to better understand the hazard it and similar events might pose. For the Pawnee earthquake sequence, I will examine the Coulomb stress interactions for the sequence to determine if its foreshocks might have contributed to the critical stress state of the fault that the mainshock ruptured along.

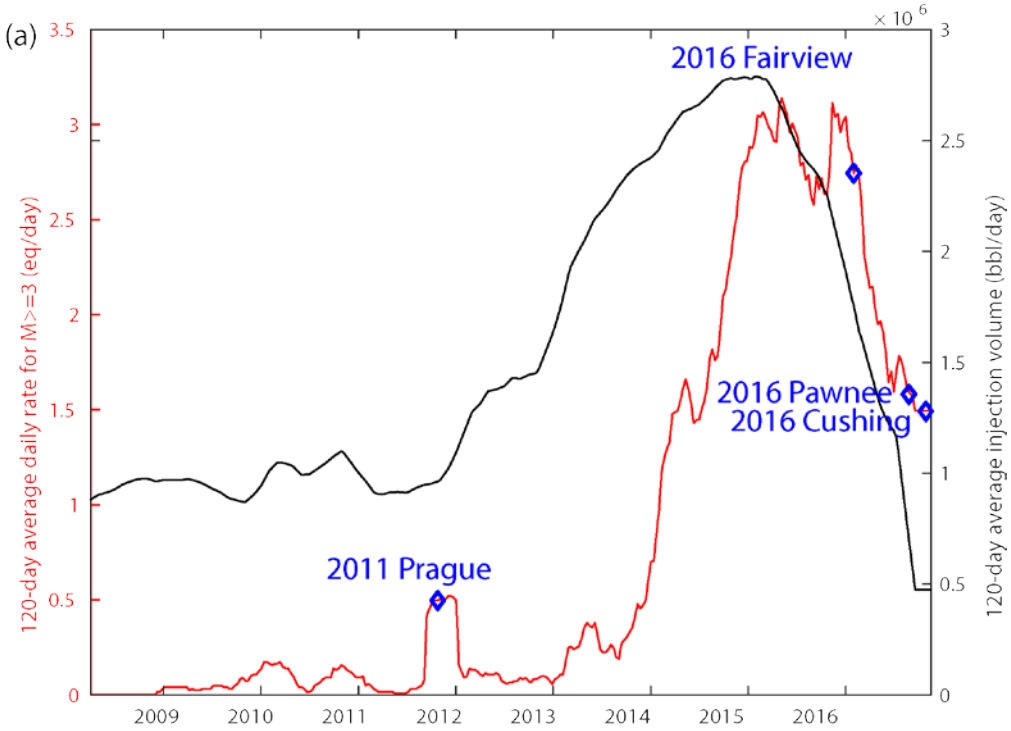

Figure 1. Overview of the relationship between injection and seismicity for Oklahoma. Black line shows 120-day average of state wide injected volume, while the red line shows as 120-day average for M>=3 earthquakes. The blue diamonds indicate major earthquakes. [*Chen et al.*, 2017 in review]

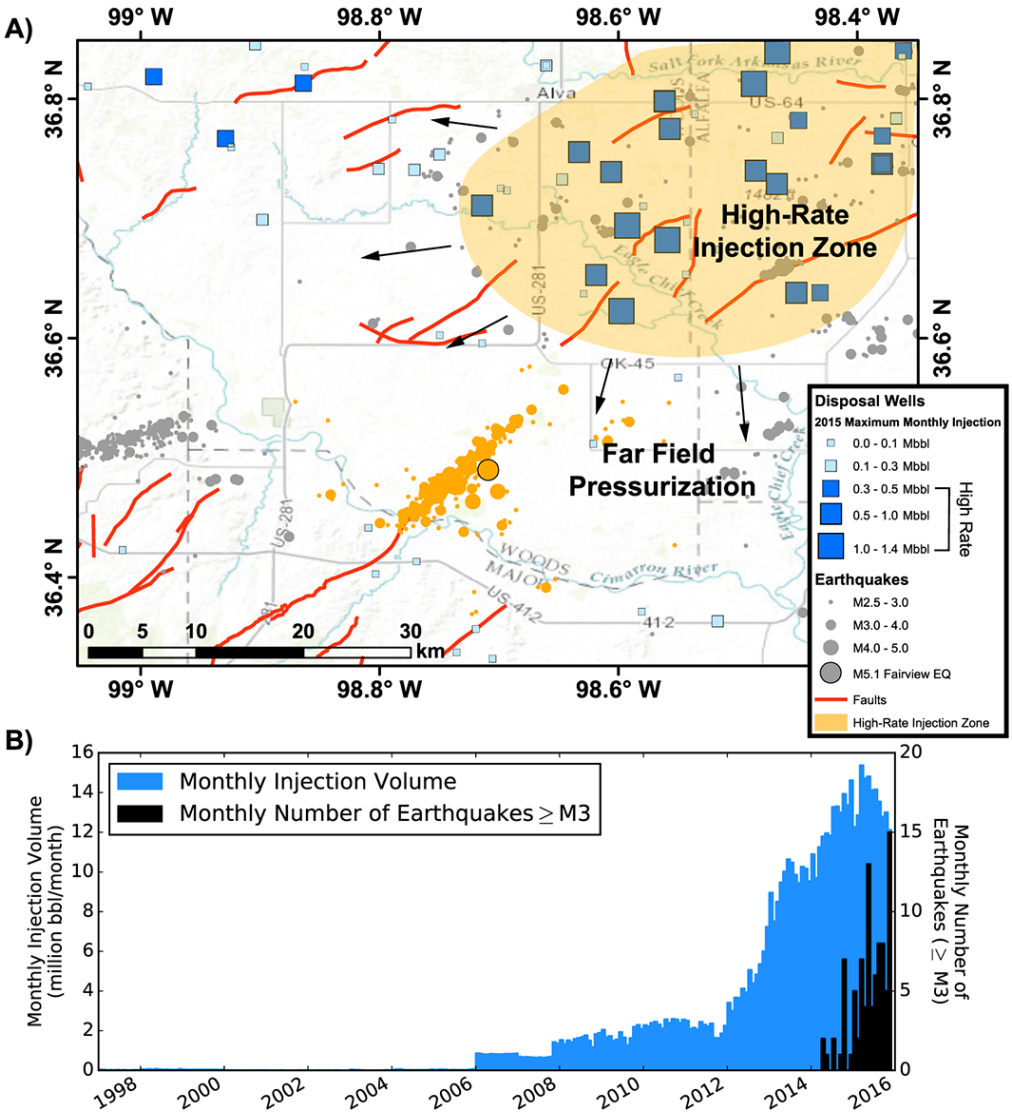

Figure 2. (a) Overview of Fairview region with injection wells shown in blue. Gray circles show earthquakes with the orange ones beloning to the fairview sequnce. (b) Cumulative monthly injection rate of 79 wells operating in the Fairview sequence region, shown in blue. For the same region the earthquakes are shown in black. [*Yeck et al.*, 2016c]

Chapter 2: Past Studies of Prague

The Prague earthquake sequence occurred along the Wilzetta fault system in Oklahoma that was formed due to deformation related to activity associated with the Nemaha Ridge and Ozark uplift [*Way*, 1983]. It contains both normal faults and transverse faults throughout the fault system that extends 200 km from the SW to the NE. The fault system shows up to 600ft of displacement for the normal faults that trend from the NE to the SW. The E-W faults show displacement of 20-100ft of displacement in the Hunton group. The observed displacement for both fault trends increases with depth, so the displacement in the basement could be greater than the amounts observed in the shallow formation [*Way*, 1983]. The Hunton group is seated at 1.04-1.09 km and the Arbuckle group is located 1.3 to 2.2 km of depth, with the top of the basement in the area varying from 1.8-2.2 km [*Keranen et al.*, 2013]. The Arbuckle group and the Hunton group have both been used for wastewater disposal starting in 1993.

The first recorded major earthquake for the area was a M4.1 event that occurred in 2010. Prior to this event, no earthquakes had been recorded in the area, however there were only 8 stations in Oklahoma before 2010, so seismicity could have been present, but below the detection threshold. The M4.1 earthquake was examined by *van der Elst et al.*, [2013] and they found that it could have been dynamically triggered by surface waves from the 2010 M8.8 Maule Chile megathrust event. They proposed that this could be an indication that the Wilzetta fault area and the area where the future main shock would occur was critically stressed and primed for failure. This critically stressed fault failed on November 5, 2011 with a Mw 4.8 earthquake along a fault with a strike and dip of 207° and 73° with right lateral strike slip motion (Figure 3). It was followed

less than 24 hours later by the second largest event in instrumented Oklahoma earthquake history, a Mw 5.7 event that was found to have occurred along a fault with a right lateral strike slip motion which had a strike of 324° and a nearly vertical dip of 88° [*McNamara et al.*, 2015]. This event led to the destruction of 16 homes, the buckling of pavement and injuries to two people. It was then followed two days later by a Mw 4.8 aftershock which ruptured along a new fault that had a strike of 91° and dip of 74° and a left-lateral motion [*McNamara et al.,* 2015]. 24 hours after the mainshock, 3 more seismometers were deployed followed by 12 more in the next five days [*Keranen et al.,* 2013]. All stations remained in the area until the end of December 2011.

Triggering of the Prague Earthquake Sequence

From the gathered data, multiple studies were done to try and understand what triggered the Prague earthquake sequence. The first study to do an in depth examination of the Prague earthquake sequence was *Keranen et al.,* [2013]. They hypothesized that injection into a subsurface compartment of the Hunton group that had previously contained oil, surpassed the amount of oil extracted from the group. This led to an increase in formation pressure, which caused the failure of the fault sealing the reservoir producing the Mw 4.8 foreshock (Figure 3). The Coulomb stress change from the foreshock then led to the mainshock causing the cascading failure of the fault system (Figure 4) [*Sumy et al.,* 2014].

Two other hypotheses were introduced about the possible cause of the Prague earthquake sequence. One was that the Prague mainshock was a natural event, which was introduced by *Keller and Holland,* [2013]. They supported this idea by examining 3D seismic information that showed that the sealed group referenced by [*Keranen et al.*,

2013b] was not actually fault bound, so pressure would not have built up in the reservoir (The 3D data has not been released to the public, so confirmation of this interpretation cannot be made). They supported their assessment further by stating that Oklahoma has had more than ten M4.0 or greater earthquakes since the El Reno earthquake, so the magnitude 5.7 at Prague would be consistent with the Gutenberg-Richter relationship. The second hypothesis proposed by *McGarr*, [2014] was that the earthquake sequence was the result of about 1.2e7 m^3 of wastewater injected in the vicinity of the epicentral zone by 5 high-volume injection wells and not just the two selected by *Keranen et al.*, [2013]. The large injections happened in the Arbuckle group, which is a highly permeable and porous zone [*Murray*, 2014]. The amount injected also aligns with the observed injected volume and moment relationship *McGarr*, [2014] observed for other clusters.

The next investigation into the Prague earthquake sequence considered the Coulomb stress transfer of the $M \geq 4.8$ events by *Sumy et al.*, [2014]. This study found that the foreshock, mainshock, and aftershock promoted failure for ~60% of the events where focal mechanism solutions were determined. The Mw 4.8 foreshock was found to promote failure for the Mw 5.7 mainshock rupture plane, this was interpreted as evidence that the foreshock, which was likely triggered by fluid injection, lead to the cascading failure of the rest of the fault (Figure 4). They found that the aftershock hypocenter locations experienced a negative Coulomb stress change from both the foreshock and mainshock as well most events that fall on the East-West oriented fault (Figure 4 b, c).

Stress Drop Observations for Prague

To understand more about slip of the mainshock *Sun and Hartzell*, [2014] constructed a finite-fault slip model of the Mw 5.7 event using a linear least squares method. They created the model by using 6 aftershock events recorded at 21 regional stations to create empirical Green's functions (EGFs). The solution they found indicates three stages of faulting. First at the hypocenter, then at two large slip patches to the southwest and northeast of the hypocenter, and finally a diffuse slip over the entire fault (Figure 5 b, c). From this model, they estimated and average static stress drop of 1.6 MPa over the entire fault and 9 MPa for the mainshock. This finding is considerably lower than other values found on the east coast, specifically the Mw 5.8 Mineral, Virginia earthquake, which had an average static stress drop 15 MPa to 25 MPa (depending on the model used) over the entire fault [*Hartzell et al.*, 2013]. They hypothesize that the diffuse slip seen in the model, as well as the lower stress drop observed at Prague compared to the Mineral earthquake, could be evidence of injection playing a role in Prague mainshocks rupture.

There were multiple investigations into the stress drop of the Prague earthquake sequence. A study that examined the ground motion for the Prague earthquake sequence by *Yenier et al.*, [2017] found that the largest magnitude events in the Prague sequence, and the events following the initial aftershock decay sequence, have similar source parameters to natural events in the central and eastern North America (CENA). The only events that they observed lower stress drop for were the aftershocks (Figure 6). They posit that the common assumption that induced events have lower stress drop and therefore produce lower ground motions is not supported by their analysis.

A recent study by *Boyd et al.*, [2017] estimated stress drop using spectral ratios. They obtained stress drop estimates for 1121 events across the US. They found stress drops ranging from 2.6-36 MPa, 1.0-7.9 MPa, 0.6-5.6 MPa for the eastern, western, and central United States, respectively (Figure 7). For the Prague earthquake, specifically they found a stress drop of 2.0 to 2.8 MPa for the mainshock. Regarding stress drop, they found that induced mainshocks are no different than tectonic events when the calculated stress drop was scaled for depth of 10 km, strike slip focal mechanism, and a constant moment of 1×10^{17} N·m. The correction for depth was obtained by multiplying the stress drop by the ratio of vertical stress at 10 km of depth to the vertical stress at the depth of the measurement. The correction to strike slip was done by correcting for the trend observed of increasing stress drop with rake (increasing from normal to strike slip and then to reverse). To correct all events to a common moment of 1×10^{17} N·m, they multiplied the stress drop by the ratio of the desired common moment of 1×10^{17} N·m to the measured moment raised to the power of 0. After these corrections are applied, they observed that aftershock stress drops for events within central Oklahoma are half of those observed in the western and eastern United States, but that this difference is barely significant given the standard deviation and that such variance could just be an artifact. The main difference between induced and the natural earthquakes they observe is that they occur at a shallower depth, which will increase ground shaking in the area 1-10 km away from the epicenter and decrease it at distance ranges of 10-100 km.

The most recent study that examined the stress drop of the Prague earthquake sequence was done by *Sumy et al.*, [2017] using the method of *Neighbors et al.*, [2017].

They determined stress drops for 87 events, which ranged from of 0.005-4.8 MPa with a median of 0.2 MPa (Figure 8). They found that stress drop correlates with depth and magnitude, and a trend of increasing stress drop over time. They interpret the overall low median stress drop to mean that the Wilzetta fault segment that the earthquake cluster occurred on possibly failed due to high pore fluid pressures related to nearby wells.

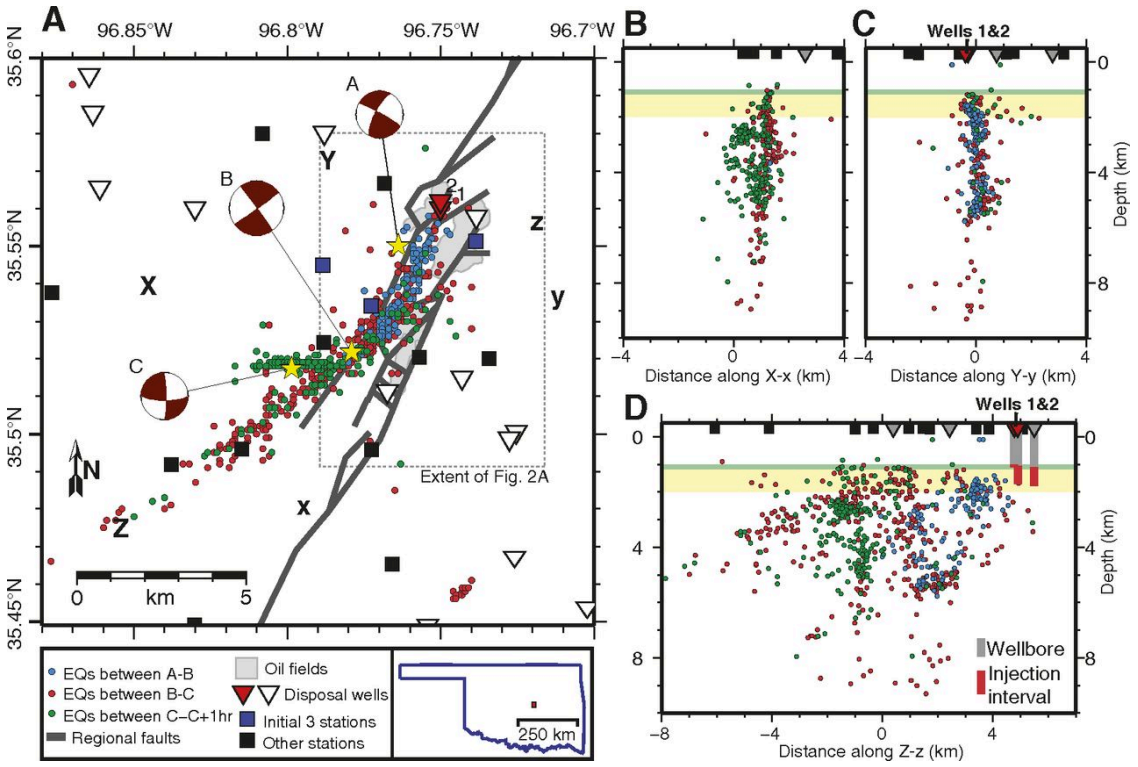

Figure 3. (a) Prague earthquake cluster with EQ plotted in color for when they occurred. Reference legend for and explanation of all items. (b-d) Cross sections of seismicity projected from within 4 km of plane of each section. Depths are relative to sea level. Land elevation is ~300 m. [*Keranen et al.*, 2013b]

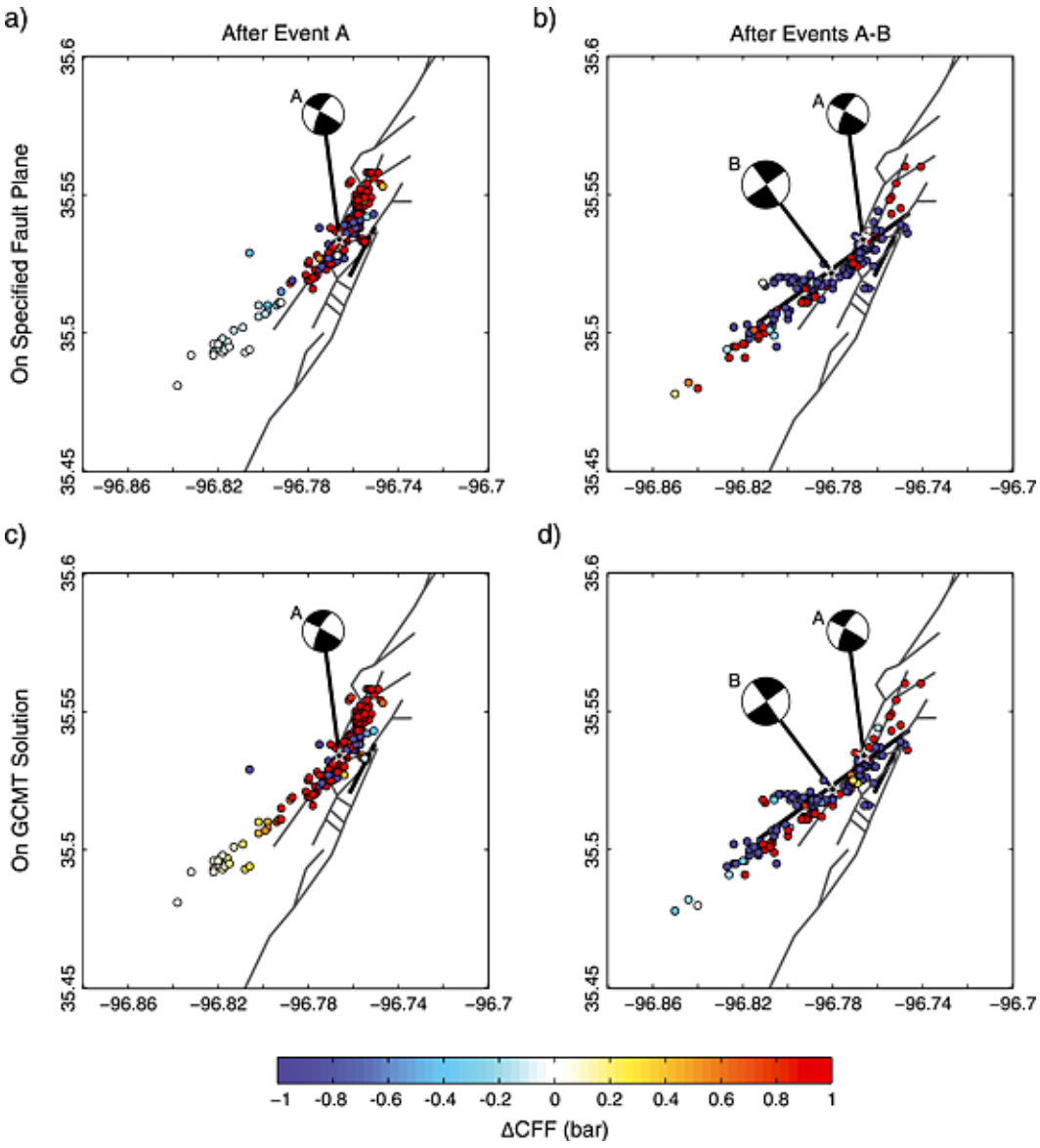

Figure 4. Coulomb stress change is mapped on specified fault planes on the aftershocks that follow (a) The 4.8 foreshock (Event A) and (b) the Mw 5.8 mainshock. (c) Coulomb stress change on the aftershock GCMT solution of aftershocks of event A. (d) The aftershocks of event B on the GCMT solution of event C.[*Sumy et al.*, 2014]

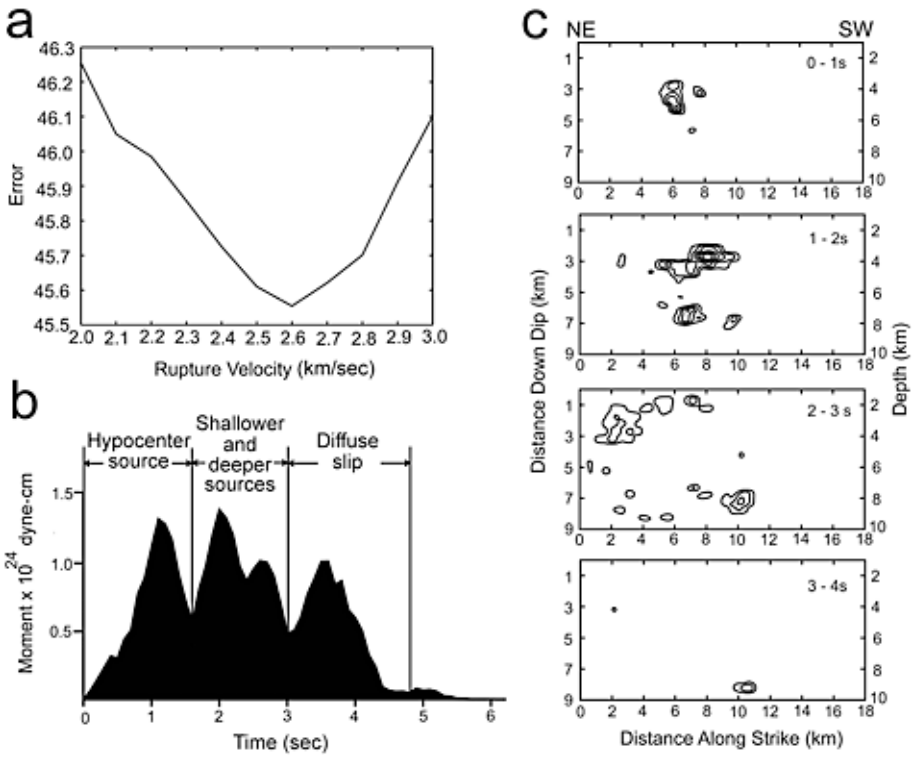

Figure 5. (a) Waveform fitting error measured as Euclidian norm verse rupture velocity using one time slice. (b) Moment rate function for slip model. Three phases of ruptured are identified. (c) Rupture time history at 1s timer intervals with a slip contour of 10 cm.[*Sun and Hartzell*, 2014]

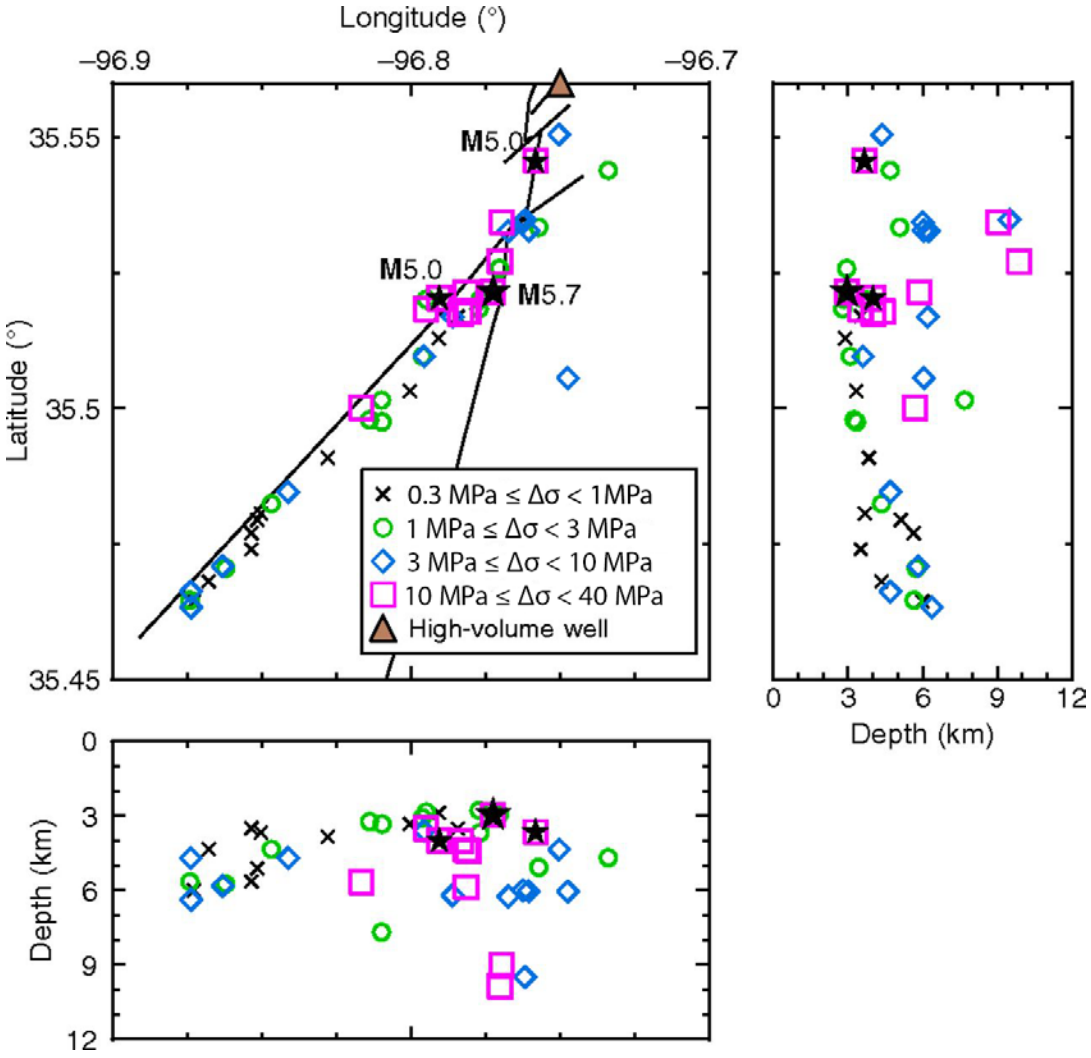

Figure 6. Spatial distribution of stress parameters for the induced Prague sequence. The locations of mainshocks are shown as stars. Wilzetta fault system is shown as black lines.[*Yenier et al.*, 2017]

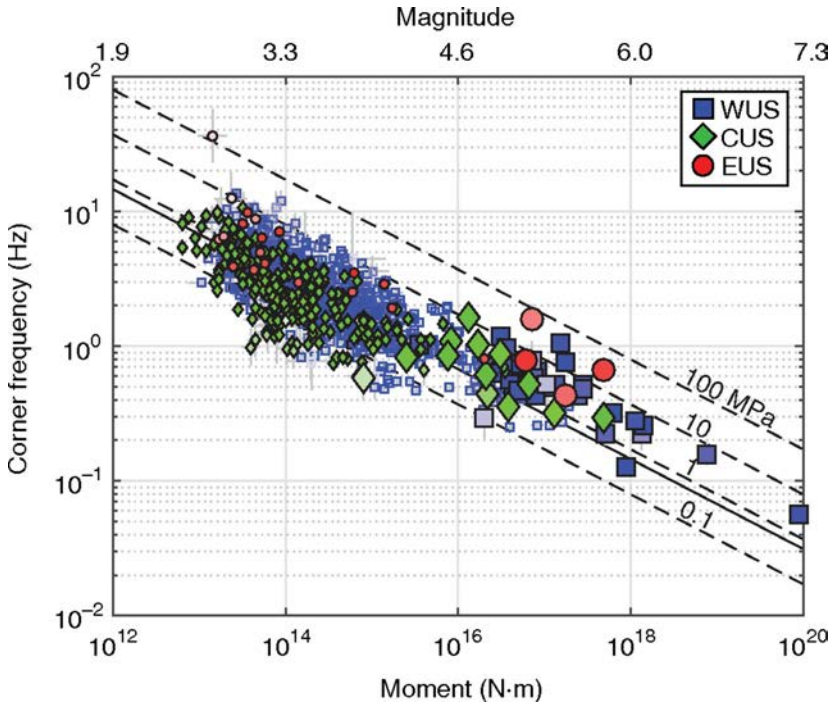

Figure 7. Results from Boyd. Corner frequency versus moment. Squares are western US events, diamonds are central US, and circles are eastern US events. Large symbols are mainshocks and small symbols are foreshocks and aftershocks. The saturation is inversely proportional to uncertainty. WUS are shown in outline only, vertical and horizontal bars represent uncertainty and are in many cases the same size as the symbol.[*Boyd et al.*, 2017]

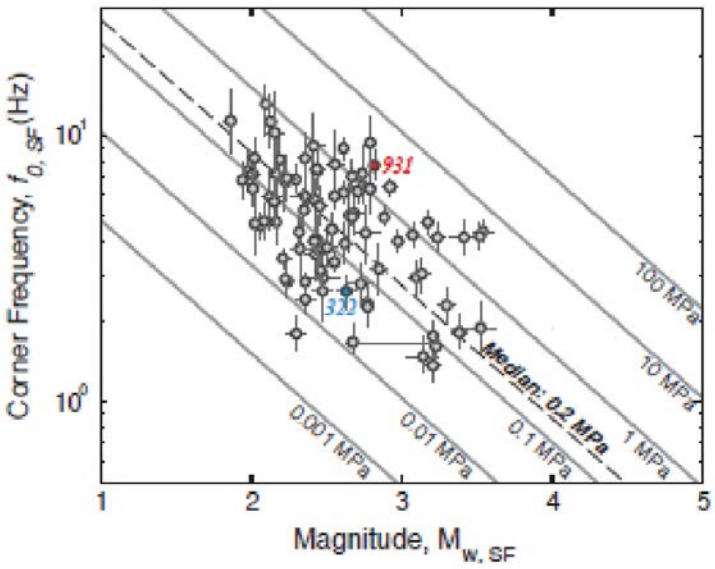

Figure 8. *Sumy et al.*,[2017]stress drop results. Corner frequency is on the vertical axis and moment magnitude is on x axis. Bars around events represent 10th and 90th percentiles from 500 bootstraps.[*Sumy et al.*, 2017]

Chapter 3: Prague Fault Interpretation

In order to construct a detailed view of the seismicity at Prague, I first collect all the events from the Oklahoma Geologic Survey (OGS) earthquake catalogue that fall within an area of 35.4 to 35.6 latitude and -96.9 to -96.7 longitude. This catalog is then combined with a subspace detected catalog from *Mcmahon et al.*, [2017, in review], which has a larger number of shallow events. This addition will assist in the understanding of seismicity in the sedimentary layers above the basement. To avoid having duplicate earthquakes in the catalog, each earthquake is first compared between the two catalogs and any event that occurs within 1 second of an event in the OGS catalog is considered a possible duplicate and is discarded, producing a merged catalog of 6399 events with 742 being from OGS and 5446 being from the subspace detected catalog. The subspace detected events only contained arrival times for the shear wave, so a phase picker [*Li and Peng*, 2016] that utilizes a 1D velocity from *Keranen et al.*, [2013] and SNR detector is used to correct the current picks as well as locating accurate P arrival times. Using these arrival times, I then obtain precise differential times using waveform cross-correlation between each event and all the other events based on a time window of 0.5 seconds before and 1 sec after the picked arrival time (or a predicted arrival time from a 1D velocity model) between 1 and 10Hz. Only pairs with a cross correlation coefficient ≥ 0.7 from at least 4 stations are used in this relocation. Both catalog differential times and waveform cross-correlation derived differential time are used in the program GrowClust [*Trugman and Shearer*, 2017b] to obtain a relocation for 2846 out of our original catalog of 6399.

From this relocation, many new features of the Prague fault system can be identified (Figure 9). Instead of the faults being long linear segments, as was the case in the previous locations, the relocation reveals discontinuous anastomosing fault segments. They still form different segments that I will refer to as SWF (South -West Fault), NEF (Northeast Fault), NF (North Fault) and EWF (East-West Fault). The SWF appears to be made up of 4 different segments with the northern most segment having two parallel faults that split apart from the bend before rejoining into one fault 2 km later. These segments have a strike of 54 degrees and nearly vertical dips of 89 degrees. The EWF is the segment that was activated after the M 4.8 aftershock and shows two segments with a strike of 80 degrees. The NF segment has two segments contained inside of it with the southern segment having a strike of 17 and the northern segment with a strike of 19. The final segment is more diffuse in nature but it has a general strike of 54. Examining these fault segments in cross section view (Figure 10), I observe that there is a cluster of shallow events ranging in depth from 1.8 to 2.3 km (Figure 10 a, b, e). Figure 10 (d) shows that the shallow events are located in an area with a width of 200m. The width of the zone of seismicity increases to 400m at 3 km of depth. At 6 km of depth the observed seismicity stops and another zone with width of 400m to the west becomes active. The depth range of the shallow seismicity zone is the approximate depth range of the Arbuckle basement interface, so these shallow events could be signs of fault rupture extending into the Arbuckle formation.

The seismicity on these faults show a downward trend in depth as they approach the intersection with the SW fault (Figure 10 (b-e)). The seismogenic NF fault as observed on Figure 10 (b) has shallow events occurring at 2 km of depth with a portion

of events missing from between the two segments. This area extends down to a depth of 5 km before it shrinks from 2 km in length to 1.5 km. The same pattern also occurs for the NEF, with its length shrinking from 4.5 to 1.5 km at the same depth as NF. The NFs length decreases to 0.5 km at depth of 7.5 to 8 km. This pattern indicates that the seismicity on both of these faults is propagating down in depth as they approach the intersection with SW. When looking at the A to B (figure 10 e) cross-section, the shallow events of the SWF start at around 1.8 km and then extend down dip to a depth of 2.2 km before extending to 4.5 km of depth. A segment of concentrated seismicity that is 4 km long and extend from 3 to 5.8 km of depth. The events below 4.8 km of depth along the SWF deep events are shown in the inset mapview of Figure 10 (a).

The sizes of the seismicity zone are not the only feature of the fault system that changes with depth. Figure (11 a-g) shows that different fault segments are only active at certain depth ranges. The northern most segment of SWF is the shallow most portion of the fault with a depth of 1-2 km (Figure 11 a). Events at 2-3 km depth extend most of the length of the SWF and the northern tip of the NF has a cluster of events (Figure 11 b). For the 3-4 km depth range most of the events are shown to be occurring along the NF and the northern segment of the SWF and at the southern tip of the SWF with a seismic gap appearing in the center. This is also when the EWF starts to appear given that it is left lateral and there is a quiet, aseismic zone occurred right at the intersect between EWF and SWF.

The NEF and NE fault appear as one coherent fault segment occurring at 3-4 km depth. At 4-5 km of depth the seismicity shifts to the east by 400m (Figure 11 d). A similar shift occurs at the northern segment of SWF, with the seismicity shifting to the

NE from the previous location of fault. At 5-6 km depth, there are no longer any events occurring along the trend that was previously traced by the shallow events, which shows a clear shift in seismicity (Figure 11e). At 6-7 km depth, the seismicity located along the NF seismogenic fault is where the most recent events have been occurring (Figure 11 f). The seismicity observed at the depth ranges of 7-8 and 8-9 shows most seismic activity is clustered at the intersection of the NF and SWF (Figure 11 g-h).

Figure 12 expands on this analysis by only plotting events that occur over certain time periods. Figure 12 (a) shows the events that occur from the Mw 4.8 foreshock on November 5, 2011 through November 9, 2011 one day after the Mw 4.8 aftershock. During this time a large portion of the observed fault is activated. The mainshock occurred on November 6, 2011, 24 hours after the foreshock, the fault shows earthquake activity occurring along the entire length of the SW fault in the hours following the mainshock. The aftershock occurred 48 hours after the mainshock. Within hours after its rupture, the EWF was activated. 10 days after this period, events propagate further and deeper towards the end of the SW fault (Figure 12 b). Then when examining the period 20 to 30 days from the Mw 4.8 aftershock, events are no longer propagating further to the southwest, but are instead propagating downward or are located at the intersection of the faults (Figure 12c-d). Jumping forward by 4 months the events are not occurring in the shallow regions anymore, which could be due to the time span of the sub-space detected catalog (Figure 12 e). When examine the events that occurred between March 31, 2012 to the end of the catalog in January 2015, all the earthquake activity has shifted to a deep region below the NWF (Figure 12 f). The

deeper depth for the recent seismicity could be due to lack of near-source stations when all the temporary stations were removed in early 2012.

In order to see if the observed features in our relocated seismic catalog are accurate, we compare them to a previous structural interpretation for the area. To do this, I digitize the fault map and depth measurements of the Hunton group interpreted by *Way*, [1983]. The digitized fault map and formation depths are used to create surfaces that represent the bottom of the Hunton group. This is done using a diffusion interpolation in ArcGIS using the digitized faults as barriers to prevent the interpolation from smoothing the vertical displacement across faults, with the assumption that there is vertical offset and the dip of the faults is 90 degrees. The diffusion interpolation in ArcGIS uses the heat equation, which describes how heat or particles diffuse with time in a homogeneous medium. The predictions made using this method tend to try and flow around barriers. If there are no barriers used with the interpolation, the predictions made by the code are approximately the same as those that would be made by a kernel interpolation with a Gaussian kernel.

From this interpolation, I obtain an estimated elevation profile for the Hunton formation, which I compare to the original contour map to prevent any anomalies. Using this surface, I assume that the displacement and fault orientation of the basement-Arbuckle interface would be similar to that of the Hunton group. Using the shallow events between 1.8 and 2.2 km, which is the estimated depth range of the Arbuckle-basement interface [*Keranen et al.*, 2013a]. I then shift the depth of the surface until it matches the depth of shallow events in Figure (13). From this I find that the events that slope down along the SWF compare well to the displacement between the grabens

found in the Hunton group. If the depth of the graben continues to decrease to the SW, then that would support the observed decrease in the shallow event depth. Given the gradual transition of the earthquakes with depth in the observed area, the dip of the fault would have to be shallow given that the transition occurred over 1.2 km and only shifted 200 m. Another possible explanation would be that there are more complex fault features in the transition area, given that the depth change corresponds to where the events trace two parallel faults.

Based on the observations made above, the Prague earthquake sequence is far more complex than originally thought. The shallow seismogenic features and the concentration at the depth range of the Arbuckle formation indicate that the fault rupture extends up into the Arbuckle formation, with the shallowest portions of the rupture showing similar displacement to that of the structures observed in the Hunton group. The faults in the system are nearly vertical and the observed seismicity migrates to the northwest with depth. The wider zones of seismicity observed at deeper depths could indicate that multiple faults are overlapping in the observed regions or wider damage zones. The migration of seismicity observed at deeper depths could possibly be caused by the interaction of the NWF and the NEF faults.

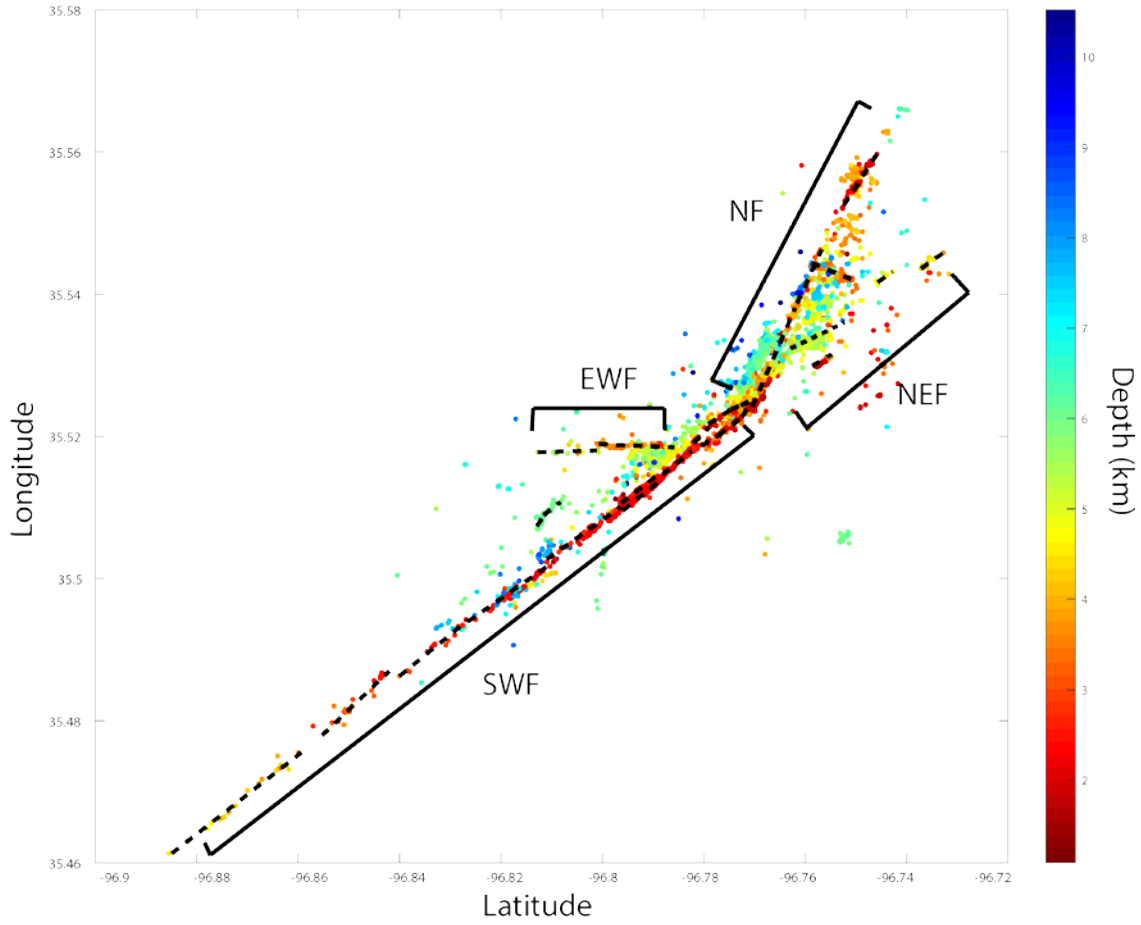

Figure 9. Mapview of relocated earthquakes with the color bar representing the depth of the events in km. Interpreted faults are drawn with dashed lines, the earthquakes are grouped into 4 segments with the given name next to the group.

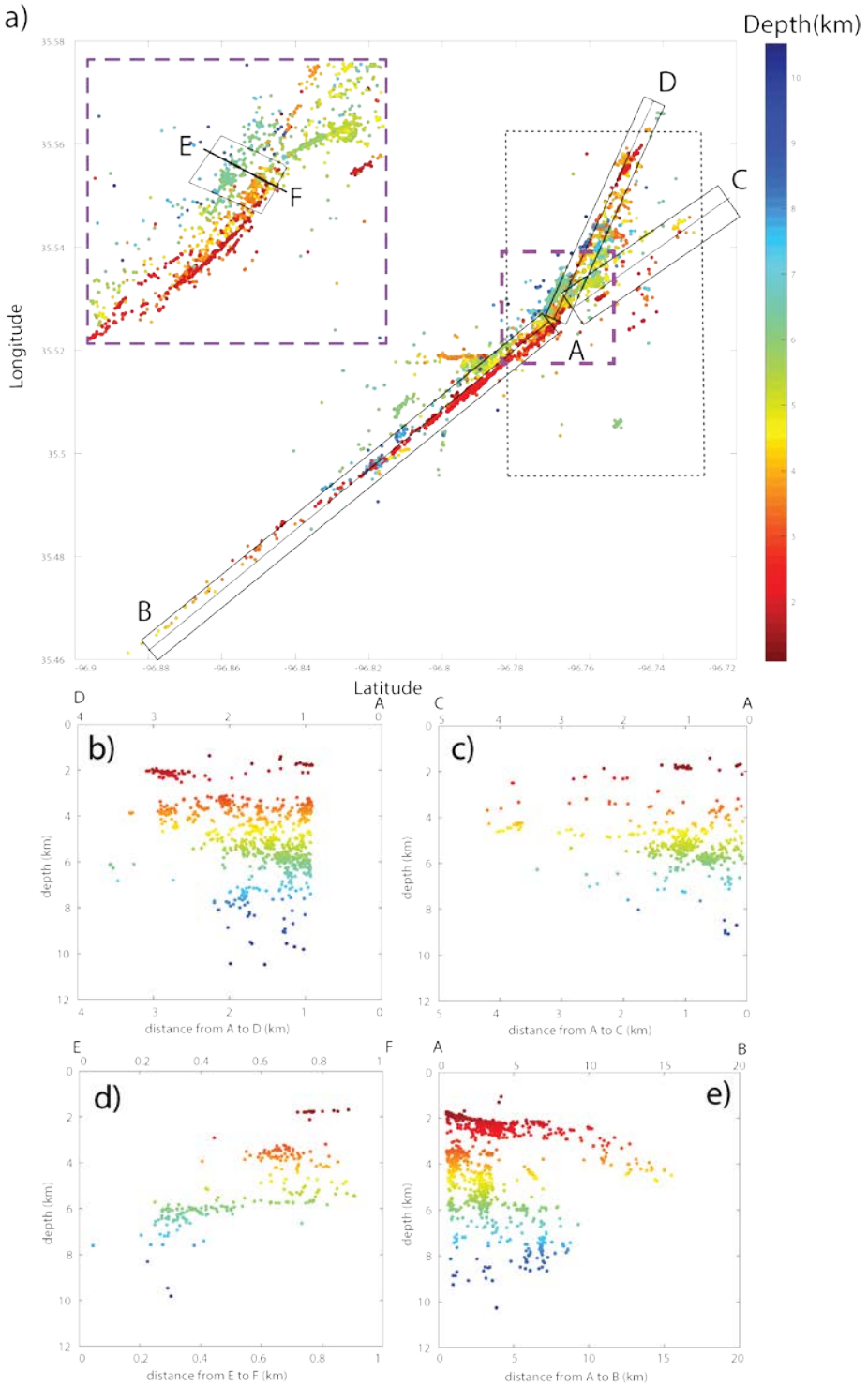

Figure 10. Map view earthquakes with a zoomed in view of the fault intersection (Dashed purple box). Earthquakes are colored by depth. Solid boxes represent earthquakes selected to be viewed in each cross-section. Dashed box is the surface area shown in figure 13. (b) Cross section D -A. (c) cross section C-A. (d) cross section E-F. (e) Cross section A-B.

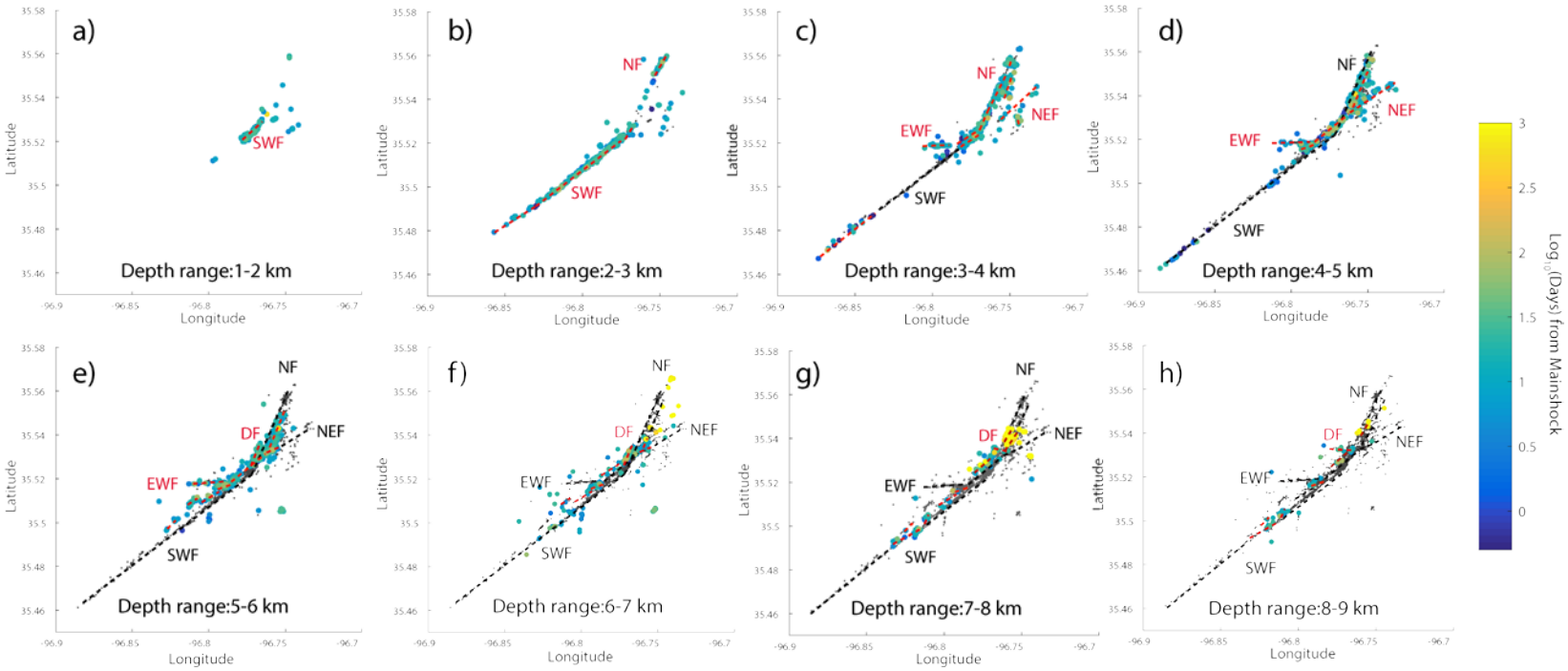

Figure 11. (a-h) Depth plot of cluster with each figure showing 1 km of depth with new appearing faults drawn in red and old fault or repeating fault locations in black.

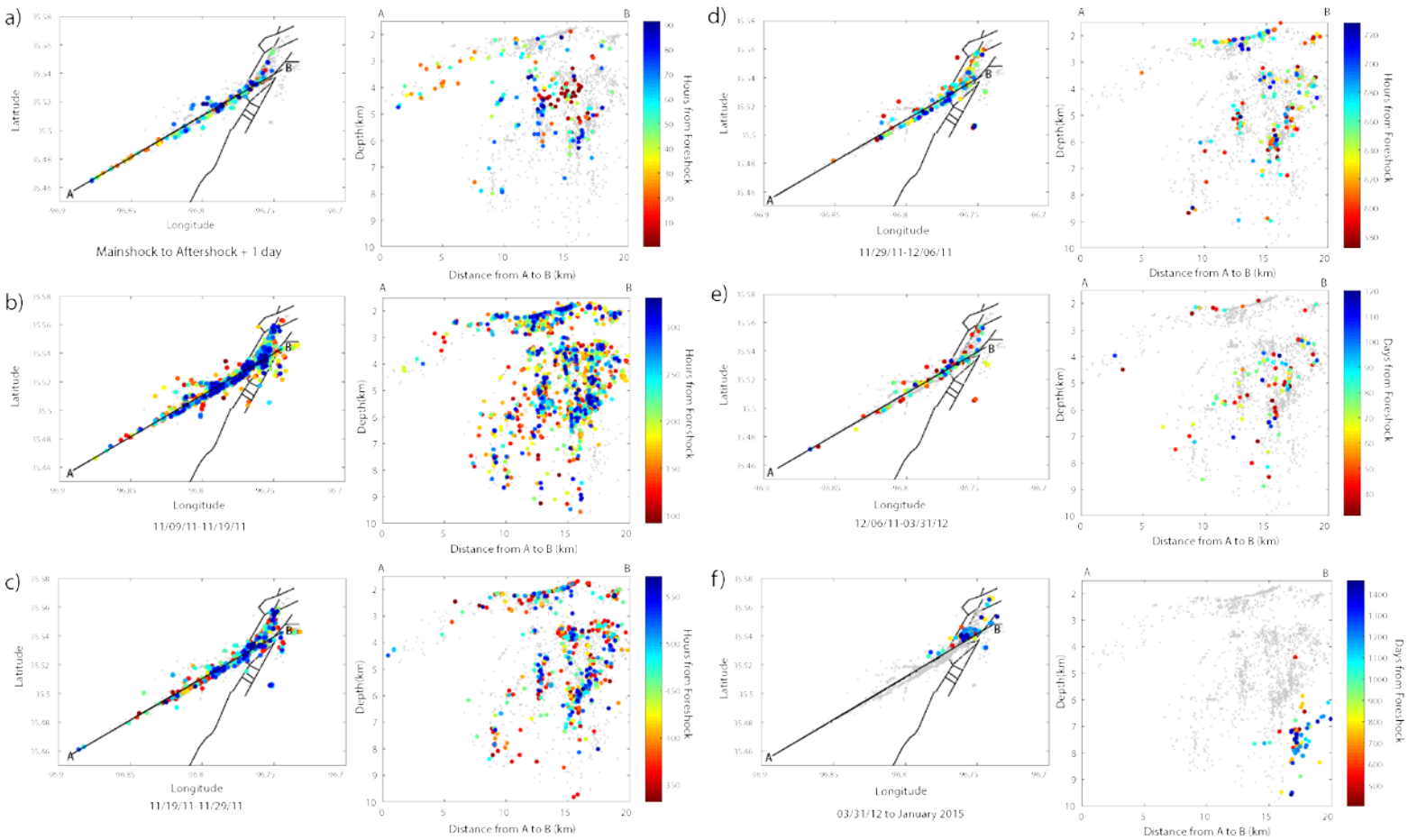

Figure 12. Snap shots of the propagation of events with events colored by time. There is a map view and a depth view parallel to strike. (a) Are all events that occurred during the foreshock to aftershock period plus the addition of one day. (b-d) 10 days' time added to the previous snapshot, with events colored by hours from the foreshock. (e) Snapshot from December 6, 2011 to March 31, 2012 with events colored by days. (f) March 31, 2012 to end of data set with events colored by days.

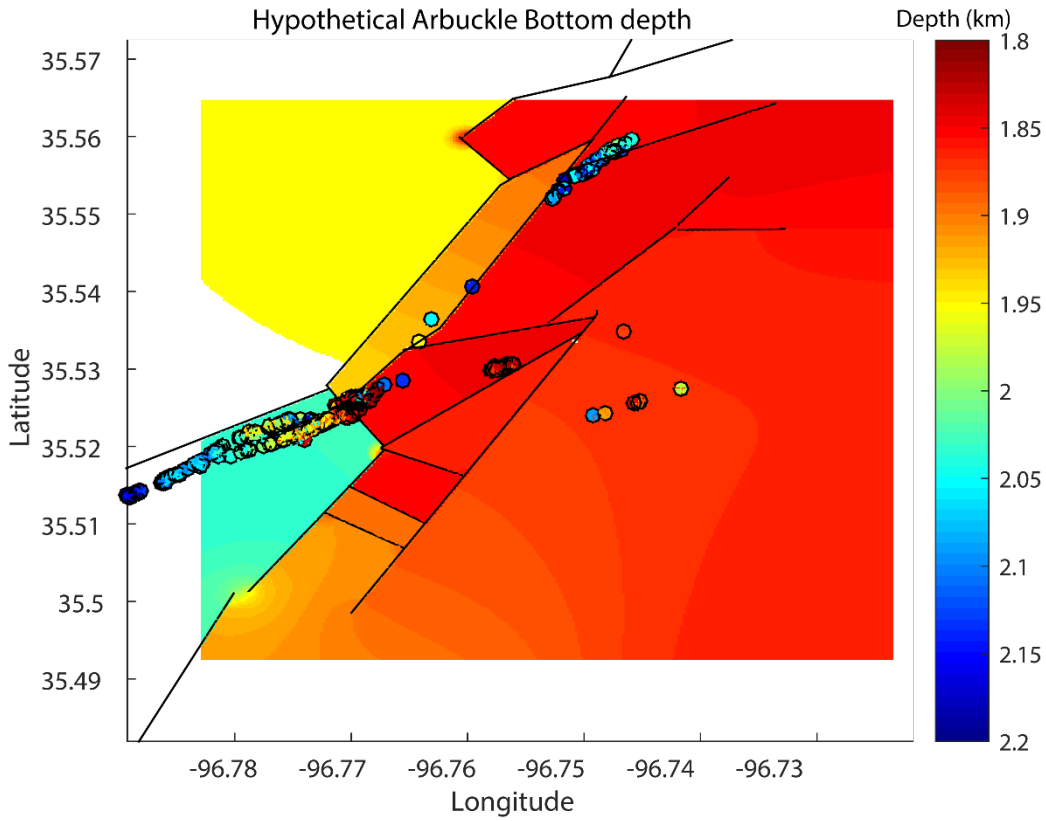

Figure 13. Zoomed in dashed box in figure 10. With only events between 1.8-2.2 km in depth shown and colored by depth. The surface was interpolated from depth data form the Hunton group.

Chapter 4: Prague Spectral Analysis

Spectral Introduction

Stress drop is one of the key parameters in the ground motion estimations [e.g., *Yenier et al.*, 2017] and also one of the most important parameters for understanding earthquake scaling and source physics [e.g., *Abercrombie,* 2014, 2015]. Therefore, accurate estimation of stress drop is very important. However, it is quite common for stress drop to range over several orders of magnitude for individual studies [*Cotton et al.*, 2013]. Given this uncertainty, it is difficult to constrain spatial and/or temporal variation in stress drop. The uncertainty associated with stress drop can be even larger when considering different methods used to calculate it.

Even our knowledge of how stress drop relates to moment is uncertain, and it remains a heavily debated topic in the field. The argument centers on whether stress drop increases with moment or if it is independent of moment. Studies done by *Pacor et al.*, [2016] and *Calderoni et al.*, [2015] have found such a scaling relationship between stress drop and moment for the 2009 Aquila earthquake. Other studies done in South Africa, California and New Zealand found no dependence of stress drop on moment [*Shearer et al.*, 2006a; *Kwiatek et al.*, 2011; *Oth and Kaiser,* 2013]. Besides the scaling controversy there are other factors that can affect stress drop estimates. For example, for methods that use smaller events as empirical Green's function (EGF) events in *Abercrombie et al.*, [2017], the choice of different EGF events can have significant impact on the results [*Kane et al.*, 2013; *Abercrombie*, 2015; *Del Gaudio et al.*, 2015].

One other possible factor that could affect the results is the limitation of frequency bandwidth. If the corner frequency is near the upper bound of the frequency

band, it will be severely underestimated [*Abercrombie*, 2015]. This problem not only effects the single EGF method, it also plays a role in the stacking approach [*Shearer et al.*, 2006a]. The stacking method shown in *Shearer et al.*, [2006a] and used in this study, which is able to reduce the possible errors associated with directivity of earthquakes by averaging over wide azimuth [*Calderoni et al.*, 2013]. This lessens the effect of erroneous spectra and allows for large numbers of events to be examined. The stacking method can produce reliable estimates of the average stress drop as well as the overall pattern of stress drop in an area. However, by stacking multiple spectra, it loses resolution and may not reveal details of the rupture process as individual EGF analysis [e.g., *Abercrombie*, 2014]. These two methods can produce similar results as in *Allmann and Shearer*,[2007], and *Abercrombie*, [2014], where both studies found similar results for one repeating earthquake sequence with simple source time functions and relative larger magnitude, however, they didn't agree well for a sequence with complex sources, and a sequence with high corner frequencies that approach the upper bound of the frequency band. Finally, the Brune-type stress drop that is derived from spectral analysis is based on the assumption of circular source models and a constant rupture velocity [*Brune*, 1970; *Boatwright*, 1980]. If this is not true, then these estimated stress drops may not be accurate.

Prague Spectral Method

To analyze the spectra of our relocated events, I first obtain the waveforms of each event at stations with a sampling rate of 200-250 Hz. A P signal window of 1 second is set to begin 0.1 seconds before the P arrival to account for errors in the

picking process, while a noise signal window of 1 second is selected before that. A 1.5 second window is selected for the S-wave after the S pick, and a 10 second window after the S-wave is selected for the coda wave analysis. I then compute the velocity amplitude spectra for the signal and noise window using a multitaper algorithm [*Thomson*, 1982; *Percival and Walden*, 1993]. I convert these velocity spectra to displacement, and then resample all spectra to equal log-spacing between 0.5 and 95 Hz for further analysis. A signal-noise ratio (SNR) criterion is adopted to select high-quality spectra. The SNR is defined as the ratio between the spectra of the signal and the. For each event, I examine three frequency bands (0.5-5, 5-15, and 15-80 Hz) and set an average SNR ≥ 5 for the first two frequency bands, and minimum SNR of ≥ 3 for the third frequency band to ensure high-quality high-frequency recordings. The SNR requirement is applied to all wave types and all channels. From the original catalog, only 351 events have at least 1 station that passed criteria. For P-wave analysis, only the vertical channel is used. For S-wave and Coda-wave analysis, the geometrical mean of the two horizontal channels are used [*Sumy et al.*, 2014].

Following *Shearer et al.*, [2006], the observed displacement spectra are considered a convolution of source (event) E, path P, and ST effects (includes both site and instrument effects). In the frequency domain, the recorded spectra D(f), can be written as the product of source, path and station spectra (Figure 14):

$$D(f) = E(f)P(f)ST(f)$$

This is then linearized by working in the log-f domain,

$$\log D(f) = \log E(f) + \log P(f) + \log ST(f)$$

Now this can be viewed as an over-determined system of equations because each event E_i is recorded by multiple stations S_j. Each station records many events, and each path from source and receiver will be traveled multiple times, which can be approximated by a travel-time dependent term T that depends on the distance between the event and station. The travel time is discretized into bins (k) of 0.2 seconds of the recorded source-receiver travel time $T_{k(i,j)}$. Viewing it this way I can write a linear equation in the form of:

$$D_{ij} = E_i + T_{k(i,j)} + ST_j + R_{ij}$$

for each observed spectrum, where R_{ij} is a residual error term. In order to mitigate the influence of outliers, an iterative, least-squares method is used to solve for $T_{k(i,j)}$, ST_j, E_i, which is performed for each frequency point independently [*Shearer et al.*, 2006a].

The above method only resolves relative differences between source spectra of each event, so I need to correct for propagation effects that are common to all event paths. [*Shearer et al.*, 2006a] resolved this by computing averaged, stacked spectra in bins corresponding to a range of spectral moments. To do this, I first need to calibrate the measured seismic moment Ω_0 to the absolute moment M_0 using the local magnitude M_L. I define Ω_0 using the mean amplitude over 1 – 3 Hz band. This is done by fitting a linear relationship between $\log(\Omega_0)$ and M_L using the equation $M_L = 1.0 \ \log_{10} \Omega_0 + 2.19$. The events used in the calculation are limited to those that have an estimated $\log(\Omega_0)$ of 1-6 to preserve the linear relationship of the higher magnitude events. If this is not done, the higher magnitude events would be either under or over corrected if those events with lower measured seismic moment are included in the fitting. This error

in fitting is caused by the systematic magnitude difference between the OGS catalog and the subspace-detected catalog (Figure 15).

I initially only consider events that have P, S or Coda wave spectra stacked from at least 7 stations that passed the previous spectra SNR criteria. The calibrated magnitudes are then used to stack the source spectra in incremental magnitude bins, with the requirement that the bin contain at least 5 events.

Instead of assuming a constant $\Delta\sigma$ for each bin as in [*Shearer et al.*, 2006b], I allow for the possibility of mean stress drop to vary with moment for each bin similar to the method of *Trugman and Shearer*, [2017], which found a unique EGF for each bin to allow the assumption of non-similarity between magnitudes. I use a different approach that calculates the predicted spectrum for the lowest magnitude bin, which would then be applied to the other magnitude bins to estimate the regional EGF following the approach in *Chen et al.*, [2016].This method attempts to combine the methods of *Shearer et al.*,[2006a] who used the stacking approach and *Abercrombie et al.*, [2017] who generates a stacked EGF for individual earthquakes from highly correlated events (cross-correlation ≥0.8) that are 1-2.5 magnitude units lower and within 2 km of the target events. When testing against the previous method of *Shearer et al.*, [2006a], it shows greater stability using varied magnitude ranges, frequency bands, and number of required stations.

To calculate the EGF from the lowest magnitude bin, this is done using a grid search method that determines the best fitting theoretical source model proposed by *Brune* [1970]:

$$u(f) = \frac{\Omega_0}{1 + (f/f_c)^2}$$

The Ω_0 is the long-period amplitude and f_c is the corner frequency. The residual between the observed spectra of the lowest magnitude bin and best fitting theoretical source model is the EGF. This EGF correction is then applied to the other magnitude bins. The corner frequency f_c can then be related to stress drop $\Delta\sigma$ by using the relation found by *Brune* [1970]:

$$\Delta\sigma = \frac{7M_0}{16}\left(\frac{2\pi f_c}{2.34\beta}\right)^3$$

For a shear wave velocity β (assumed to be 3.5 km/s). I then calculate the overall misfit with the predicted source model for all magnitude bins, until I get the best-fitting $\Delta\sigma$. The regional EGF obtained from the best-fitting $\Delta\sigma$ is then used to correct the shape of the relative source spectra of the individual events for their propagation effects.

To test the stability of the estimated stress drop, I varied three parameters, magnitude range (maglim), frequency range (freqlim), and the number of stacked station spectra for individual events (nspec). The magnitude range is tested by varying the lower limit of the magnitude between 1.5-1.9 Ml, and the upper magnitude limit between 2.2-3.5 Ml. The frequency ranges lower limit is varied between 0.5-2 Hz, and upper limit of 15 – 60 Hz. The number of stack spectra is varied between the 3-10. This is done both for the Boatwright [*Boatwright*, 1980] and Brune [*Brune*, 1970] models. I choose to use the Brune model given that it provides a better fit. I perform this analysis for all wave types.

The P-wave spectra are selected to be the first spectra results tested of the three wave types (Figure 16). It shows stability around 7 nspec (Figure 16 a). This therefore becomes the standard value for the magnitude and frequency tests. From varying the

magnitude, the magnitude range that is the most stable and allows for the most events to be included is 1.5 M to 2.9 M, given the stability of the stress drop (Figure 16 c). When testing, frequency limit the stress drop increases as the upper frequency limit is increased, due to the corner frequencies becoming more accurate given the expanded spectra (Figure 16 b). From this observation, I chose to use a frequency limit of 1-60Hz. I had recorded the spectra up to 95Hz, but given the unknown effect of the observed geologic structures on higher frequencies the limit is kept lower than the maximum value.

I then perform the same analysis on the S-spectra (Figure 17) and the C-spectra (Figure 18). The S-spectra nspec results are stable with a stress drop estimate of 3.2 MPa for the four to seven station range (Figure 17 a). The 60Hz and 40Hz frequency range converge with each other very well, showing that most of the S-wave spectra is able to obtain the corner frequency with a smaller frequency range. This is supported by the frequency tests that show the 40.71 to 60 Hz high frequency range having a stable and constant stress drop (Figure 17 b). The most unstable changes come during the 27 to 40 Hz range (Figure 17 b). The magnitude lower limit and higher limit ranges have a region of stability from 0.9 to1.90 and 2.5 to 3.10 before increasing the stress drop by 1-2 MPa (Figure 17 c). The magnitude range shows a much greater variability at lower frequency ranges that causes a 1-3 MPa decrease in the stress drop estimate. From the observed changes in stress drop caused by changes in frequency and magnitude range, the S-wave results show greater instability than the results observed for the P-wave spectra. From the analysis of the S-spectra the values chosen for the P-spectra fall

within the observed stable ranges, so the same parameters were kept the same for the individual event analysis to allow an accurate comparison.

The C-wave spectra are the final spectra that I examine and I consider these spectra to be the most stable given that it covers the longest time window and contain the most spectral information about the event. The stress drop estimate for the nspec range is similar to that of the P-wave, which increases our confidence in this result. The most stable region for the C-wave is the 3-6 nspec range (Figure 18 a). I want to keep the results comparable with P and S waves, so I decide to maintain the choice of 7 nspec, even though it represents the maximum value for the C-spectra. The maximum value is only 1 MPa greater than the average, so that is well within the acceptable variability (Figure 18 a). The frequency range shows stability being reached at around 28.86 Hz. Variability in the low frequency range shows that the estimated stress drop will increase from 1.5 to 2.00 Hz frequency range. It will then become stable and before returning to a lower stress drop estimate of (1-2 MPa) when the lower frequency is about 2.5 Hz. Given the variability over the low-frequency limit, I decide to remain with the 1-60Hz range (Figure 18 b). The magnitude range shows a stable stress drop in the low magnitude ranges of 1.2-1.5 and for all the higher magnitude ranges (Figure18 c). This makes us confident in using the 1.5 to 2.9 magnitude range. The lower frequency magnitude test shows instability, but the value tends to remain between 1-0.5 MPa.

From these tests, I determine a stable solution for the regional EGF. I calculate and correct each waveform using the magnitude range of 1.5 to 2.9, frequency range of 1-60Hz and a station requirement of 7 or more. Comparing the individual stacks for the

correction, I observe that each produces a well-fitted result. That makes me confident in correcting the individual source spectra using the regional EGF (Figure 20).

After subtracting the regional EGF from the spectra of the individual events, I find the best fitting f_c. Then finding the $\Delta\sigma$ I calculated the Brune stress drop using the shear velocity from *Keranen et al.*, [2013b], which was obtained from velocity logs of nearby wells. I only analyze single events that had 5 or more stations and occur in all three waveform results. The EGF was obtained with a requirement of 7, this change is based on the previous sensitivity tests, that show the stability at both 5 and 7. From this observation the inclusion of more events after the correction, should not greatly affect the median stress drop. The reason why the number of stations is reduced is to allow for the inclusion of the aftershocks that occur in the 3 days following the mainshock and aftershock to be included in the analysis. With a 5 station requirement, I find a median stress drop of 2.00, 4.07, 2.29 for the P-wave, S-wave, and C-wave, respectively (Figure 19). The P-wave and the C-wave results agree well with one another, both have an upper limit of 15 MPa, and both extend to 0.1 MPa. The S-wave shows the most anomalous value with an estimate of 4.07. This variance could be caused by simply the differences in wave type spectra, or due to the lack of low frequency information observed for many of the S-spectra. Another possible cause for this could be due to insufficient window length, or instability in S wave for this earthquake sequence.

From these results, I then decide to first compare the different median values against their moments. I find that they have similar patterns, which show that there is not systematic scaling of stress drop for the magnitude range observed here (Figure 21). Similarly, the spatial variability for the P, S and coda waves are very similar (Figure

22). They all show an increase in the stress drop with depth, and all have lower stress drop in the shallow region. The areas where they differ the most is that the P-wave predicts higher stress drops at the 4-5 km depth range. The S-wave reports lower stress drops for that region and only shows consistently higher stress drops below 6 km. The C-spectra results show a mixture of lower and higher stress drops in that region. From this analysis, I decide to use the C-spectra because of the stability observed from the different tests.

To see if the results seemed reasonable, I compared the result to other calculated stress drop results for the Prague sequence. Comparing the results to others obtained using different methods I found that the stacked S-wave results, and those of *Yenier et al.*, [2017] correlated well with the stacked coda results. The stacked Coda results as well as other S-wave Stacked results are consistently different from those of *Sumy et al.*, [2017]. To examine if the systematic difference between the results is caused by differences in processing of data or selected time windows I compared my results to those obtained using the method of [*Sumy et al.*, 2017] on my data set (Coda-Kappa results in Figure 24). This result does show some correlation with the Coda determined results, but it still has a systematic bias to lower stress drop values. The results of *Wu and Chapman*, [2016] were recently updated and they were kind enough to allow us to compare ours to theirs. When comparing against the stacked Coda-results some events do correlate well with their results, but they also have values widely (order of magnitude lower or higher) different from mine that don't compare well with the other estimated values either (Figure 24). I also tried to compare the results to the previous study done by *Boyd et al.*, [2017], however I only had 3 matching events between our

results, which did not allow for adequate assessment (Figure 24). The Coda-Kappa obtained values show a clear preference to a lower corner frequency and the estimated stress drops are far from the average values estimated for the finite fault model and strong motion estimates. The median value of 2.10 MPa is close to the estimated value of 1.6 MPa made by the finite fault model [*Sun and Hartzell*, 2014].

From these comparisons, I feel confident in the results obtained using the stacking method. I use these results to examine the cluster for temporal and spatial trends. From the previous interpretation of the fault I divide the cluster into 6 segments that correspond to the NEF, NWF, EWF and SWF. The SWF is then divided into two segments, one for events in the shallow region, and the other for the events that are below interpreted Arbuckle formation (Figure 25 a). We also added a new group called the South-East fault (SEF), which is seismogenic fault that occurred to the south east of the Wilzetta fault system. I then examined the stress drops observed in each cluster for 120 days and found the linear fit for each cluster, which should give an estimate of the trend in stress drop within through the 120 days. Doing this, I find that the shallow events consistently had a lower stress drop 0.2-1 MPa (Figure 25 c), while the deeper fault segments had higher stress drop with a trend that remained stable throughout the clusters history. The EWF fault however shows a higher overall trend in stress drop. Its events occur between 4-6 km of depth, so they should not be skewed by the deeper events.

Discussion

Assuming that the source model and rupture velocities used above are accurate and represent the rupture of each event, I find that the stress drop 10 to 90 percentiles

ranges are 0.468 – 8.488 MPa, 1.168-11.073 MPa, and 0.411-8.486 MPa for the P, S, and Coda waves, respectively. With a median value for P, S, and Coda being 2, 4.07, and 2.21 MPa, respectively. The standard deviation observed for the $\log_{10} \Delta\sigma$ ranges around 0.47-0.53, which is well within the limits of stress drop variability found in other studies [*Cotton et al.,* 2013; *Abercrombie et al.,* 2017]. As observed from our sensitivity test analysis, some extreme parameter sets may change the median stress drop systematically by a factor of 2-10, but the final reported median values represent the stable result over a wide parameter space. Our stress drop matches results found by *Yenier et al.*,[2017] and the median stress drop fall within the range observed for events in the central United State by *Boyd et al.*, [2017]. It also falls close to the average slip estimated by [*Sun and Hartzell*, 2014] as shown in Figure 23, showing good comparison with three other measurements made for the sequence.

Moment Dependence

I do not observe any scaling of moment with magnitude (Figure 21); the median value obtained for each spectra type shows no consistent increase with moment. However, I did not examine the large magnitude events given the lack of station coverage for the foreshock and mainshock, and that the aftershock clipped a large portion of the nearby stations. This result differs from that of *Sumy et al.*, [2017], who found a positive trend with moment. This trend has not been found for natural earthquakes [*Allmann and Shearer*, 2009; *Baltay et al.*, 2011; *Abercrombie*, 2015] in previous studies, but a recent study reported dependence with magnitude using improved method [*Trugman and Shearer*, 2017], so the debate is still ongoing. There have also been other studies that have found weak trends between stress drop and

moment [*Pacor et al.*, 2016; *Boyd et al.*, 2017]. *Pacor et al.*, [2016] found a strong correlation between stress drop and magnitude for events large than M3.5, which were not examined in this study due to the magnitude limits. [*Boyd et al.*, 2017] examined events across the United States and found that there was a weak trend between stress drop and moment for their events. They explained this trend with the theory that larger events rupture along stronger fault patches, which would then produce a high stress drop compared to other lower magnitude events.

Depth Dependence

I find a correlation between stress drop and depth (Figure 25 d, 26 b, d, f, h, j, l). This correlation has been found in many studies [*Shearer et al.*, 2006a; *Hardebeck and Aron*, 2009]. Note that these results do not assume a constant rupture velocity with depth; a 1D velocity model obtained from velocity logs of nearby wells was used to represent the rupture velocity of different zones [*Keranen et al.*, 2013b]. If this correction was not done then the relationship between stress drop and depth could be attributed to the use of a constant shear wave velocity, which might not properly account for the changing rupture velocities of different rock types. This is especially important for the shallow events observed in this study, since they are interpreted to be in the Arbuckle group, which has a different shear velocity than the basement where the other events are observed. The events of the shallow region after a velocity correction is applied have stress drops that range from 0.23 to 4.79 MPa (10^{th} and 90^{th} percentiles) at a depth range of 1.8 to 2.5 km. The deeper regions of the fault have a stress drop range of 0.467 to 8.545 MPa (10^{th} and 90^{th} percentiles). The mean stress drop for the shallow region is 2.4 MPa, and the deeper region (greater than 2.5 km) has an average stress

drop of 2.78 MPa. The depth range of 2.5 km of depth was used because that is the bottom of the observed shallow seismicity zone, which is interpreted to be the bottom of the Arbuckle formation.

To examine the difference between the two depth ranges we now apply a uniform velocity correction of 3.46 km/s. With the uniform velocity, I obtain stress drops of 0.22 to 5.58 MPa, and 0.47 to 9.66 MPa for the shallow and deep regions respectively. The average stress drop for the shallow region is now 2.6 MPa, and the deeper region now has a stress drop of 3.11 MPa. The percentage change between the two zones is 15.53%. We predict what type of velocity contrast we would need to make the two averages converge. For the average stress drops of each zone we need a velocity contrast between the two zones of 0.19 km/s (or 5.5% of 3.46 km/s) for them to converge. For the range of values observed in each to be the same, the velocity contrast would have to be 0.56 km/s (or 16%). Using this contrast prediction, the velocity for the Arbuckle formation would need to be 2.9 to 3.27 km/s. This falls within the observed shear velocity ranges for both dolomite (1.9-3.6 km/s) and limestone (2-3.3 km/s) [*Bourbié et al.*, 1987]. The current velocity model predicts that the Arbuckle has a shear velocity of around 3.04 km/s at 2 km of depth while the basement has 3.46 km/s, the velocity contrast between the two zones to be 0.42 km/s. This justifies the velocity correction adopted for our final results, where the median stress drop of 2.4 MPa for the shallow group is consistent with the deeper group of 2.7 MPa.

This analysis assumes that the stress drop is primarily controlled by the minerology of each formation and its effect on rupture velocity. It also assumes a uniform velocity for an entire formation. This is inaccurate given that the Arbuckle

formation contains dolomite as well as limestone, which would lead to velocity contrasts inside the formation itself. This analysis does not account for the possible effect of low stress drop events caused by aftershock rupture on fault patches that experienced high slip after the mainshock. The effect of pore pressure in the basement and in the Arbuckle formation is also not accounted for. The study by *Sumy et al.*, [2017] interpreted the low stress drop observed in their findings to be caused by injection and higher pore pressure, so it's effect should be taken into account in future analysis.

Spatial Observations

I observe some patterns when I examine the stress drop divided into different groups based upon the different fault segments and depth ranges observed in the seismic relocation (Figure 25 c). For the EWF, I observe a consistently higher overall trend in stress drop compared to other groups (Figure 26 i, j). It is mostly contained in the depth range of 2-7 km, so its trend of stress drop should resemble that of NF (Figure 26 c, d) or the NEF (Figure 26 e, f). The EWF consistently has a higher stress drop value for events at all depth ranges even for the events that occur around 2 km of depth where the stress drop should be the lowest (Figure 25 c, 26 a, b). This observed stress drop difference can also be observed when examining the histogram of each of these groups (Figure 27). This could be explained by the interaction of the EWF, which has a left-lateral rupture and the SWF, which has a right lateral rupture. Not enough is known about the two faults and how they intersect with one another to confidently interpret the observed higher stress drops.

Temporal Observations

I found a trend between higher stress drop in time from the Mw 4.8 foreshock on November 5, 2011 similar to the observations of *Sumy et al.*, [2017], and *Yenier et al.*, [2017]. All three studies found a trend of increasing stress drop over time. *Sumy et al.*, [2017] found an overall trend of increasing stress drop that they interpreted to show the propagation of the fault. *Yenier et al.,* [2017] found that events that follow each mainshock closely in time and distance exhibit a low stress drop. I found a similar pattern for the SWF (Figure 26 g,h), where a cluster of events with low stress drop of 1 to 0.1 occur for 80 hour after the mainshock (Figure 25 c, 26 g). A similar pattern is observed for the EWF, the aftershock occurred 2 days after the mainshock and when it does there is a segment of events with low stress drop extending for 80 hours after the aftershock rupture (Figure 26 i). Each of these groups exhibits a tailing off of the low stress drop events after 40 hours, but both have a final low stress drop event occuring at the 80 hour mark. One possiblity that might lead to this drop in stress drop after the >Mw 4.8 aftershock is that these events are rerupturing portions of the mainshock rupture area which the mainshock caused to slip during its rupture (Figure 23 b). A similar pattern was observed by *Abercrombie,* [2014] for repeating clusters of earthquakes that followed the 2006 M6.0 mainshock that occurred along the San Andreas Fault at Parkfield. She attributed this pattern to a short recurence time of events that limits the healing time of the fault, which could be reflected in the observed lower stress drop over time [*Vidale et al.,* 1994; *Shaw et al.,* 2015]. Due to the lack of repeating events in this sequence, it is difficult to attribute the increase of stress drop to fault healing. Instead the likely cause of the increase is partially due to the propogation

of events further away from the mainshock onto fault patches that have not slipped. When examing stress drop over longer time periods there is no clear trend that shows a increase or decrease in stress drop. There is spatial pattern observed over time that shows repeated instances of event propogation to deeper depths. The first instance of this pattern shows an intial propogation down to 9 km of depth occuring over a period of 30 to 300 hours after the mainshock (Figure 25 d). Later in time a longer propogation occurs over a period of 1000 hours (Figure 25 d).

Fluid Injections Effect on Stress drop

For these events I find stress drops that are low for periods after the mainshock can be explained events occurring on recently slipped portions of the fault [*Vidale et al.*, 1994; *Shaw et al.*, 2015]. Now *Sumy et al.*, [2017] posited the idea that the overall lower stress drop for the aftershocks in the entire cluster is caused by injection saturating the fault system. This idea has merit, becuse faults can be pushed to a critical state by an increase in differential stress, which can occur from by increasing in the shear stress on the fault or by increasing the pore fluid pressure [*Pearson*, 1981; *Goertz-Allmann et al.*, 2011; *Rubinstein and Mahani*, 2015]. Injecting fluids in the formations near the Wilzetta fault sequence could have led to a pore pressure increase inside that formation as well as in fractures in the basement rock, possibly pushing those faults into a critical stress state [*Zoback and Hickman*, 1982; *Talwani and Acree*, 1985]. High pore pressure will lower crustal strength as well as lower Coulomb stresses on the fault [*Bell and Nur*, 1978], which can lead to lower stress drop as observed by [*Kanamori and Anderson*, 1975; *Pearson*, 1981; *Goertz-Allmann et al.*, 2011]. You can observe this effect by correlating stress drop to the distance from the injection wells where the pore-pressure

should be the greatest [*Chen and Shearer*, 2011; *Goertz-Allmann et al.*, 2011; *Kwiatek et al.*, 2014].

In my analysis, however I find no correlation between distance from the wells and the observed stress drop. I find that stress drops are better correlated with their individual groups than they are with any well. This does not mean that injection had no effect on these events, there is just currently no available data that tells us how high the fluid pressure was on fault planes prior to their failure. It is possible that fluid was able to propagate throughout the fault system given that the permeability of faults can be magnitudes greater than that of the surrounding rock [*Zoback and Harjes*, 1997]. Fluid injection was started in 1993 and given the amount of time between then and the mainshock, the entire fault system could have been effected. I also observe that the stress drop of the events that I interpret to be in the Arbuckle layer exhibit the lowest stress drops (Figure 26 a, b, 27). This formation is the one that primarily that receives all injection, so it would be the most effected by any pore pressure weakening. These effects could also just be a factor of the shallow locations of the earthquakes. That explanation could also be applied to the earthquake cluster as a whole, since they are shallower than those observed on the west coast. *Boyd et al.*, [2017] scaled the stress drops to a common depth, focal mechanism and moment. They found that west coast and central United States earthquakes were similar in stress drop, with the largest driver in difference being event depth. This could provide another explanation for why the Prague cluster has lower stress drop. However, such corrections for depth, and moment assumes that there is a trend in stress drop for all those factors, which can introduce large amounts of error.

Conclusions Prague:

Using a subspace detected catalog *Mcmahon et al.*, [2017, in review], of the Prague earthquake sequence that extended from November 8, 2011 to December 8, 2011 and combining it with the OGS catalog, I obtained a GrowClust relocated catalog of the combined events [*Trugman and Shearer*, 2017b]. I find that the cluster is composed of a number of anastomosing faults indicating a complex fault system. From this catalog, I determined the stress drop for 214 events. I correct individual spectra for site effects by calculating a regional EGF using a modified stacking method [*Shearer et al.*, 2006a] that used the smallest magnitude bin of events to determine a theoretical model for the other bins. Using a grid search method, I determined a regional model that best fit all bins, which was then applied to the single events. This method was done for the P, S, and Coda spectra, using multiple parameters to test for stability.

I find that the stress drop for the Coda wave varies between 0.411-8.486 MPa (10^{th} and 90^{th} percentiles) with a median stress drop of 2.21 MPa using the Brune model. Comparing individual results and our obtained median value I find that our values agree well with those of previous studies done of the Prague sequence [*Sun and Hartzell*, 2014; *Boyd et al.*, 2017; *Yenier et al.*, 2017]. I find that stress drop increases with depth, and shows lower stress drop after the rupture of the mainshock indicating events occurring in fault patches that slipped during the mainshock. I also find that stress drop varies spatially with the E-W splay fault showing high stress drop compared to the other faults. I also observe the lowest stress drop occurring in the Arbuckle group, which is clearly defined by events in the sub-space catalog.

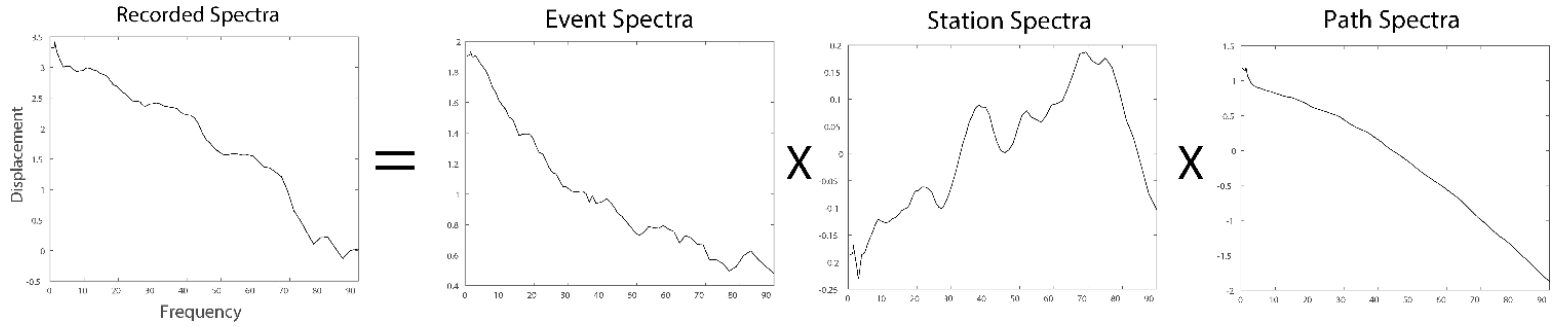

Figure 14. Example of recorded spectra, event spectra component, path component and station term.

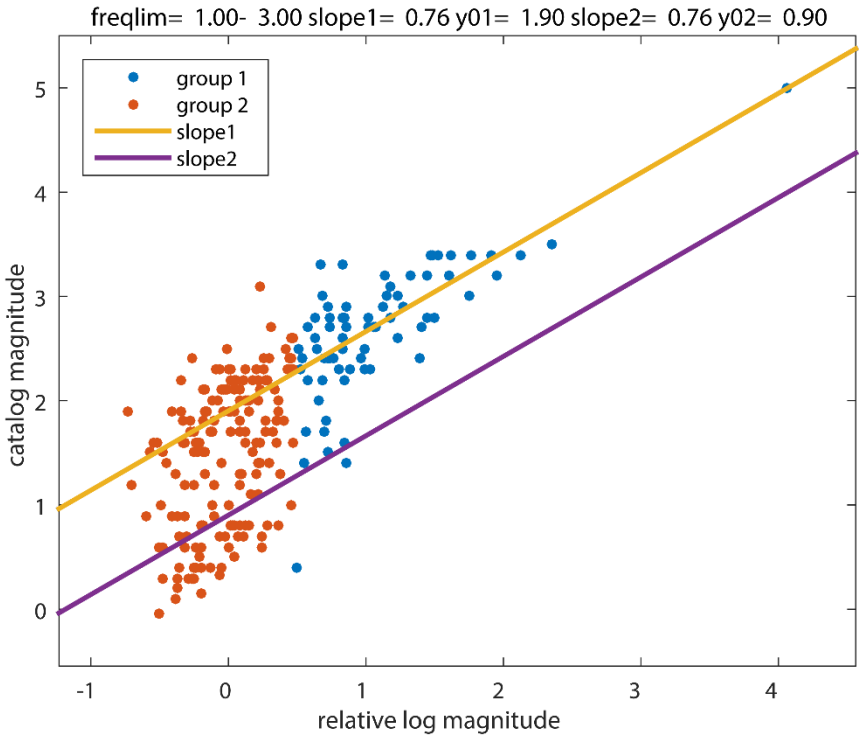

Figure 15. Linear relationship between relative log magnitude and our catalog magnitude. Slope 1 is the slope of the higher magnitude events in group 1 and group 2 is the lower magnitude events, which have the slope of slope2.

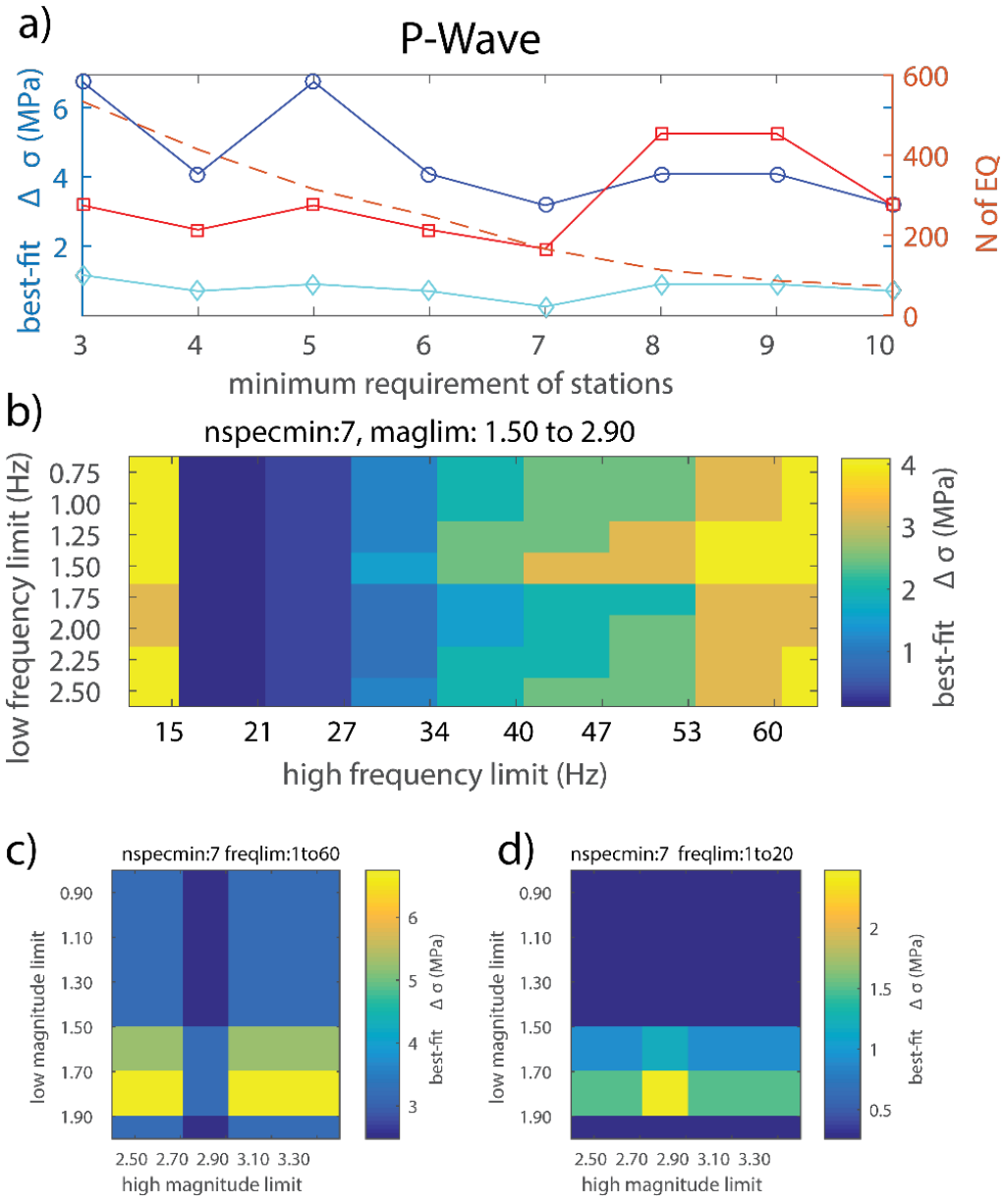

Figure 16. P-wave spectral stability tests. (a) Number of station requirement tests for a magnitude limit of 1.5 to 2.9, frequency limit of 1-60hz (blue), 1-40hz (red), 1-20(light blue). Dashed orange line is the number of events. (b) Frequency bins used and their effect on the stress drop. (c) Magnitude ranges effect on stress drop estimate for Brune 1-60hz (d) for 1-20 hz.

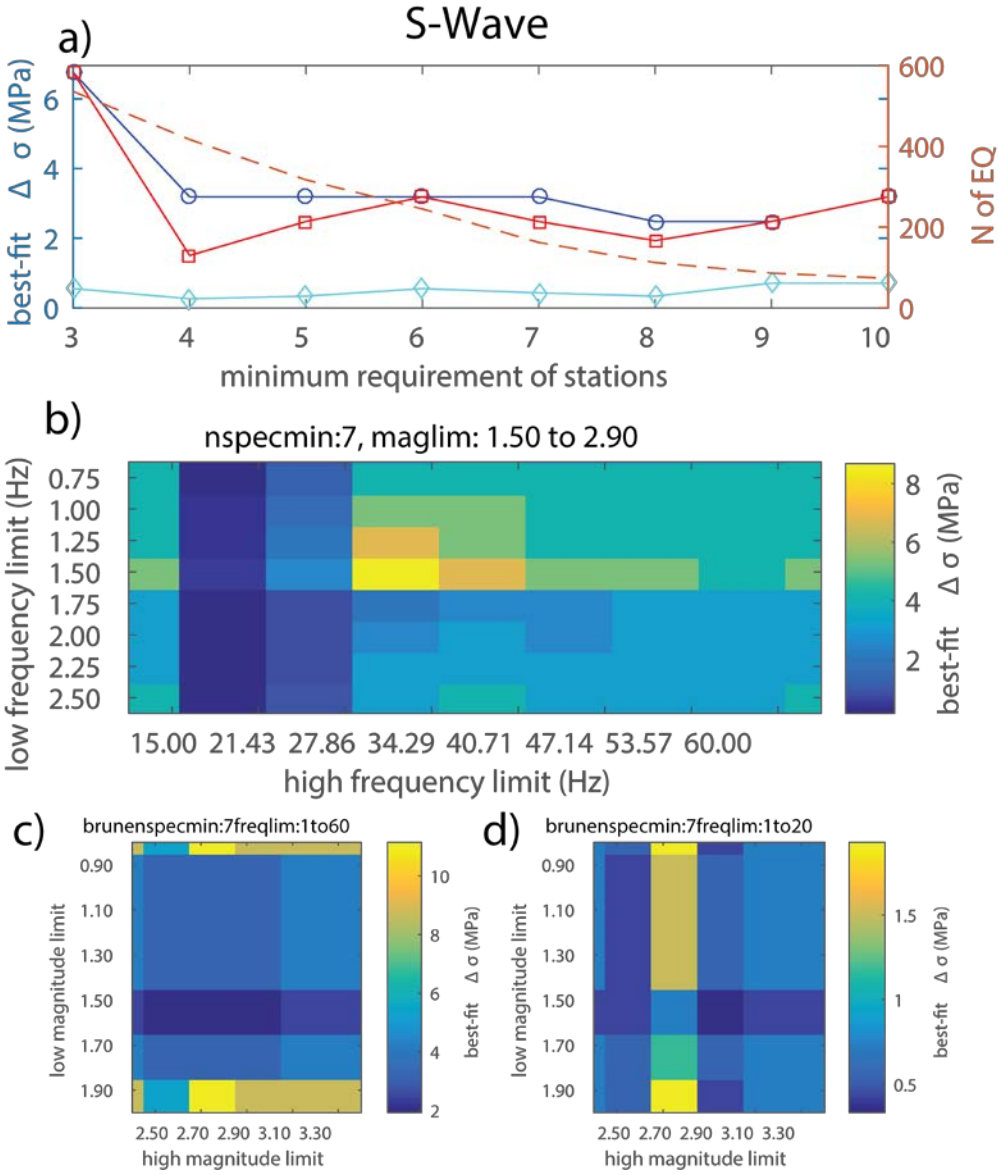

Figure 17. S-wave spectral stability tests. (a) Number of station requirement tests for a magnitude limit of 1.5 to 2.9, frequency limit of 1-60hz (blue),1-40hz (red), 1-20(light blue). Dashed orange line is the number of events. (b) Frequency bins used and their effect on the stress drop. (c) Magnitude ranges effect on stress drop estimate for Brune 1-60hz (d) for 1-20 hz.

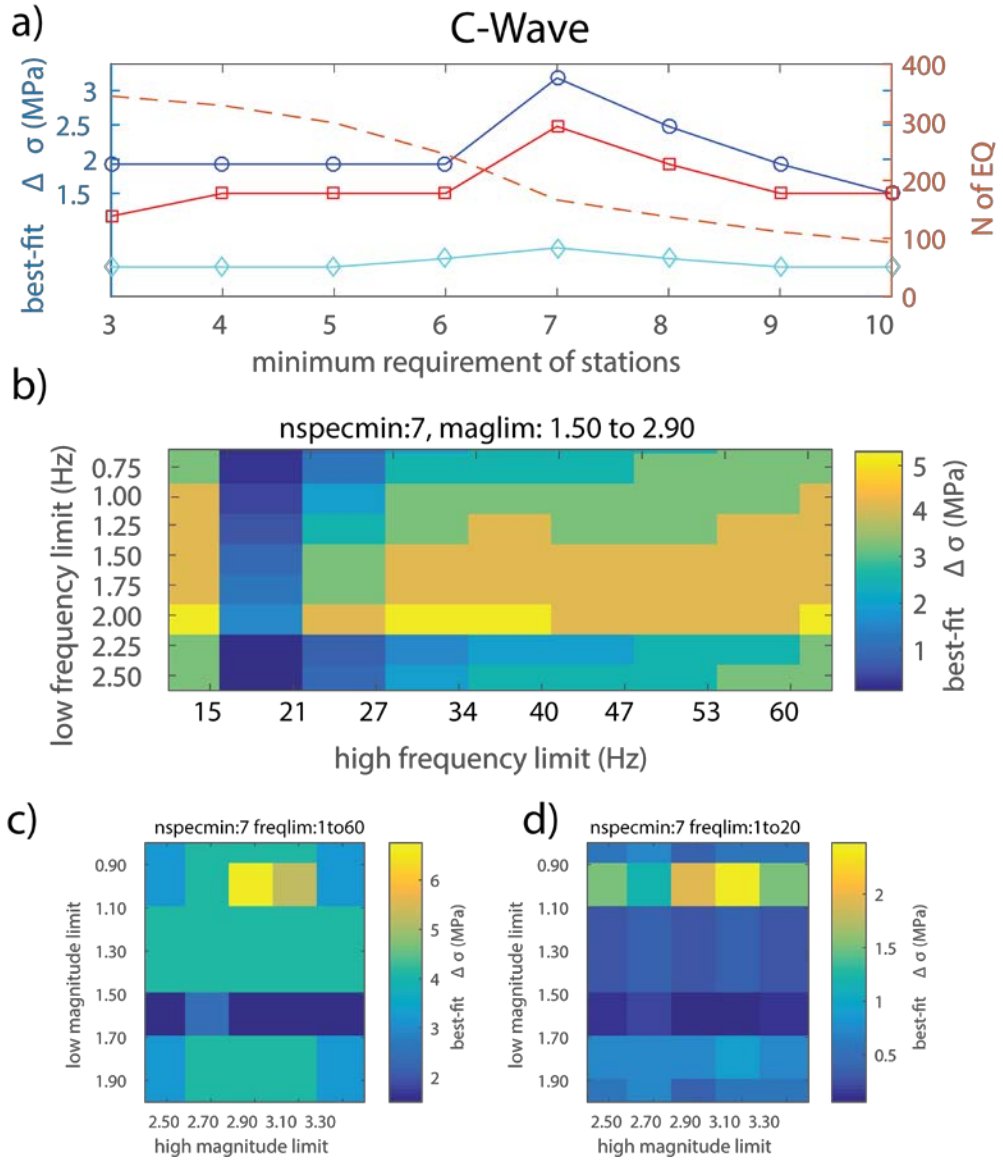

Figure 18. C-wave spectral stability tests. (a) Number of station requirement tests for a magnitude limit of 1.5 to 2.9, frequency limit of 1-60hz (blue),1-40hz (red), 1-20(light blue). Dashed orange line is the number of events. (b) Frequency bins used and their effect on the stress drop. (c) Magnitude ranges effect on stress drop estimate for Brune 1-60hz (d) for 1-20 hz.

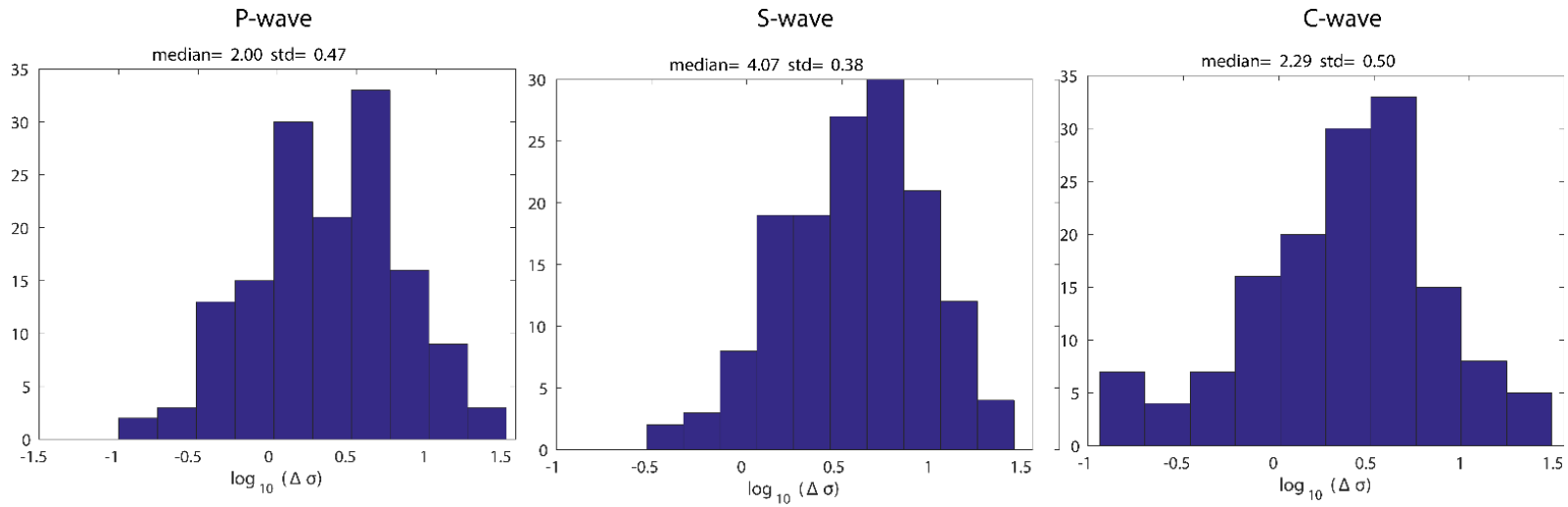

Figure 19. Histograms of the individual Stress drop estimates using the Brune model for the P,S, and Coda wave. Median and std are listed at the top of each figure.

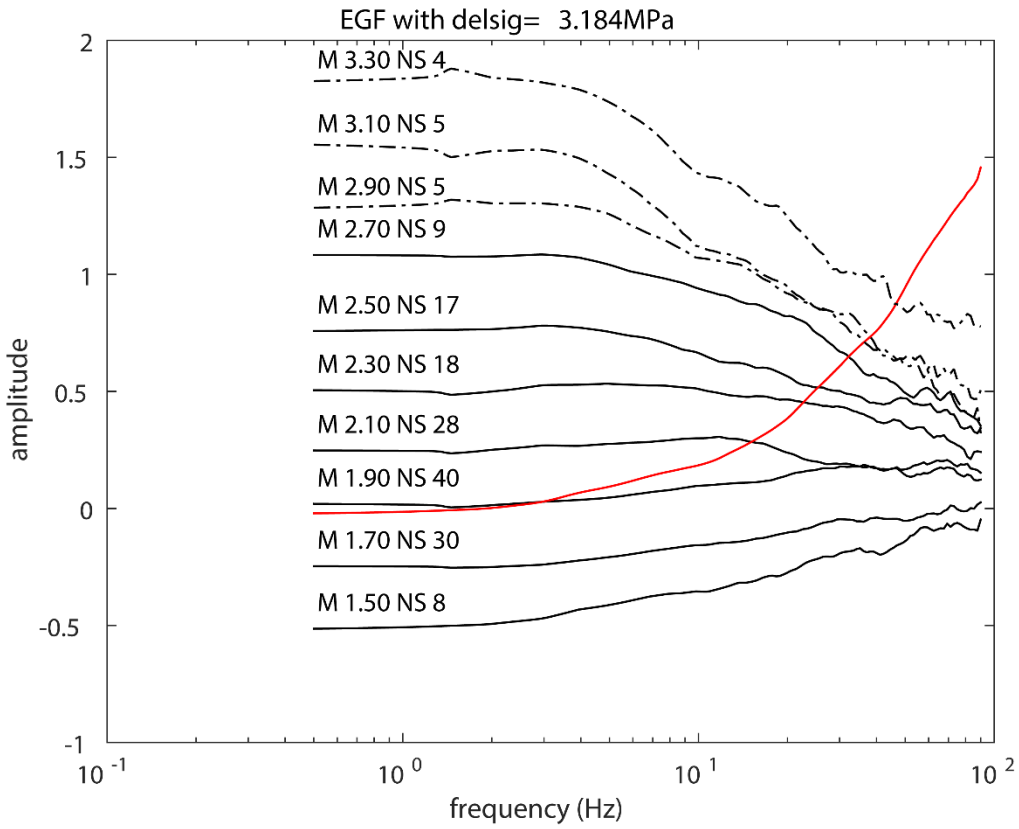

Figure 20. P-wave spectra before correction (Black lines), events are binned in 0.2 magnitude intervals (Dashed lines for bins with not enough events.). Regional EGF used for correction is plotted in red.

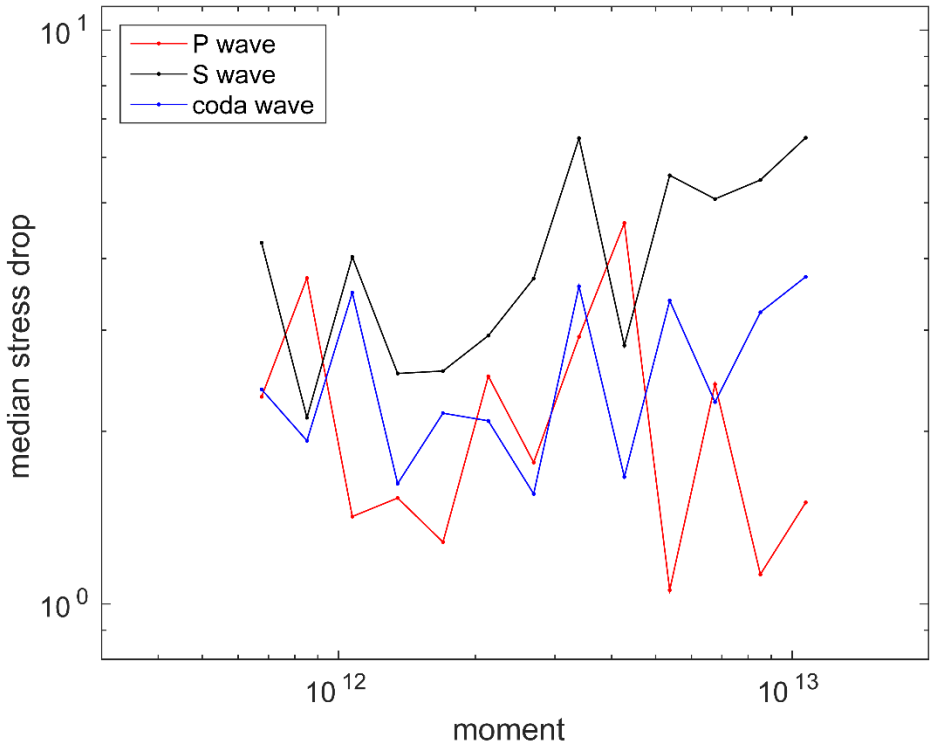

Figure 21. Comparison of median stress drop values verse moment, see legend for identification.

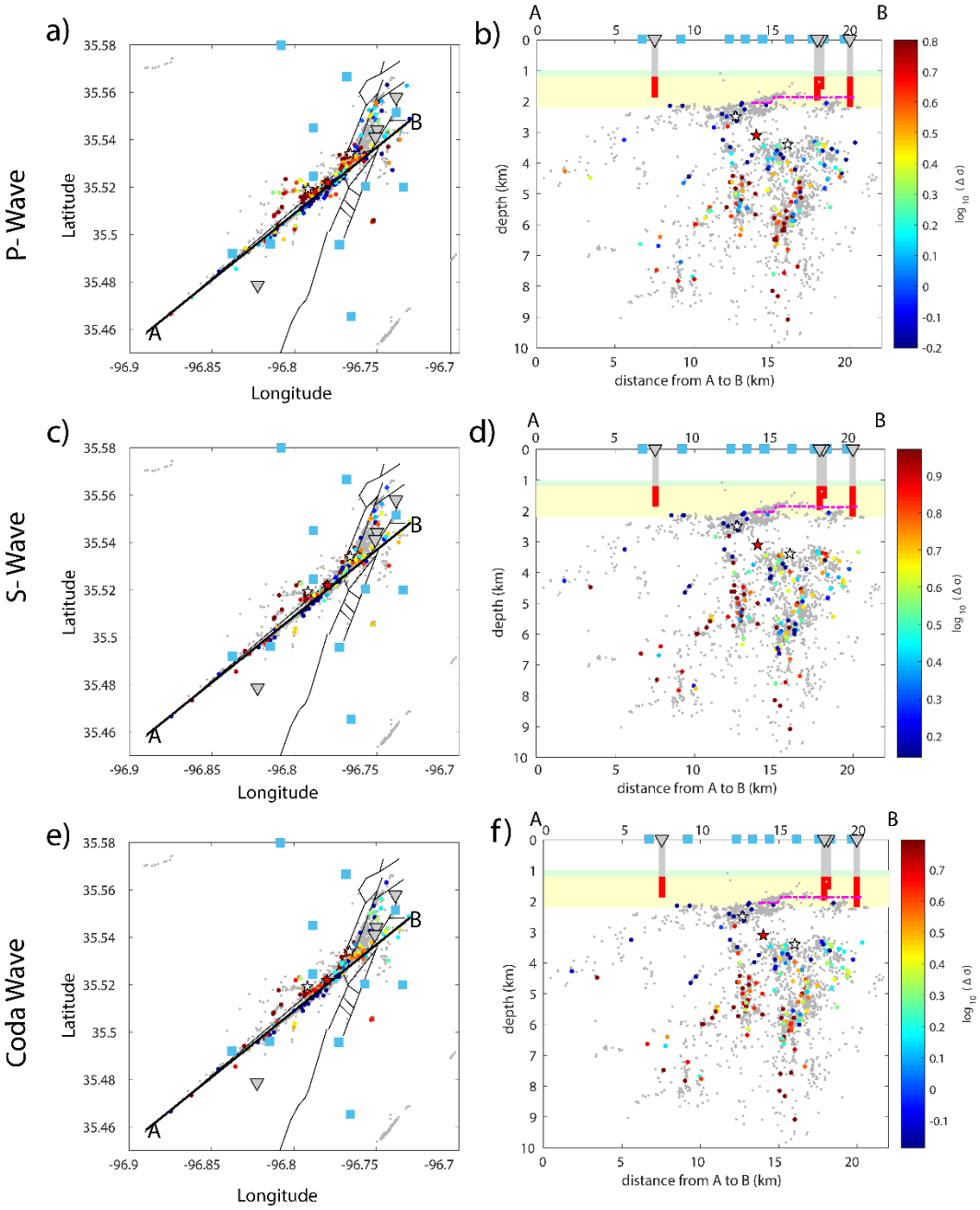

Figure 22 Comparison of P, S, and Coda wave spatial distribution (a, c, e) Map view of individual event stress drop estimates. Gray triangles are injection wells and blue squares are station locations, faults are drawn in black and cross section is thick black line. (b, d, f) Cross section A-B with Hunton group being the green bar, yellow bar is Arbuckle range, magenta is interpolated surface from Figure 13, and gray rectangles are injection wells with red portion representing injection interval.

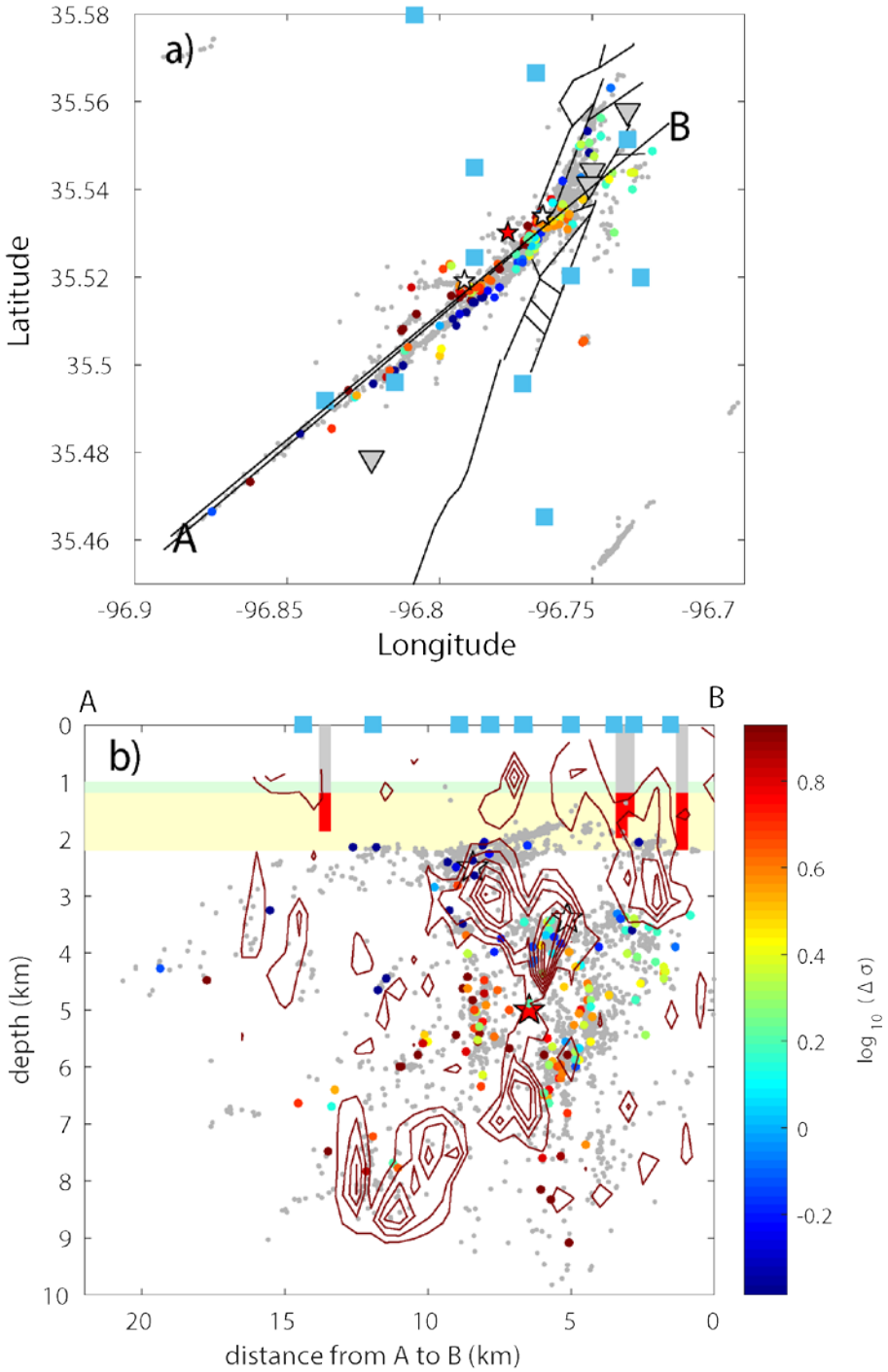

Figure 23. Stress drop results obtained from coda wave placed over the slip model obtained by [*Sun and Hartzell*, 2014]. (a) Map view of individual event stress drop estimates for the Coda wave. Gray triangles are injection wells and blue squares are station locations, faults are drawn in black and cross section is thick black line. (b) Cross section A-B with Hunton group being the green bar, yellow bar is Arbuckle range. Contours represent the slip experienced on the fault plane. Each contour represents an interval of 10 cm of slip

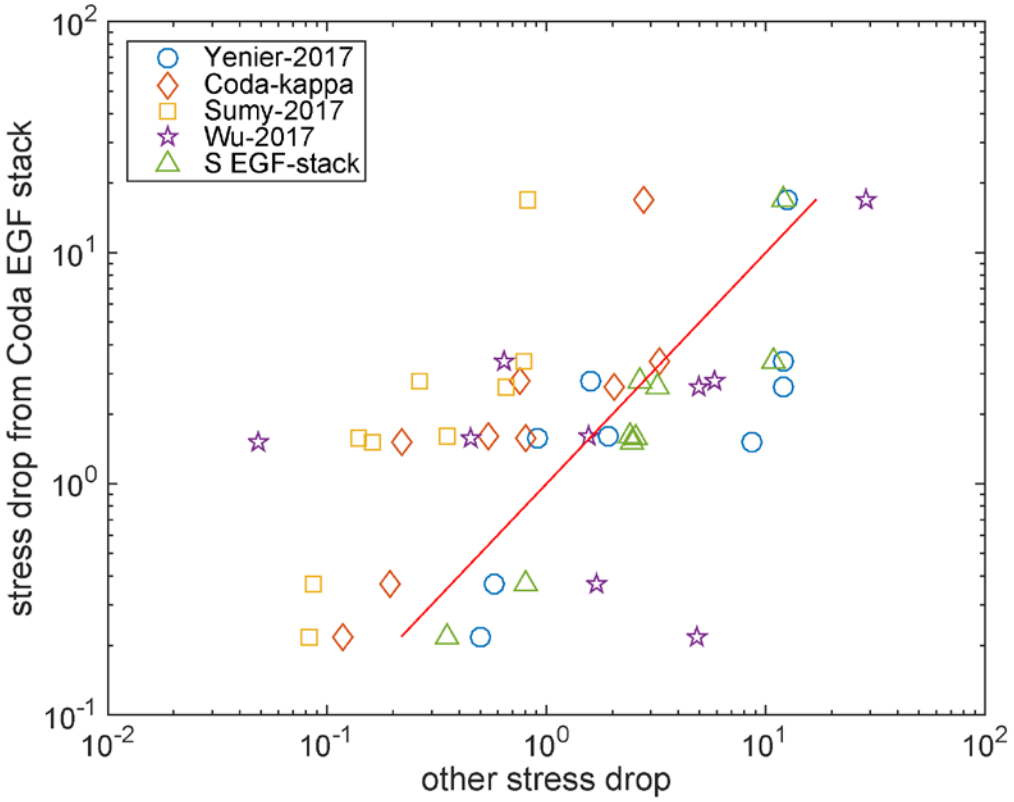

Figure 24. Comparison of stress drop results with other studies adjusted to the Brune stress drop calculation. Red line represents perfect fit with C-coda results.

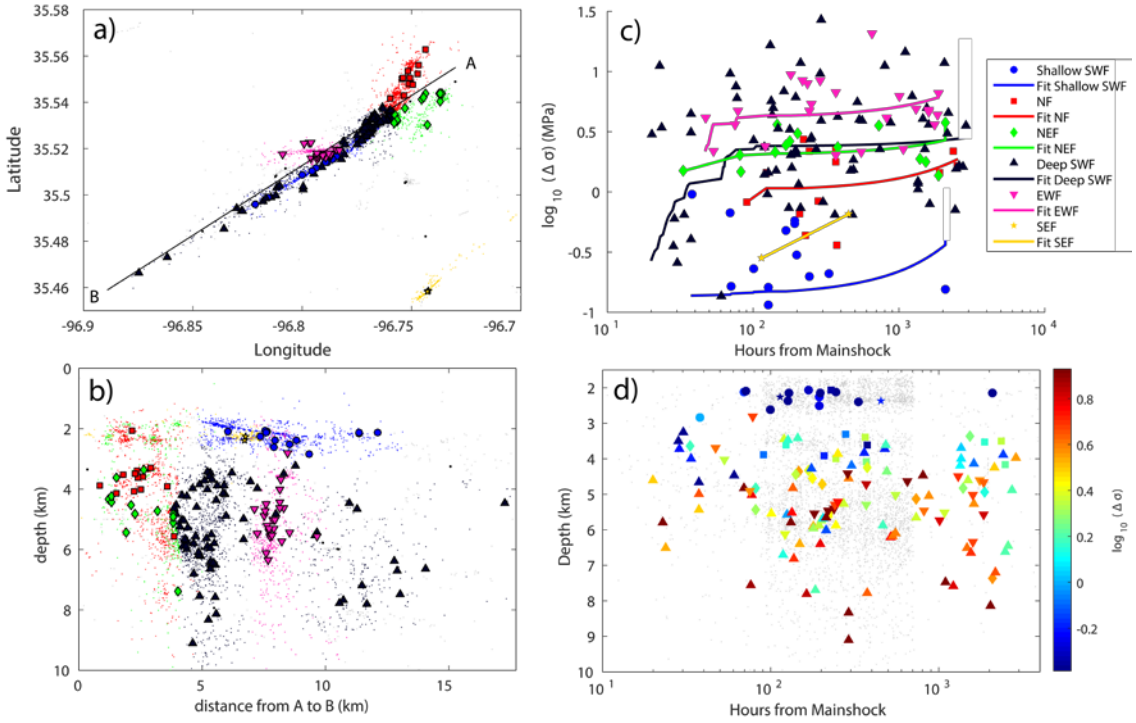

Figure 25. Map view of divided Prague cluster groups, with EGF corrected events shown with group symbol and non-EGF corrected as dots of the same group color. (B) Cross-section of A-B of divided groups. (C) Stress drop vs. Days from Mainshock with the linear fit drawn for each group. (D) Depth vs. Hours from Mainshock, with shapes colored to correspond with stress drop and gray events are all events in the cluster.

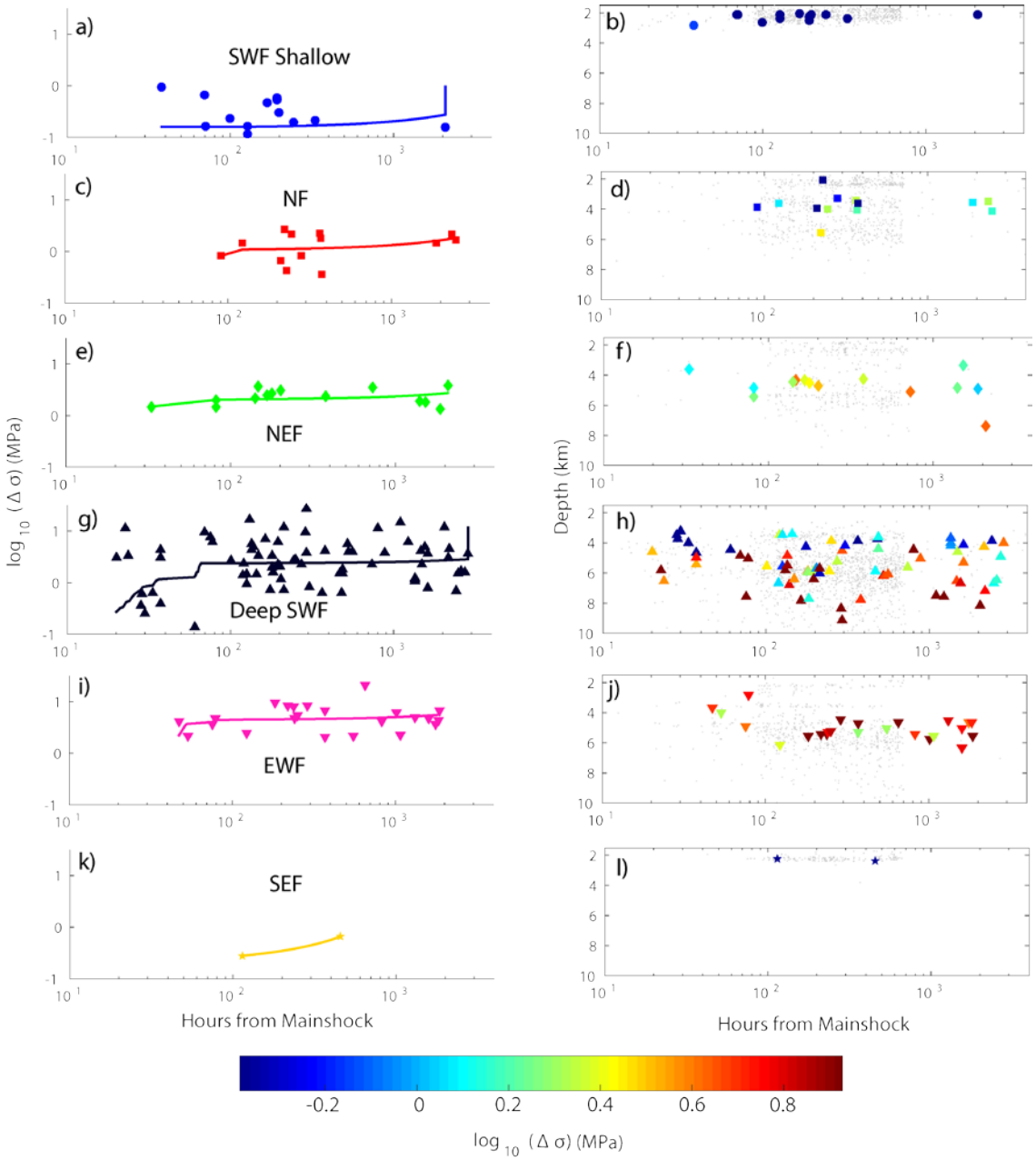

Figure 26. Separate plots of stress drop and depth over time for each individual group.

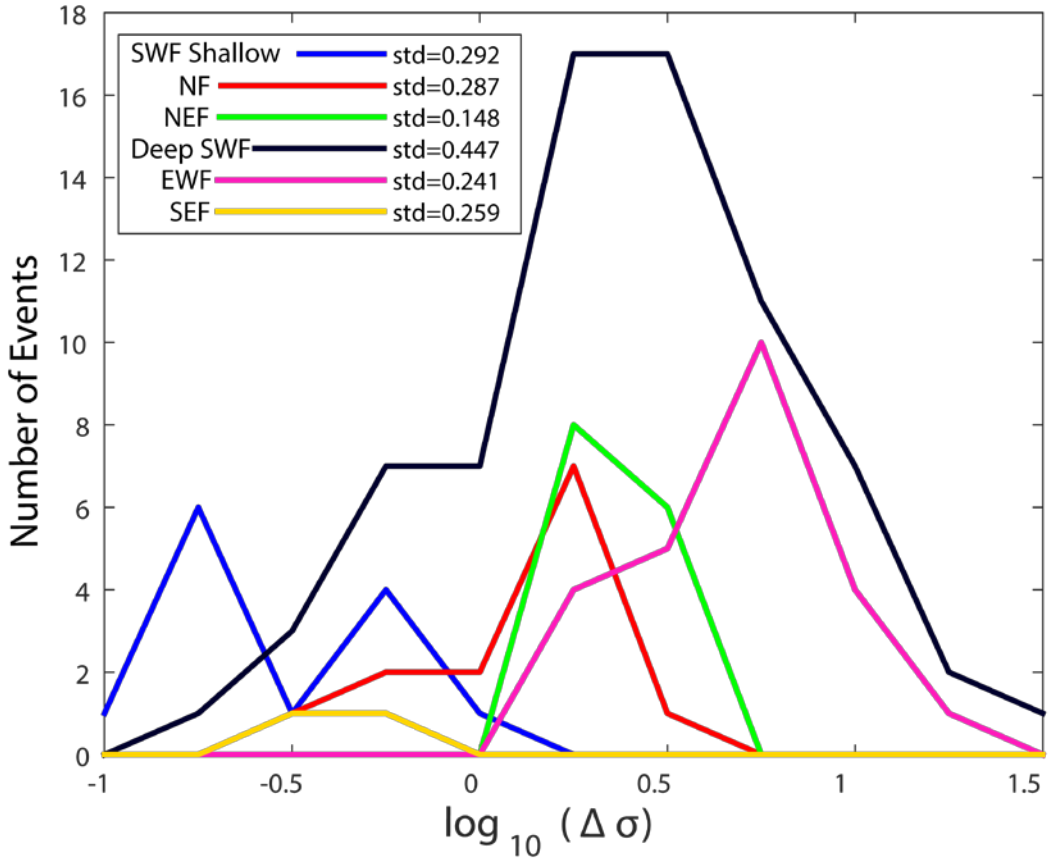

Figure 27. Histogram of stress drop for each group, with standard deviation for each group listed in the legend. With number of events plotted on the vertical axis and the log10 of stress drop plotted on horizontal axis.

Chapter 5: Pawnee

Introduction

The M5.8 Pawnee earthquake (magnitude from USGS) occurred at 12:02 UTC on September 3, 2016 and was felt throughout Oklahoma and neighboring states. The earthquake occurred near the junction of two previously mapped faults named the Watchorn fault and the Labette fault, but the source fault was a left-lateral unmapped basement fault (now known as the Sooner Lake fault, referred to as SLF) with a strike of 107°. The Sooner Lake fault is conjugate to a segment of the Labette fault that is optimally oriented (referred to as LF) in the present stress field [*Darold et al.*, 2015] (Figure 25 b). Within the Pawnee sequence, multiple episodes of earthquake bursts occurred within 200 days of the mainshock nearly simultaneously on the SLF and LF. Three M≥3.0 earthquakes occurred before the mainshock in the study area: the June 6, 2016 M_w3.7 (denoted as event A), the June 8, 2016 M_w3.6 (denoted as event B), and the September 1, 2016 M_w3 (denoted as event C). After the mainshock, the first M_w3.9 aftershock occurred on the LF 4.5 days after the mainshock on September 7, 2016.

It is well-established that most recent earthquakes in Oklahoma are due to anthropogenic activities, mostly related to wastewater disposal into the Arbuckle group, which is the predominant layer directly on top of the crystalline basement [*Walsh and Zoback*, 2015]. Previous studies suggest that the M5 foreshock to the 2011 M5.7 Prague earthquake and the 2016 M5 Fairview earthquake may have been triggered by nearfield and far field injection, respectively [*Keranen et al.*, 2013a; *Yeck et al.*, 2016a]. While the role of injection has been well studied in Oklahoma seismicity, the role of stress interactions between earthquakes is usually not discussed, but should be considered

when analyzing earthquake sequences. For example, the M5.7 Prague earthquake may have been promoted by the M5 foreshock via Coulomb stress transfer, pointing to a scenario of cascading failure from the initial injection induced M5.0 foreshock [*Sumy et al.*, 2014]. Pore pressure increases from fluid injection have also been directly linked to earthquake triggering [*Nur and Booker*, 1972; *Zoback and Harjes*, 1997]. In this study, I seek to understand the roles of static Coulomb stress transfer in the occurrence of foreshocks, mainshock, and aftershock sequences. I first analyze detailed fault plane solutions for earthquakes with adequate first-motion picks, and then use Coulomb 3.4 to analyze the static stress transfer between foreshocks and the mainshock, as well as between the mainshock and subsequent earthquakes.

Data

In the weeks following the earthquake, I deployed twenty short-period stations from the Incorporated Research Institutions of Seismology (IRIS), and the United States Geological Survey (USGS) deployed eight stations (Figure 28 a-b). The twenty IRIS stations and five of the USGS stations are streaming data to the Oklahoma Geological Survey (OGS) in real-time, while the other stations need to be serviced manually. For this study, I only used the real-time stations in this area, as data from the offline stations are not yet available.

To obtain a complete and detailed view of the evolution of seismicity, I use the relocated catalog from *Chen et al*., [2017, under review]. The catalog is obtained via waveform cross-correlation and a 3D velocity model based on the double-difference algorithm, with a final estimated relative horizontal location error of 35 m and vertical location error of 200 m. I primarily use the double-difference catalog with relative

locations for analysis. However, I note that the seismicity preceding the mainshock was covered by far fewer stations than the aftershocks. To verify the effect of the location on the Coulomb stress analysis, I also test our results against the original 1D locations from the OGS catalog. For the mainshock, I examine stress changes using both the double-difference location and the published USGS location to examine the sensitivity of Coulomb stress changes as a function of hypocenter location. The USGS location uses more regional stations, but is based on a 1D regional velocity model, while the double-difference relocated catalog uses a 3D velocity model, so the relative location between the mainshock and foreshocks should be improved.

Method:

Focal Mechanism Determination:

I determine focal mechanisms with P-wave polarity picks with the program HASH [*Hardebeck and Shearer*, 2003]. The HASH algorithm computes takeoff angles from source to receiver and performs a grid search on all possible focal mechanisms to identify the most acceptable solutions for each earthquake. Due to the sparse station coverage before the mainshock, I require that foreshock events have at least three well constrained quadrants with a minimum of four polarity measurements in each quadrant, while the fourth quadrant needed a minimum of two polarity measurements (Figure 29). This allows for the inclusion of events as low as M_L 1.8, but does not represent a consistent level of magnitude completeness for the foreshock clusters. For the aftershocks of the mainshock, I require that each quadrant have at least four or more polarity measurements due to the improved station coverage. I obtain focal mechanism solutions for 54 events from February 22, 2016 to October 31, 2016, 36 of which

occurred after the mainshock. The earthquake catalog after the mainshock is complete down to a magnitude of M_L 2.8 (Figure 30). I primarily focus on foreshocks that occurred between the first M3.7 foreshock on June 6th, 2016 and the mainshock, to investigate the stress interactions among the foreshocks, mainshock and aftershocks within the conjugate fault system (SLF and LF). The majority of the earthquakes are strike-slip faulting events and the region is characterized by a transtensional regime. For earthquakes that occurred on the LF (or within 0.5 km of the fault), I choose the right-lateral nodal plane that best matches the mapped fault. For earthquakes that occurred on the SLF (or within 0.5 km of the fault), I choose the left-lateral nodal plane that best matches the orientation of the SLF as the primary fault plane. For other events, I do not distinguish primary and auxiliary nodal planes. The mainshock fault plane solution is obtained from regional waveform modeling, and has a primary fault plane solution with a strike of 107°, a dip of 90°, a rake of 0°, and a rupture direction of 107° [Chen et al., 2017, under review].

Coulomb Stress Analysis:

The effective Coulomb stress is a function of the shear stress and the frictional strength of the material. The frictional strength is defined as the friction coefficient multiplied by the effective normal stress, which is the difference between normal stress and pore pressure. In Coulomb stress triggering analysis, failure is promoted when the Coulomb stress on the receiver fault increases. Following *King et al.* [1994], the Coulomb stress change (ΔCFS) is defined as:

$$\Delta CFS = \Delta\tau + \mu(\Delta\sigma + \Delta p)$$

where $\Delta\tau$ is the change in shear stress, $\Delta\sigma$ is the change in normal stress (positive when the receiver fault is unclamped), Δp is the change in pore pressure, and μ is the effective coefficient of friction, which typically ranges from 0.6 to 0.8 [*Harris*, 1998].

The shear stress and normal stress on a given fault can be affected by earlier earthquake activities [*Harris*, 1998; *Stein*, 1999; *Steacy et al.*, 2005; *Hainzl et al.*, 2010], dynamic stress changes due to passing seismic waves [*Gomberg et al.*, 2001, 2003] and even tidal stresses [*Stroup et al.*, 2007, 2009; *Crone et al.*, 2011]. Stress changes as low as 10 kPa can have an impact on nearby faults [*Stein*, 1999].

In the Pawnee area, wastewater injection has been in operation since the mid-2000s, causing a few kPa in pore pressure changes with reasonable model assumptions [*Barbour et al.*, 2016]. In areas with fluid flow, the pore pressure changes cannot be neglected. Following *Reasenberg and Simpson* [1992], I incorporate the effect of pore pressure by using a modified Coulomb criterion with an effective friction coefficient:

$$\Delta CFS = \Delta\tau + \mu'(\Delta\sigma)$$

where $\mu' = \mu(1 - \beta)$, with β being the Skempton's coefficient, and μ being the friction coefficient. The effective friction coefficient μ' ranges from 0 to 0.8 with a 0.2 increment.

I therefore examine the ΔCFS conditions that may have led to the mainshock rupture and early aftershocks with Coulomb 3.4 (coulombstress.org). This includes interactions between foreshocks, the mainshock, and aftershocks that occurred on mapped geological faults. I first examine the effect of three M3+ foreshocks, two of which occurred in early June 2016, and the third two days before the mainshock in September 2016. I then examine the effect of the mainshock on mapped geological

faults and individual aftershock nodal planes to assess earthquake hazards on regional fault systems.

Results

Three M3+ Foreshocks

The source faults for individual foreshocks are selected based upon the right-lateral nodal plane found using HASH. The first M≥3 event (denoted as A) occurred within 0.5 km of the mainshock epicenter (denoted as M), and ~3 km from the other two M≥3 foreshocks (denoted as B and C) on the LF (Figure 30). Thus, it is possible that the foreshock could have occurred on the left-lateral SLF, similar to the mainshock. However, after detailed examination of the sequence, I find that it occurred as the last event of a 5-day earthquake swarm, which strikes at 55°, consistent with the orientation of the LF (Figure 28 b). Therefore, I choose the right-lateral motion as the primary fault plane for this earthquake (however, it remains possible that the foreshock ruptured a segment on the left-lateral SLF, as there is hint for a small step-over within this foreshock sequence, so I also tested the left-lateral rupture plane on the mainshock rupture plane). For each foreshock, I model the fault dimension based on the empirical relationship for strike-slip faults in *Wells and Coppersmith* [1994], which is the default model in the Coulomb 3.4 software. In addition, I use the moment magnitude from the OGS catalog, and assume that the hypocenter is the event centroid. The parameters for each foreshock are listed in Table 1.

For each foreshock, we estimate the Coulomb stress change imparted to the hypocenters of subsequent events. I calculate the ΔCFS on both nodal planes for all events except the mainshock, for which I only estimate on the primary left-lateral nodal

plane based on directivity analysis [*Chen et al*., 2017, under review] and aftershock locations.

The ΔCFS at the mainshock hypocenter from each of the foreshocks is listed in Table 1 using USGS locations and double-difference locations, respectively. Using an effective friction coefficient of 0.4, I find that event A produced the most significant ΔCFS of 68 kPa (or 198 kPa with the hypoDD location), while events B and C produced a ΔCFS of 0.4 and 0.14 kPa respectfully and are two to three orders lower than event A, but all produced a positive ΔCFS (Figure 31 a, d, f). In total, the three foreshocks produced about 69 kPa (or 198 kPa with the hypoDD location) of positive ΔCFS at the mainshock hypocenter (Figure 32 a-b).

To examine the effect of the friction coefficient on the resulting ΔCFS, I vary μ' from 0 to 0.8 with an increment of 0.2. With the hypoDD location, the ΔCFS ranges from 114.5 kPa (at μ'=0) to 208.1 kPa (at μ'=0.8); with the USGS location, the ΔCFS ranges from 208.6 to -71 kPa (Table 3).

The difference between the ΔCFS at the two hypocenter locations mainly comes from the normal stress resolved on the mainshock nodal plane: the USGS location received negative normal stress changes, while the shear stress changes remain positive at both locations (Table 1). One possible explanation is that the 3D velocity model systematically shifted the foreshock locations away from locations obtained from the 1D velocity model [*Chen*, 2016], and the USGS location is located in the negative normal stress side lobe from the 3D relocated foreshock.

To further assess the sensitivity of locations on the ΔCFS, I examine the spatial distributions of ΔCFS over the entire mainshock rupture plane from the three

foreshocks (Figure 33 a). Event A produced an area of significant positive ΔCFS (10 to 2 kPa) at the eastern end of the mainshock rupture plane, which extends from 4.25 to 8 km in depth. It also produces positive ΔCFS at deeper depths (under 6 km) extending the entire fault length (Figure 33 b). Calculations using the left-lateral nodal plane of event A produces a large area of positive ΔCFS (10 to 2 kPa) that extends from 0-3 km along the rupture plane and to a depth of 8 km (Figure 33 c). Thus, both suggest that event A has promoted failure near mainshock hypocenter. Events B and C produced negative ΔCFS of 10-2 kPa at 4.25-6 km of depth, and positive change of 4-1 kPa from 6-7 km of depth on the eastern end of the rupture plane (Figure 33 a). The overall pattern of ΔCFS on the rupture plane does not change when using different friction coefficients. Overall, the majority of the mainshock rupture plane at depths below 6 km received a positive ΔCFS of 4-1 kPa from the foreshocks, with the area of positive ΔCFS near the mainshock suggesting that the foreshocks promoted failure in the region surrounding the hypocenter of the mainshock

In addition to the positive ΔCFS on the mainshock, the foreshocks also produced positive ΔCFS at the future sites of the aftershocks on both the SLF and LF. Event A promoted failure at aftershock locations within 2 km of mainshock (Figure 31 a-c). Event B promoted failure of event C, aftershocks along the LF (including the M3.9 aftershock on September 7th, 2016), and aftershocks within 2 km east of the mainshock along the SLF experienced a positive ΔCFS of 1-4 kPa (Figure 31 d-e). Event C promoted failure of events within close proximity to the LF (including the M3.9 aftershock on September 7th), and relatively insignificant (0.1 kPa) ΔCFS on the SLF (Figure 31 f-g).

Coulomb Stress on Mapped Faults from the Mainshock:

For the mainshock, most catalogs report a depth range from 4 to 9 km, with the exception of the Global Centroid Moment Tensor (GCMT) solutions, which reports a likely erroneous depth of 18 km. The reported moment magnitude ranges from M_w 5.6 (in the Saint Louis University catalog) to M_w 5.83 (USGS catalog). Based on a few trial tests with different source parameters, I find that the details of the specified source models do not significantly change our results in terms of the spatial distributions. It should be noted that the Coulomb stress calculation could not resolve the details within the assumed rupture plane, and within 1 km perpendicular to the fault plane. All catalogs report near-vertical dipping angles. Therefore, I choose a fault model that is consistent with early aftershock distributions: extending from 0.5 km to the west of the mainshock hypoDD hypocenter to a mapped structural "kink" about 4.25 km to the east of the mainshock along the SLF, where the fault strike changes by about 10° based on aftershock distributions. The depth extends from 4.25 to 9.75 km, and it experiences a peak slip of 0.4 m, and a total seismic moment of 5.04e 24 dyne cm (assuming a shear modulus of 30 GPa, which is typical for upper crustal rocks (e.g., *McGarr* [2014]), producing a moment magnitude of M_w 5.77, consistent with the waveform modeling result in *Chen et al*., [2017, under review]. The slip on the fault is tapered into five nested 1km by 1km rectangles at the edges of the fault patch using the default settings from Coulomb 3.4.

First, in order to confirm our model of the mainshock, I examine the Coulomb stress changes on the regional faults with individual rake angles that are selected based on the current fault map of Oklahoma. Along the SLF, both the mainshock rupture

plane and the eastern segment where the strike is rotated by 10° are selected to have left-lateral motion; all other mapped faults are selected to have right lateral motion, consistent with the LF segment. The SLF receiver fault segments are assumed to be vertical and extend from a depth of 4 km to 10 km based upon aftershock distributions. The other faults are placed based upon the current fault map [*Holland*, 2015] and are assumed to be 0 to 6 km in depth (Figure 34 a).

The SLF and LF faults all experienced significant positive ΔCFS of 150 to 500 kPa. The areas above and below the assumed mainshock rupture area receive positive ΔCFS greater than 500 kPa (Figure 34 b). The Labette Fault sections both north and south of the mainshock experience negative Coulomb stress, consistent with the lack of aftershocks in those areas. Overall these findings suggest that the aftershock patterns align with the areas of positive ΔCFS and areas with a lack of activity align with stress shadow regions. Overall, the map view is consistent with results in *Yeck et al.,* [2016b] who calculated ΔCFS on a receiver fault that is consistent with the orientation of the Labette fault.

Coulomb Stress Change on Aftershock Nodal Planes from the Mainshock:

In this analysis, I do not assume the regional stress state or fault geometry for aftershocks, but instead use individual nodal planes as receiver faults at each earthquake's hypocenter. For each aftershock, I do not specify the exact nodal plane I wish to calculate the ΔCFS value on, but instead examine the effect on both nodal planes. The final ΔCFS is computed from shear and normal stress changes with an effective friction coefficient of 0.4. Based on the mean ΔCFS resolved on both nodal planes, I find that 66.7% of the events receive positive ΔCFS and 33.3% experience

negative ΔCFS. This result is statistically robust and independent of the choice of nodal plane, as there are only three events for which the sign of the ΔCFS depends on the nodal plane (Figure 35). The statistics are also robust in terms of the friction coefficient, as the number of events that received a positive ΔCFS only changes by 1-2 events across the range of different friction coefficients (Table 4). The percentage is consistent with the previous study on Coulomb stress triggering in the Prague sequence [*Sumy et al*, 2014]. Most of the events that experience negative ΔCFS are located within the assumed mainshock rupture plane (i.e., within 2 km of the mainshock), where the calculation is subject to large uncertainties (Figure 32 c-d) [*Toda et al.*, 2012]. For these events, I note that they mostly receive a positive ΔCFS from the foreshocks (Figure 32 a-b), especially from the foreshocks A and B, suggesting that the foreshocks contribute to the triggering of events within the mainshock rupture plane.

Discussion:

The ΔCFS increase experienced by the M5.8 mainshock indicates static triggering by the foreshocks that occurred 90 days before the mainshock. Foreshock A produces 100-200 kPa of positive ΔCFS at the mainshock hypocenter and on a majority of the mainshock rupture plane, it also promoted failure for all subsequent foreshocks and most aftershocks within 2 km of the mainshock. The foreshocks B and C produced insignificant (0.1 to 0.01 kPa) positive ΔCFS at the mainshock hypocenter. Combining the ΔCFS from all three M≥3 foreshocks, many of the aftershocks along the eastern portion of the SLF experience a ΔCFS decrease, primarily due to the stress shadow, from event B (areas with negative ΔCFS), while the intersection of the LF and the SLF

experiences positive ΔCFS of 25 to 30 kPa (Figure 32 a-b), which is sufficient to promote earthquake activity on critically stressed faults [*Stein*, 1999].

The mainshock imparted up to 500 kPa of positive ΔCFS on the LF and both the eastern and western ends of the SLF (Figure 34 b), consistent with the aftershock distribution (Figure 32 c-d) and the findings of *Yeck et al.* [2016b], who found a similar spatial distribution of ΔCFS. The mainshock produced a positive ΔCFS for 66.7% of the aftershocks, similar to the effect of the Prague mainshock on aftershocks [*Sumy et al*. 2014]. The NS-trending Watchorn fault is not optimally oriented in the regional stress field [*Holland*, 2013; *Walsh and Zoback*, 2016], but received significant positive ΔCFS from the mainshock. Several dip-slip events with normal faulting components occurred at the southern end of the Watchorn fault (Figure 30, 32 a-d). Examination of the original unrelocated catalog from the OGS further validates that spatial distribution of the ΔCFS is generally stable (Figure 37). These observations suggest that near field static stress change is capable of triggering faults that are not optimally oriented in the regional stress field. In Figure 36, the specific receiver orientation does not affect the resolved shear stress changes on the nodal planes; it is the normal stress that would change with fault orientations [*Sumy et al.*, 2014]. I further validate that the effect of normal stress and the friction coefficient is relatively small in this analysis (Table 4), leading to robust triggering statistics.

Pawnee Conclusion:

In summary, I determined focal mechanism solutions for 54 events that had sufficient azimuthal coverage of P wave polarities in our study area.

- The three foreshocks promoted failure of the mainshock, with the greatest contribution from the M3.7 foreshock on June 6, 2016.
- The three foreshocks also promoted failure for aftershocks located near the intersection of the SLF and LF.
- The mainshock produced up to 500 kPa of positive ΔCFS on surrounding faults, which aligns with the spatial pattern of aftershocks.
- Of the 36 events that have occurred after the mainshock, 66.7% experience positive ΔCFS from the mainshock.

Our findings show that small magnitude events can lead to static stress triggering of larger magnitude events. The Coulomb stress change we find represents only the minimum amount of Coulomb stress change the fault mainshock experienced. We cannot account for the aseismic slip that was occurring at the time and the Coulomb stress change that it placed on the rupture plane of the mainshock. Earthquake interaction due to smaller earthquakes should also be taken into account with hazard analysis and forecasting, especially in an environment with critically stressed faults from long-term fluid loading.

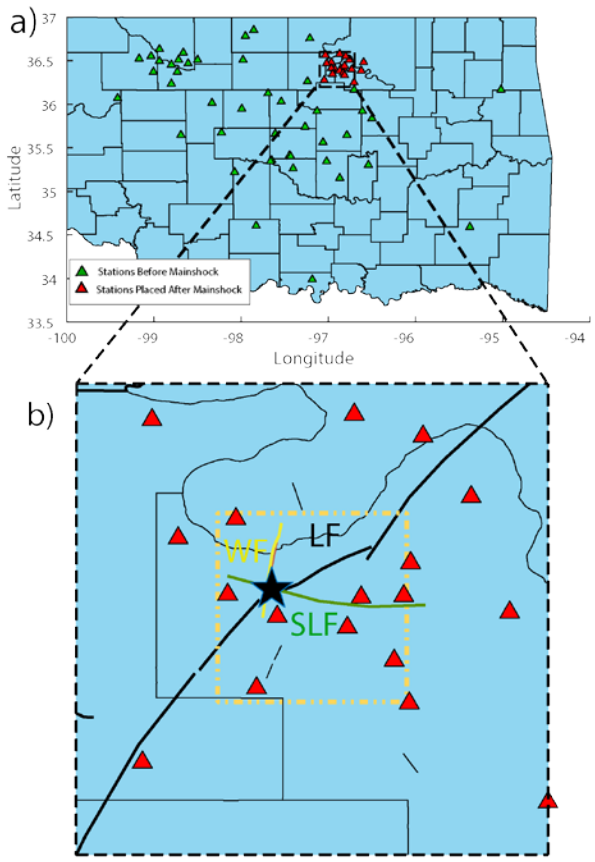

Figure 28. (a) Map view of the station locations in Oklahoma, with the station locations before the mainshock and the stations deployed after, see map legend for different stations. (b) Map view of the study area with the mainshock denoted by a star and stations deployed after it as squares. County lines are denoted in black with faults that were previously mapped in black as well. The Sooner Lake fault (SLF), Watchorn fault (WF), and the Labette fault (LF) are labeled. The orange dashed box represents the area shown in figure 30.

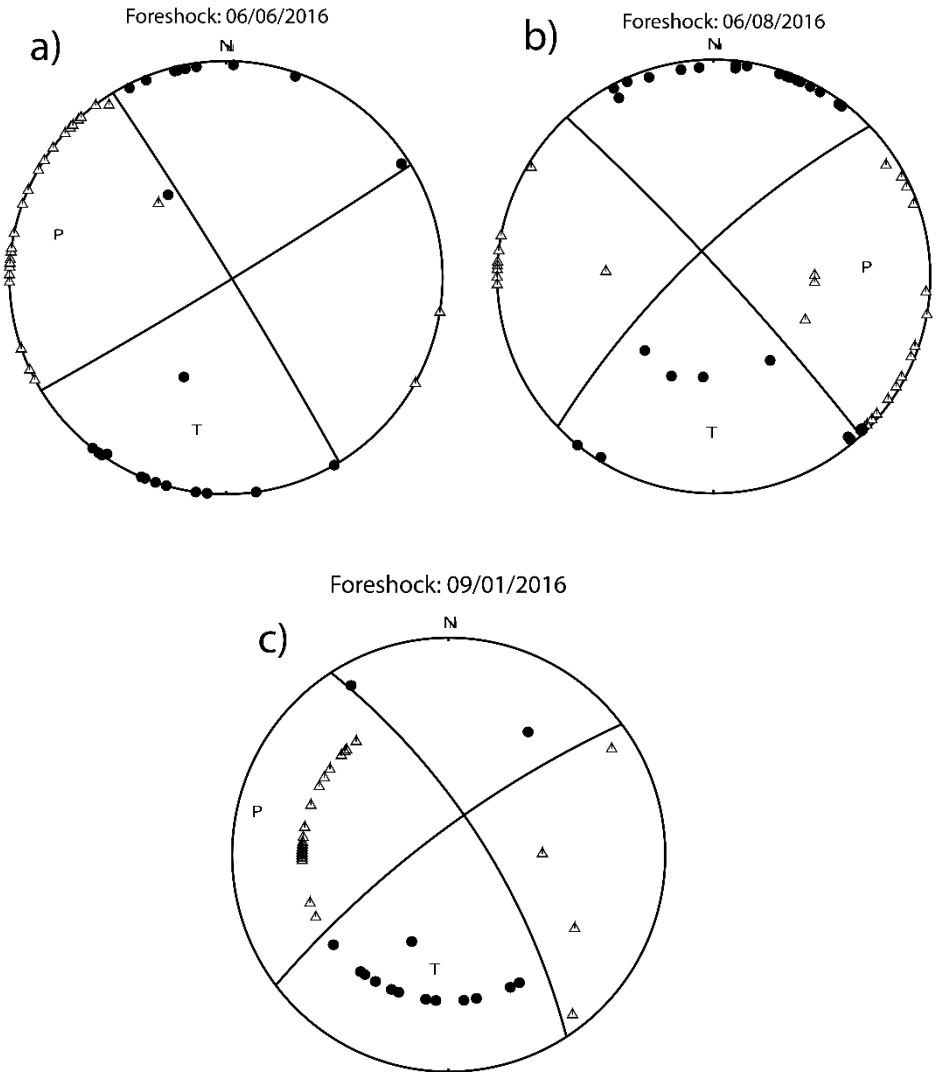

Figure 29. (a) – (c) Focal mechanisms for the three foreshocks obtained using HASH. North is denoted at the top of each focal mechanism with letter "N". The triangles are polarity measurements that represent dilation, circles represent polarity measurements that

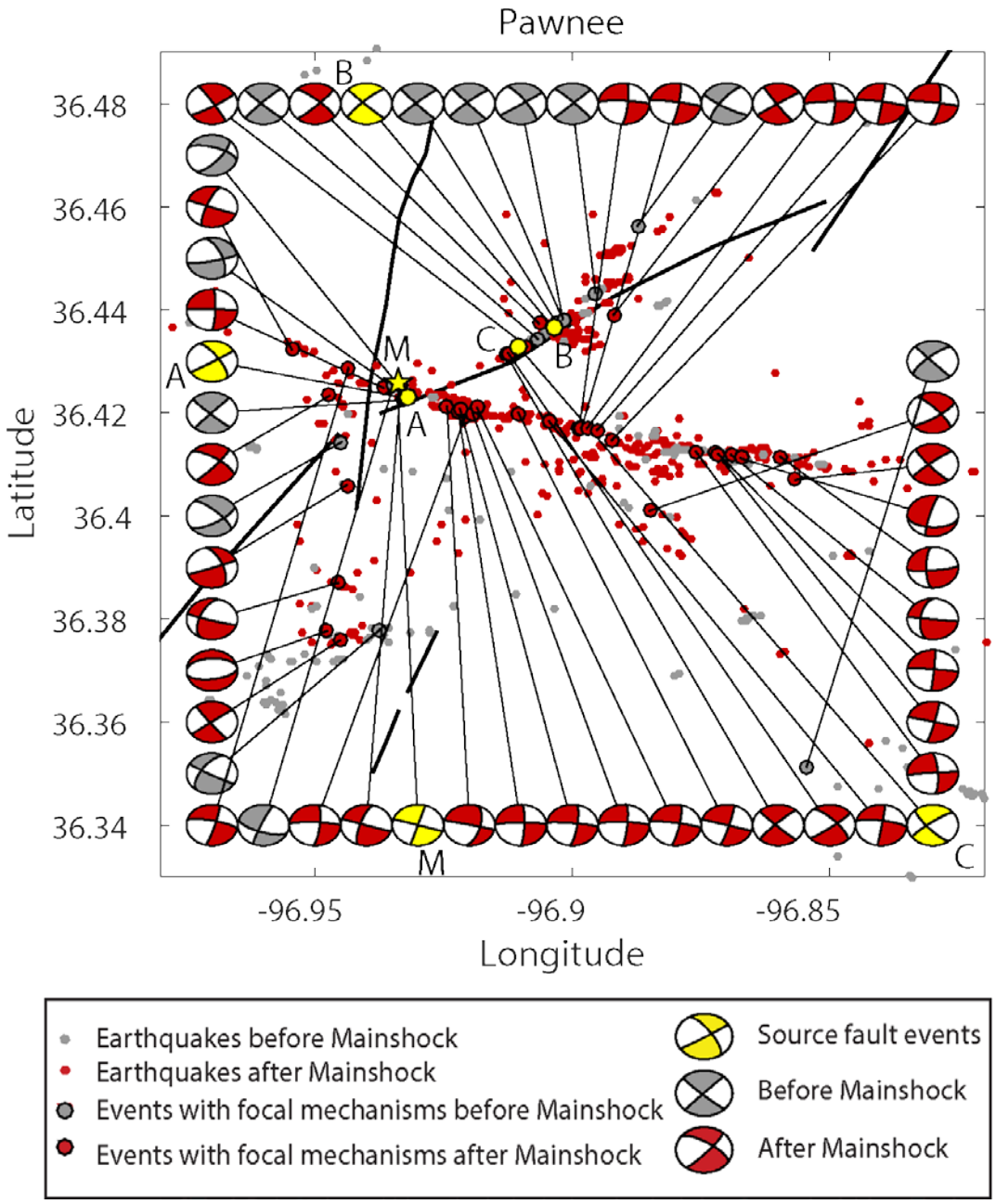

Figure 30. Map view of the 54 focal mechanisms that were obtained for our research area with previously mapped faults in black. The relocated earthquakes that occurred before the mainshock and after plotted, those that have focal mechanisms are circled in black and are linked to their corresponding focal mechanism, see map legend for different event types. The three foreshocks (A-C), and the mainshock (M) are labeled and are shown as source fault events.

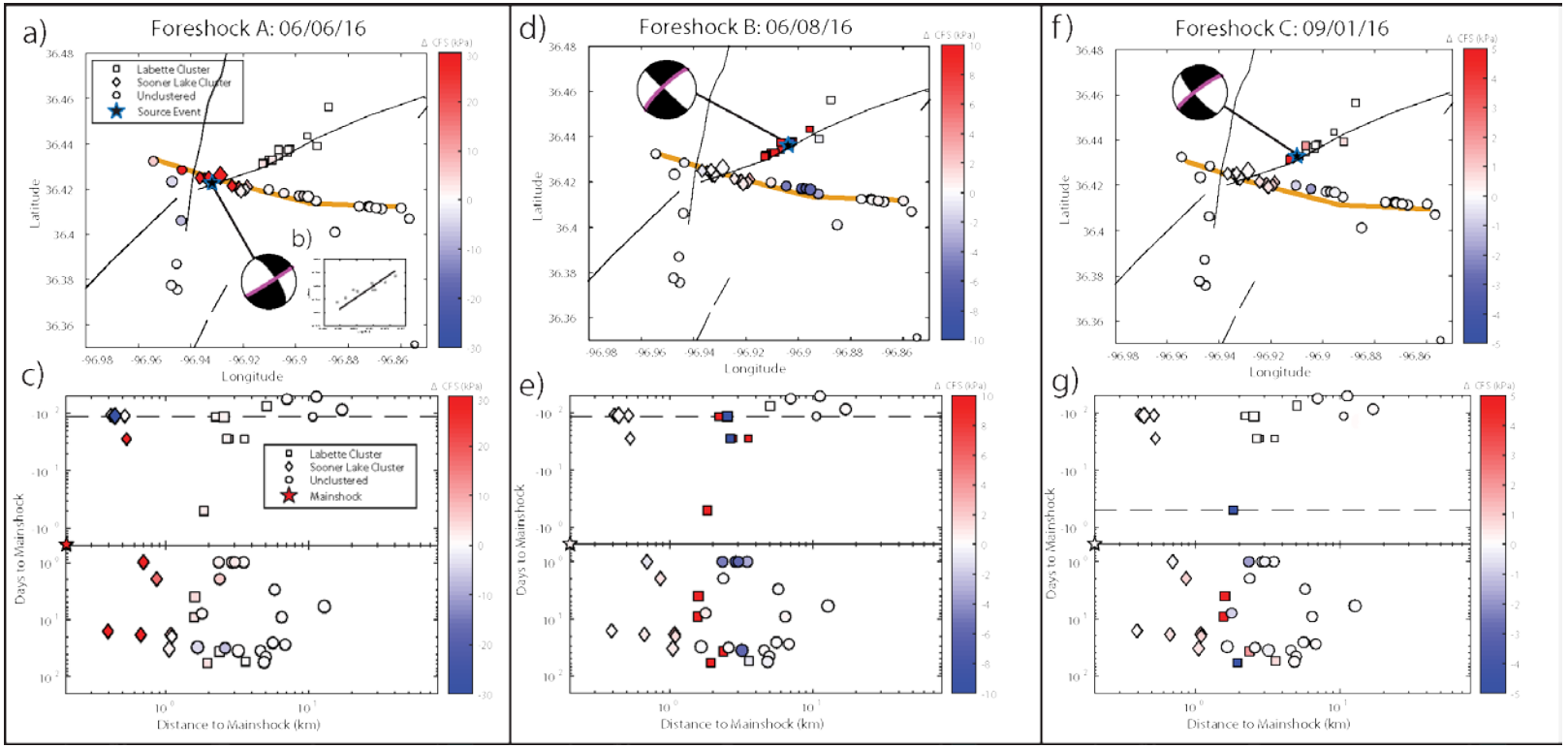

Figure 31. The mean ΔCFS experienced on between nodal plane and nodal plane 2, on each event. (a, d, f) Map views of ΔCFS from each foreshock: source event (star) and the corresponding focal mechanism with the nodal plane used in model is indicated on it. The events that occur near the mainshock vicinity (diamonds) are called the "Sooner Lake cluster", the events that occur in a cluster along the LF (squares) are referred to as the "Labette cluster", and all other events are called "unclustered" (circles) (see Map legend). (b) Zoomed-in map view of the foreshock cluster of foreshock A with the black line showing fault trend. (c, e, g) Distance to mainshock versus time to mainshock for each event. Both X and Y axes are in log scale. The dashed line shows the time of the corresponding source event. All events occurred prior to the source event are shown as white indicating no ΔCFS values were calculated.

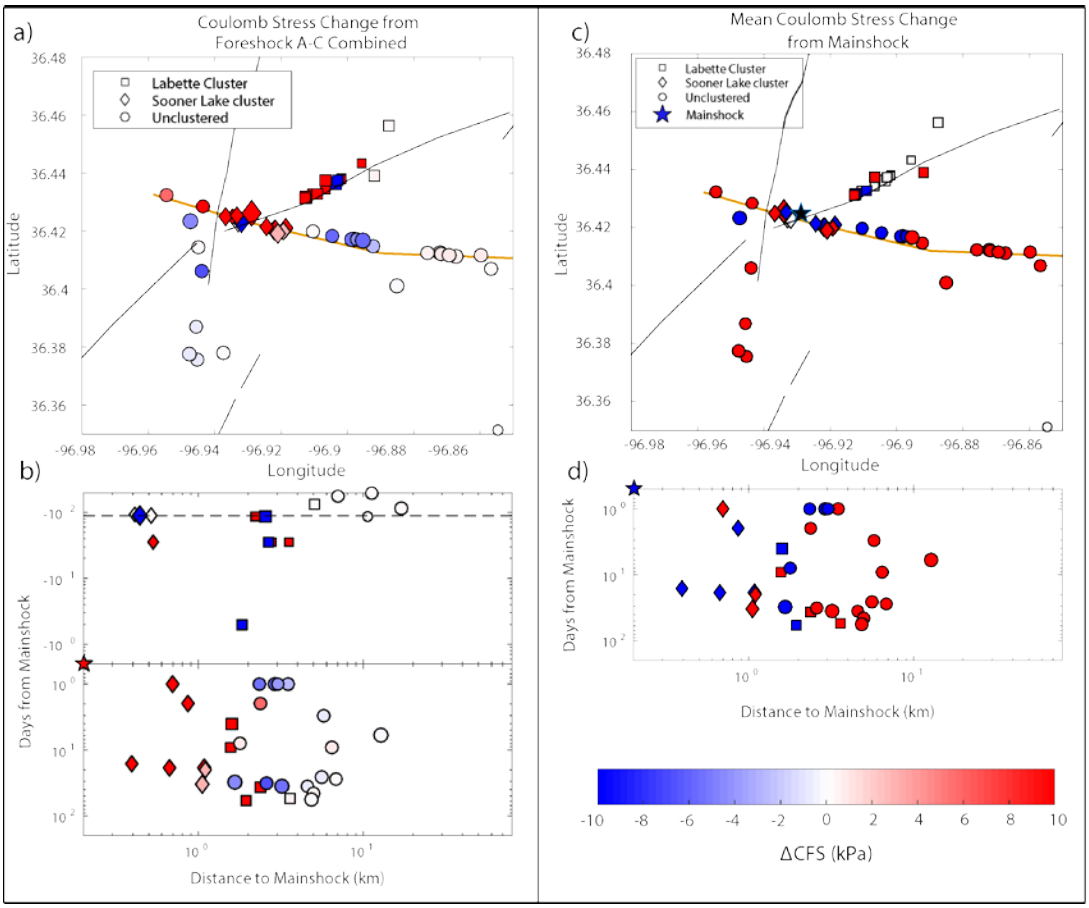

Figure 32. (a) Map view of the spatial distribution of combined mean ΔCFS of both nodal planes on the future hypocenters of subsequent events from foreshocks A-C, see map legend for different clusters. The Sooner Lake fault is the thicker line while the other faults are thin lines. (c) Spatial distribution of the mean ΔCFS of both nodal planes of each individual event from the mainshock. (b-d) Distance from the mainshock versus days from the mainshock, both are in log scale. Foreshocks are in negative time, and aftershocks are in positive time. The dashed line denotes the time of the first foreshock.

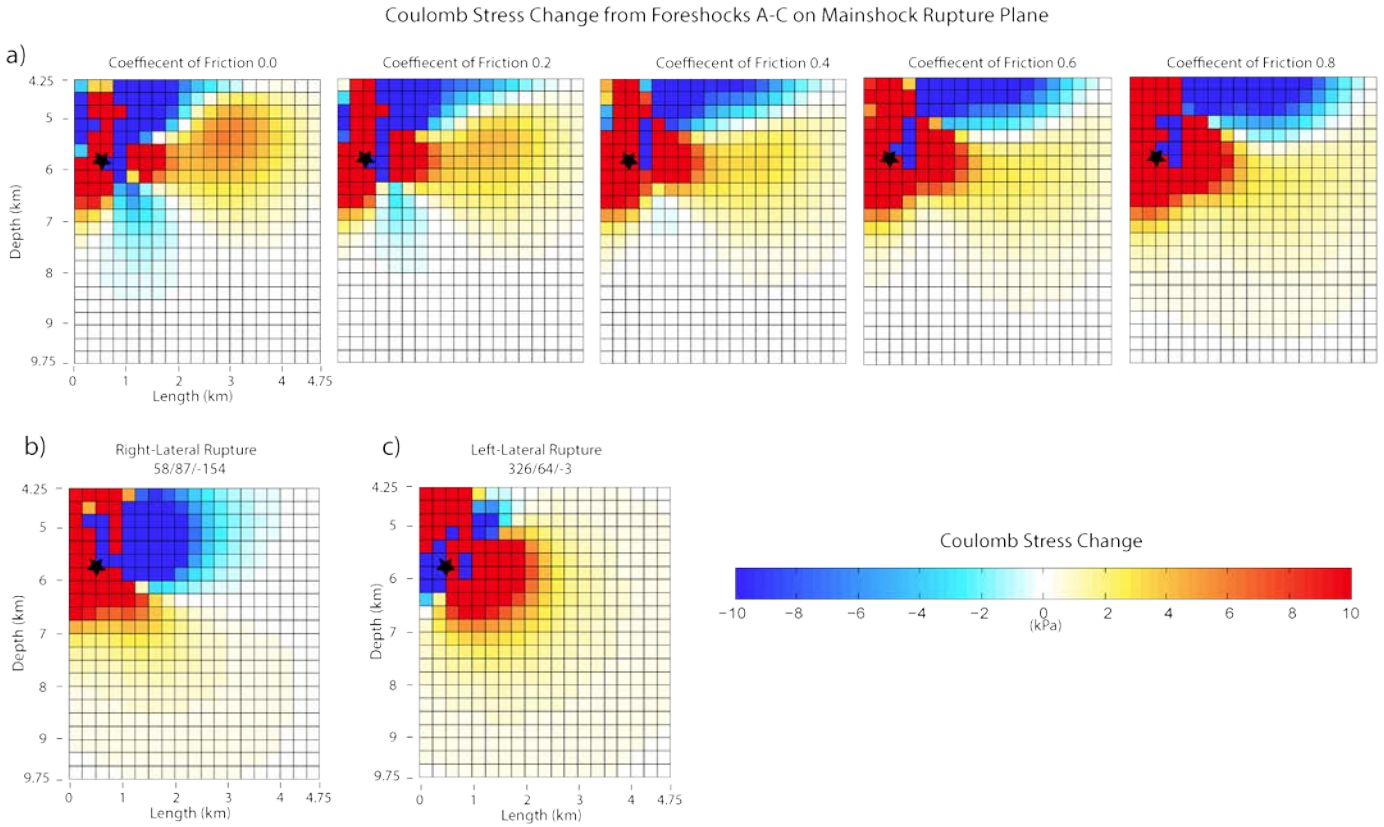

Figure 33. (a) The ΔCFS from foreshocks A-C on the rupture plane used in to model the mainshock rupture. The black star represents the depth location of the double difference relocation of the mainshock, with the USGS location being 0.3 km shallower. Each pane shows a different coefficient of friction used in the calculation and increases from left to right. (b) The ΔCFS from foreshocks A's right-lateral rupture plane on the mainshocks rupture plane. It was calculated using a coefficient of friction of 0.4 and has a strike, dip, and rake of 58/87/-154. (c) The ΔCFS from foreshocks A's left-lateral rupture plane on the mainshocks rupture plane. It was calculated using a coefficient of friction of 0.4 and has a strike, dip, and rake of 326/64/-3.

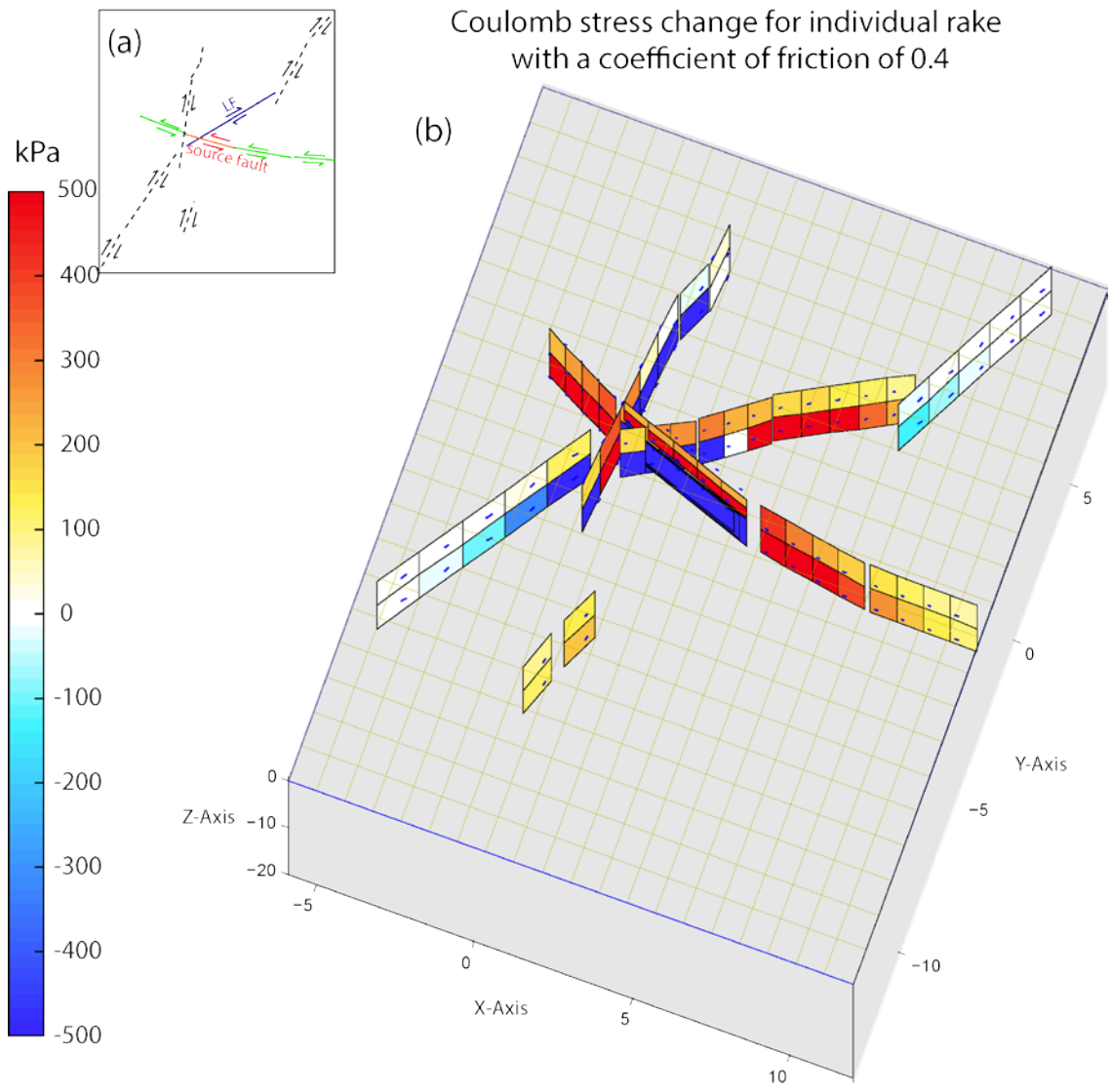

Figure 34. Modeled ΔCFS on nearby faults from the mainshock. (a) Summary of faults used in Coulomb stress calculation and their assumed directions of slip. The source fault that ruptured is labeled, the seismogenic fault outlined by the aftershocks are to the east and west of it, the LF is labeled, other previously mapped faults are dashed lines. (b) 3D view of ΔCFS on the surrounding faults rotated in the northeast direction. The X-axis is West to East, and Y is South to North directions.

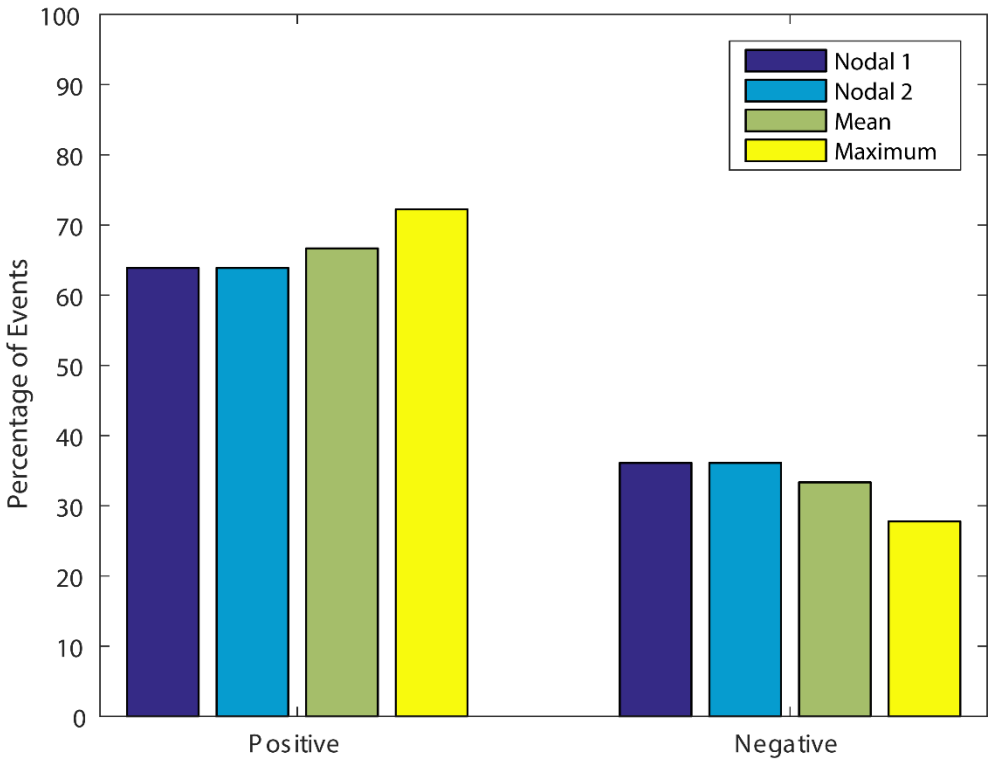

Figure 35. Percentage of events that experienced positive (triggered) and negative (not-triggered) ΔCFS on Nodal plane 1, Nodal plane 2, the mean of the two nodal values, and the maximum between the two nodal planes.

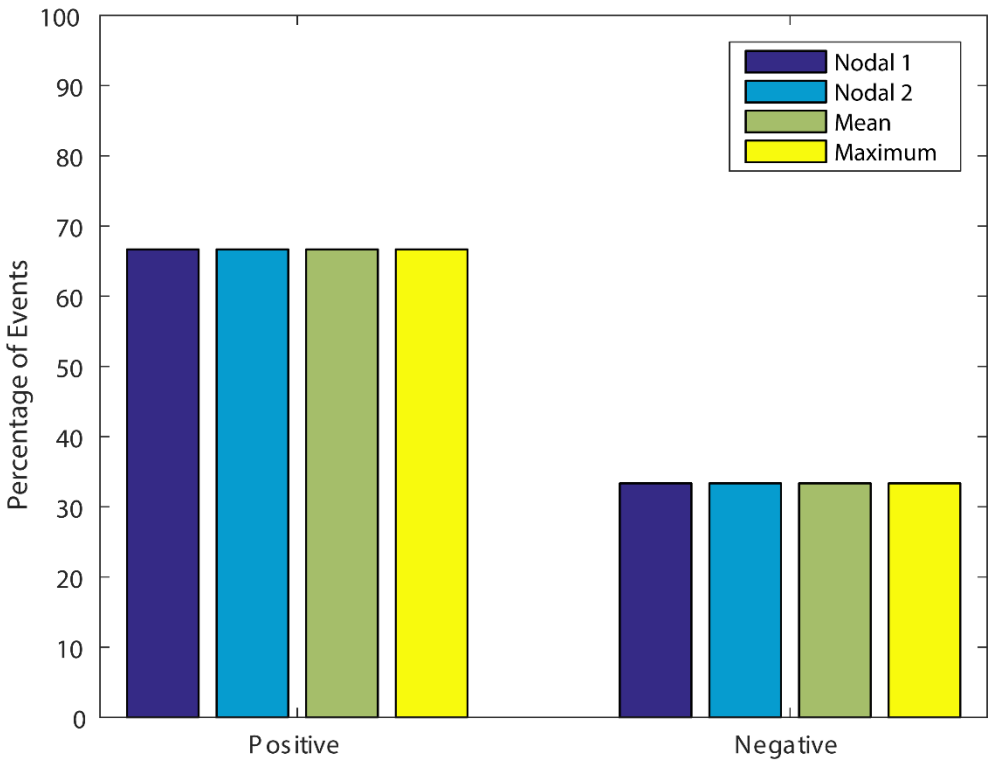

Figure 36. Percentage of events that experienced positive and negative shear stress on nodal plane 1, nodal plane 2, the mean of the two nodal values and the maximum between the two nodal planes.

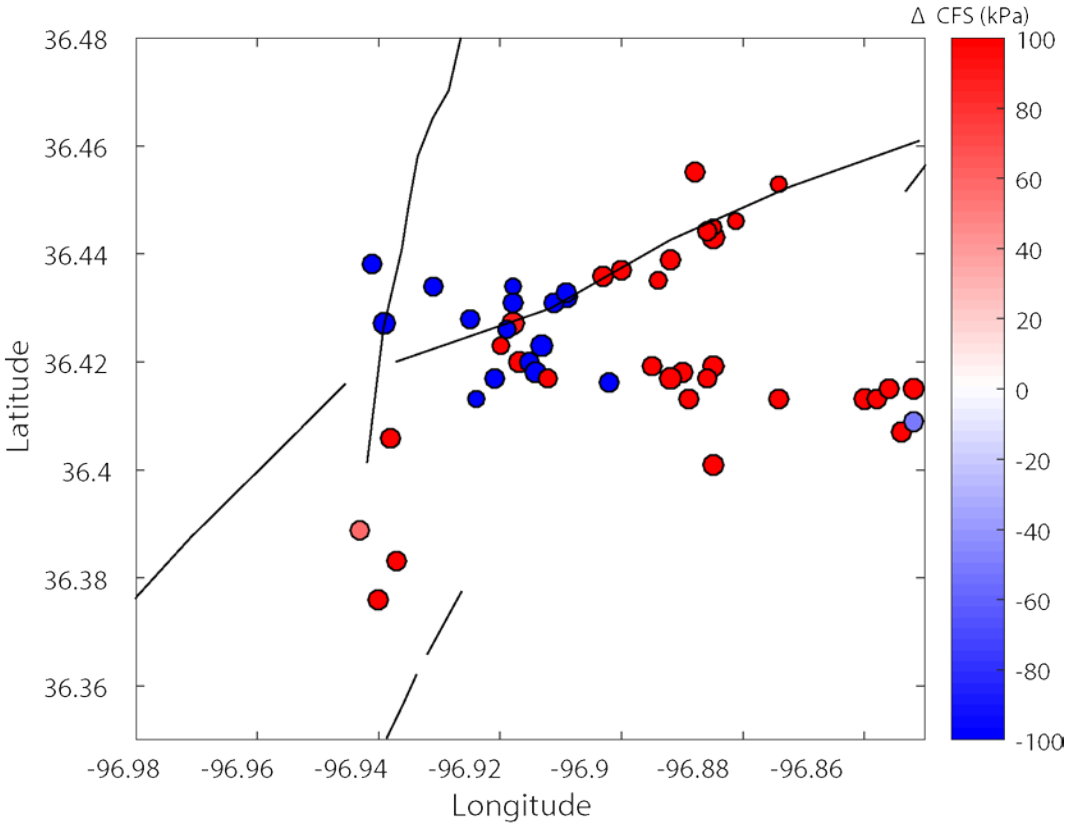

Figure 37. Map view of the mean ΔCFS from both nodal planes from the mainshock on the un-relocated aftershocks. Previously mapped faults are in black.

Event	Lat*	Lon†	Depth	Strike	Dip	Rake	Magnitude	Slip (m)	Rupture Width (km)	Rupture Length (km)
A	36.4327	-96.9104	4.25	233	78	-161	3.0	0.018	0.49	0.13
B	36.4365	-96.9037	4.46	226	76	-175	3.6	0.035	0.84	0.32
C	36.4228	-96.9320	5.4	58	87	-154	3.7	0.038	0.91	0.38

Table 1. List of the input source parameters for the three foreshocks. *Latitude †Longitude

Event	Location of mainshock hypocenter	Distance from mainshock	Shear Stress on Mainshock (kPa)	Normal Stress on Mainshock (kPa)	ΔCFS on mainshock (kPa)
A	USGS	0.45 km	208.6	-351	68.2
B	USGS	2.55 km	-0.2	1.5	0.6
C	USGS	1.82 km	0.03	0.3	0.14
Total:	USGS		208.4	-349.2	68.8
A	hypoDD	0.37 km	115	206.7	197.7
B	hypoDD	2.97 km	-0.5	1.2	0.3e-4
C	hypoDD	2.25 km	-0.04	0.2	0.04
Total:	hypoDD		114.5	208.1	197.7

Table 2. Results on the mainshock based on USGS location (36.4260, -96.9290), and based on double-difference (hypoDD) location (36.4257, -96.9340). Calculation was done using an effective coefficient of friction of 0.4 and ΔCFS is calculated on 107/90/0.

μ*	Location	ΔCFS nodal plane 1 107/90/0 (kPa)	ΔCFS nodal plane 2 197/90/-180 (kPa)	Mean of both nodal planes
0	USGS	208.6	208.5	208.5
0.2	USGS	138.6	188.4	163.5
0.4	USGS	68.8	168.4	118.6
0.6	USGS	-1.1	148.4	73.6
0.8	USGS	-71	128.4	28.7
0	hypoDD	114.5	114.5	114.5
0.2	hypoDD	156.1	98.9	127.5
0.4	hypoDD	197.7	83.3	140.5
0.6	hypoDD	239.3	67.8	153.6
0.8	hypoDD	208.1	52.2	166.6

Table 3. Combined ΔCFS (Coulomb stress change) from foreshocks A-C on USGS and double difference mainshock hypocenter location using different effective coefficients of friction. *Effective coefficient of friction

μ^*	Nodal Plane 1: Number of events receiving positive $\Delta CFS^\dagger$	Nodal Plane 2: Number of events receiving positive $\Delta CFS^\dagger$	Mean of both planes: Number of events receiving positive $\Delta CFS^\dagger$	Maximum of either plane: Number of events receiving positive $\Delta CFS^\dagger$
0	24	24	24	24
0.2	24	24	24	24
0.4	23	23	24	26
0.6	24	23	23	27
0.8	26	23	23	30

Table 4. Number of events receiving positive ΔCFS from the Mainshock, using different effective coefficients of friction. *Effective coefficient of friction, †Coulomb stress change

Chapter 6: Conclusion

I investigate the stress interaction inside different earthquake clusters to better understand the factors that might drive and control seismicity. For the Prague earthquake sequence using a relocated catalog we examined the seismogenic faults. Doing this we find that the sequence occurred along a number of anastomosing faults. We observe evidence that the fault rupture extended up into the Arbuckle formation. We also find that these shallow events show a pattern that mimics past interpreted structures in the Hunton formation.

I then examine the stress drop of the Prague earthquake sequence and find:

- A median stress drop of 2.21 MPa,
- Events occurring in the shallow region of 1.8 to 2.5 km, have lower stress drop than other areas of the fault system.
- The East-West trending fault has a higher average stress drop than the other segments of the fault system.
- Areas of low stress drop correlate with areas of high slip areas, while areas of higher stress drop correlate to areas of the fault that did not slip.

I then examined the Coulomb stress interactions before and after the Pawnee Mw 5.8 Earthquake. After determining focal mechanism for 54 events that had sufficient azimuthal coverage I found:

- The three foreshocks promoted failure of the mainshock, with the greatest contribution from the M3.7 foreshock on June 6, 2016.
- The three foreshocks also promoted failure for aftershocks located near the intersection of the SLF and LF.

- The mainshock produced up to 500 kPa of positive ΔCFS on surrounding faults, which aligns with the spatial pattern of aftershocks.
- Of the 36 events that have occurred after the mainshock, 66.7% experience positive ΔCFS from the mainshock.

Our findings for these two earthquake sequences allows for us to better quantify the dynamic and static stresses occurring within each of these sequences. The understanding of both factors and are necessary to accurately understand the hazard these sequence and future ones might pose. My analysis of the static stresses at Pawnee shows that the small magnitude foreshocks before large magnitude events can push critically stressed faults closer to failure. The observed Coulomb stress changes observed from the foreshocks also only indicate the minimum amount of Coulomb stress change, since we cannot properly quantify the Coulomb stress change from aseismic slip. These observations should be incorporated in the current hazard analysis of earthquake clusters in Oklahoma, since they might indicate, which areas are becoming critically stressed. The dynamic stress findings of Prague help us quantify what the damage might be from an eventual rupture. They indicate that the stress drops are generally lower, but currently linking this finding to injection is not possible given the lack of data. Overall the Prague sequence stress drop patterns exhibits features found in natural sequences, however the role of injection cannot be entirely ruled out.

References

Abercrombie, R. E. (2014), Stress drops of repeating earthquakes on the San Andreas Fault at Parkfield, *Geophys. Res. Lett.*, *41*(24), 8784–8791, doi:10.1002/2014GL062079.

Abercrombie, R. E. (2015), Investigating uncertainties in empirical Green's function analysis of earthquake source parameters, *J. Geophys. Res. Solid Earth*, *120*, 1–15, doi:10.1002/2015JB011984.Received.

Abercrombie, R. E., S. Bannister, J. Ristau, and D. Doser (2017), Variability of earthquake stress drop in a subduction setting, the Hikurangi Margin, New Zealand, *Geophys. J. Int.*, *208*(1), 306–320, doi:10.1093/gji/ggw393.

Allmann, B. P., and P. M. Shearer (2007), Spatial and temporal stress drop variations in small earthquakes near Parkfield, California, *J. Geophys. Res. Solid Earth*, *112*(4), 1–17, doi:10.1029/2006JB004395.

Allmann, B. P., and P. M. Shearer (2009), Global variations of stress drop for moderate to large earthquakes, *J. Geophys. Res. Solid Earth*, *114*(1), 1–22, doi:10.1029/2008JB005821.

Baltay, A., S. Ide, G. Prieto, and G. Beroza (2011), Variability in earthquake stress drop and apparent stress, *Geophys. Res. Lett.*, *38*(6), 1–6, doi:10.1029/2011GL046698.

Bell, M. L., and A. Nur (1978), Strength changes due to reservoir-induced pore pressure and stresses and application to Lake Oroville, *J. Geophys. Res.*, *83*(B9), 4469, doi:10.1029/JB083iB09p04469.

Boatwright, J. (1980), A spectral theory for circular seismic sources; simple estimates of source dimension, dynamic stress drop and radiated seismic energy, *Bull. Seismol. Soc. Am.*, *66*(3), 1271–1302.

Bourbié, T., O. Coussy, and B. Zinszner (1987), *Acoustics of porous media*, Gulf Publishing Company, Houston;

Boyd, O. S., D. E. McNamara, S. Hartzell, and G. Choy (2017), Influence of Lithostatic Stress on Earthquake Stress Drops in North America, *Bull. Seismol. Soc. Am.*, *107*(2), 856–868, doi:10.1785/0120160219.

Brune, J. N. (1970), Tectonic stress and the spectra of seismic shear waves from earthquakes, *J. Geophys. Res.*, *75*(26), 4997–5009, doi:10.1029/JB075i026p04997.

Calderoni, G., A. Rovelli, and S. K. Singh (2013), Stress drop and source scaling of the 2009 April l'Aquila earthquakes, *Geophys. J. Int.*, *192*(1), 260–274, doi:10.1093/gji/ggs011.

Calderoni, G., A. Rovelli, Y. Ben-Zion, and R. Di Giovambattista (2015), Along-strike rupture directivity of earthquakes of the 2009 L'Aquila, central Italy, seismic sequence, *Geophys. J. Int.*, *203*(1), 399–415, doi:10.1093/gji/ggv275.

Chen, X., and P. M. Shearer (2011), Comprehensive analysis of earthquake source spectra and swarms in the Salton Trough, California, *J. Geophys. Res. Solid Earth*, *116*(9), 1–17, doi:10.1029/2011JB008263.

Chen, X., R. E. Abercrombie, C. Pennington, X. Meng, and Z. Peng (2016), Source parameter validations using multiple-scale approaches for earthquake sequences in Oklahoma: implications for earthquake triggering processes, in *Abstract S13A-2515 presented at 2016 Fall Meeting, AGU*, San Francisco, Calif., 3-7 Dec.

Chen, X., N. Nakata, J. Haffener, C. Pennington, J. C. Chang, X. He, Z. Zhan, and S. Ni (2017), The Pawnee Earthquake as a result of the interplay among injection, faults and foreshocks, *Sci. Rep.*, 1–45.

Cotton, F., R. Archuleta, and M. Causse (2013), What is Sigma of the Stress Drop?, *Seismol. Res. Lett.*, *84*(1), 42–48, doi:10.1785/0220120087.

Crone, T. J., M. Tolstoy, and D. F. Stroup (2011), Permeability structure of young ocean crust from poroelastically triggered earthquakes, *Geophys. Res. Lett.*, *38*(5), 1–5, doi:10.1029/2011GL046820.

Darold, A. P., A. A. Holland, K. Jennifer, and A. R. Gibson (2015), Oklahoma Earthquake Summary Report 2014, *Oklahoma Geol. Surv. Open File Rep.*, *OF1-2015*.

van der Elst, N. J., H. M. Savage, K. M. Keranen, and G. A. Abers (2013), Enhanced Remote Earthquake Triggering at Fluid-Injection Sites in the Midwestern United States, *Science (80-.).*, *341*(September), 1380–1385, doi:10.1126/science.1238948.

Del Gaudio, S., M. Causse, and G. Festa (2015), Broad-band strong motion simulations coupling k-square kinematic source models with empirical Green's functions: the 2009 L'Aquila earthquake, *Geophys. J. Int.*, *203*(1), 720–736, doi:10.1093/gji/ggv325.

Goertz-Allmann, B. P., A. Goertz, and S. Wiemer (2011), Stress drop variations of induced earthquakes at the Basel geothermal site, *Geophys. Res. Lett.*, *38*(9), n/a-n/a, doi:10.1029/2011GL047498.

Gomberg, J., P. A. Reasenberg, P. Bodin, and R. A. Harris (2001), Earthquake triggering by seismic waves following the Landers and Hector Mine earthquakes, *Nature*, *411*(6836), 462–466.

Gomberg, J., P. Bodin, and P. A. Reasenberg (2003), Observing earthquakes

triggered in the near field by dynamic deformations, *Bull. Seismol. Soc. Am.*, *93*(1), 118–138, doi:10.1785/0120020075.

Hainzl, S., S. Steacy, and D. Marsan (2010), Theme V – Models and Techniques for Analyzing Seismicity Seismicity Models Based on Coulomb Stress Calculations, *Community Online Resour. Stat. Seism. Anal.*, (November), 1–25, doi:10.5078/corssa-32035809.

Hardebeck, J. L., and A. Aron (2009), Earthquake stress drops and inferred fault strength on the Hayward Fault, east San Francisco Bay, California, *Bull. Seismol. Soc. Am.*, *99*(3), 1801–1814, doi:10.1785/0120080242.

Hardebeck, J. L., and P. M. Shearer (2003), Using S/P amplitude ratios to constrain the focal mechanisms of small earthquakes, *Bull. Seismol. Soc. Am.*, *93*(6), 2434–2444.

Harris, R. a. (1998), Introduction to Special Section: Stress Triggers, Stress Shadows, and Implications for Seismic Hazard, *J. Geophys. Res.*, *103*(B10), 24347, doi:10.1029/98JB01576.

Hartzell, S., C. Mendoza, and Y. Zeng (2013), Rupture model of the 2011 Mineral, Virginia, earthquake from teleseismic and regional waveforms, *Geophys. Res. Lett.*, *40*(21), 5665–5670, doi:10.1002/2013GL057880.

Holland, A. A. (2013), Optimal Fault Orientations within Oklahoma, *Seismol. Res. Lett.*, *84*(5), 876–890, doi:10.1785/0220120153.

Holland, A. A. (2015), Preliminary fault map of Oklahoma, *Oklahoma Geol. Surv. Open File Rep., OF3-2015*.

Kanamori, H., and D. L. Anderson (1975), Theoretical Basis of Some Empirical Relations in Seismology, *Bull. Seismol. Soc. Am.*, *65*(5), 1073–1095, doi:??

Kane, D. L., D. L. Kilb, and F. L. Vernon (2013), Selecting Empirical Green's Functions in Regions of Fault Complexity: A study of Data from the San Jacinto Fault Zone, Southern California, *Bull. Seism. Soc. Am.*, *103*(2A), 641–650, doi:10.1785/0120120189.

Keller, R., and A. A. Holland (2013), Oklahoma Geological Survey March 22, 2013 statement on Prague earthquake, , (405), 7968.

Keranen, K. M., H. M. Savage, G. A. Abers, and E. S. Cochran (2013a), Potentially induced earthquakes in Oklahoma, USA: Links between wastewater injection and the 2011 Mw 5.7 earthquake sequence, *Geology*, *41*(6), 699–702, doi:10.1130/G34045.1.

Keranen, K. M., H. M. Savage, G. A. Abers, and E. S. Cochran (2013b), Potentially induced earthquakes in Oklahoma, USA: Links between wastewater

injection and the 2011 Mw 5.7 earthquake sequence, *Geology*, *41*(6), 699–702, doi:10.1130/G34045.1.

Keranen, K. M., M. Weingarten, G. A. Abers, B. A. Bekins, and S. Ge (2014), Sharp increase in central Oklahoma seismicity since 2008 induced by massive wastewater injection, *Science (80-.).*, *345*(6195), 448–451, doi:10.1126/science.1255802.

King, G., S. Stein, and J. Lin (1994), Static stress changes and the triggering of earthquakes, *Int. J. Rock Mech. Min. Sci. Geomech. Abstr.*, *84*(3), 935–953, doi:10.1016/0148-9062(95)94484-2.

Kwiatek, G., K. Plenkers, and G. Dresen (2011), Source parameters of picoseismicity recorded at Mponeng deep gold mine, South Africa: Implications for scaling relations, *Bull. Seismol. Soc. Am.*, *101*(6), 2592–2608, doi:10.1785/0120110094.

Kwiatek, G., F. Bulut, M. Bohnhoff, and G. Dresen (2014), High-resolution analysis of seismicity induced at Berlín geothermal field, El Salvador, *Geothermics*, *52*, 98–111, doi:10.1016/j.geothermics.2013.09.008.

Li, Z., and Z. Peng (2016), An Automatic Phase Picker for Local Earthquakes with Predetermined Locations: Combining a Signal-to-Noise Ratio Detector with 1D Velocity Model Inversion, *Seismol. Res. Lett.*, *87*(6), 1397–1405, doi:10.1785/0220160027.

Luza, K. V, R. F. Madole, and A. J. Crone (1987), Investigatiion of the Meers Fault in Southwestern Oklahoma, *Oklahoma Geol. Surv. Spec. Publ.*, *87–1*, 58.

McGarr, a (2014), Maximum magnitude earthquakes induced by fluid injection, *J. Geophys. Res. Solid Earth*, *119*(2), 1008–1019, doi:10.1002/2013JB010597.

Mcmahon, N. D., R. C. Aster, D. E. Mcnamara, H. M. Benz, and W. L. Yeck (2017), Spatio-temporal evolution of the 2011 Prague, Oklahoma aftershock sequence revealed using subspace detection and relocation., *Geophys. Res. Lett*.

McNamara, D. E., H. M. Benz, R. B. Herrmann, E. A. Bergman, P. Earle, A. Holland, R. Baldwin, and A. Gassner (2015), Earthquake hypocenters and focal mechanisms in central Oklahoma reveal a complex system of reactivated subsurface strike-slip faulting, *Geophys. Res. Lett.*, *42*(8), 2742–2749, doi:10.1002/2014GL062730.

Murray, K. E. (2014), Class II Underground Injection Control Well Data for 2010 – 2013 by Geologic Zones of Completion, *Oklahoma Geol. Surv. Open File Rep.*, *OF1-2014*, 32.

Neighbors, C., E. S. Cochran, K. J. Ryan, and A. E. Kaiser (2017), Solving for Source Parameters Using Nested Array Data: A Case Study from the Canterbury,

New Zealand Earthquake Sequence, *Pure Appl. Geophys.*, *174*(3), 875–893, doi:10.1007/s00024-016-1445-2.

Nur, A., and J. R. Booker (1972), Aftershocks caused by pore fluid flow?, *Science (80-.).*, *175*(4024), 885–887, doi:10.1126/science.175.4024.885.

Oth, A., and A. E. Kaiser (2013), Stress Release and Source Scaling of the 2010???2011 Canterbury, New Zealand Earthquake Sequence from Spectral Inversion of Ground Motion Data, *Pure Appl. Geophys.*, *171*(10), 2767–2782, doi:10.1007/s00024-013-0751-1.

Pacor, F., D. Spallarossa, A. Oth, L. Luzi, R. Puglia, L. Cantore, A. Mercuri, M. D'Amico, and D. Bindi (2016), Spectral models for ground motion prediction in the L'Aquila region (central Italy): Evidence for stress-drop dependence on magnitude and depth, *Geophys. J. Int.*, *204*(2), 697–718, doi:10.1093/gji/ggv448.

Pearson, C. (1981), The relationship between microseismicity and high pore pressures during hydraulic stimulation experiments in low permeability granitic rocks, *J. Geophys. Res. Solid Earth*, *86*(B9), 7855–7864, doi:10.1029/JB086iB09p07855.

Percival, D. B., and A. T. Walden (1993), *Spectral Analysis for Physical Applications*, Cambridge University Press, Cambridge.

Reasenberg, P. a, and R. W. Simpson (1992), Response of regional seismicity to the static stress change produced by the loma prieta earthquake., *Science*, *255*(5052), 1687–1690, doi:10.1126/science.255.5052.1687.

Rubinstein, J. L., and A. B. Mahani (2015), Myths and Facts on Wastewater Injection, Hydraulic Fracturing, Enhanced Oil Recovery, and Induced Seismicity, *Seismol. Res. Lett.*, *86*(4), 1060–1067, doi:10.1785/0220150067.

Shaw, B. E., K. Richards-Dinger, and J. H. Dieterich (2015), Deterministic model of earthquake clustering shows reduced stress drops for nearby aftershocks, *Geophys. Res. Lett.*, *42*(21), 9231–9238, doi:10.1002/2015GL066082.

Shearer, P. M., G. a. Prieto, and E. Hauksson (2006a), Comprehensive analysis of earthquake source spectra in southern California, *J. Geophys. Res.*, *111*, 1–21, doi:10.1029/2005JB003979.

Shearer, P. M., G. A. Prieto, and E. Hauksson (2006b), Comprehensive analysis of earthquake source spectra in southern California, *J. Geophys. Res. Solid Earth*, *111*(6), 1–21, doi:10.1029/2005JB003979.

Steacy, S., J. Gomberg, and M. Cocco (2005), Introduction to special section: Stress transfer, earthquake triggering, and time-dependent seismic hazard, *J. Geophys. Res. B Solid Earth*, *110*(5), 1–12, doi:10.1029/2005JB003692.

Stein, R. S. (1999), The role of stress transfer in earthquake occurrence, *Nature*, *402*(6762), 605–609, doi:10.1038/45144.

Stroup, D. F., D. R. Bohnenstiehl, M. Tolstoy, F. Waldhauser, and R. T. Weekly (2007), Pulse of the seafloor: Tidal triggering of microearthquakes at 9°50′N East Pacific Rise, *Geophys. Res. Lett.*, *34*(15), 1–6, doi:10.1029/2007GL030088.

Stroup, D. F., M. Tolstoy, T. J. Crone, A. Malinverno, D. R. Bohnenstiehl, and F. Waldhauser (2009), Systematic along-axis tidal triggering of microearthquakes observed at 9°50′N East Pacific Rise, *Geophys. Res. Lett.*, *36*(18), L18302, doi:10.1029/2009GL039493.

Sumy, D. F., E. S. Cochran, K. M. Keranen, M. Wei, and G. A. Abers (2014), Observations of static Coulomb stress triggering of the November 2011 M 5.7 Oklahoma earthquake sequence, *J. Geophys. Res. Solid Earth*, *119*(3), 1904–1923, doi:10.1002/2013JB010612.

Sumy, D. F., C. J. Neighbors, E. S. Cochran, and K. M. Keranen (2017), Low stress drops observed for aftershocks of the 2011 M W 5.7 Prague, Oklahoma earthquake, *J. Geophys. Res. Solid Earth*, doi:10.1002/2016JB013153.

Sun, X., and S. Hartzell (2014), Finite-fault slip model of the 2011 Mw 5.6 Prague, Oklahoma earthquake from regional waveforms, *Geophys. Res. Lett.*, *41*(12), 4207–4213, doi:10.1002/2014GL060410.

Talwani, P., and S. Acree (1985), Pore pressure diffusion and the mechanism of reservoir-induced seismicity, *Pure Appl. Geophys. PAGEOPH*, *122*(6), 947–965, doi:10.1007/BF00876395.

Thomson, D. J. (1982), Spectrum estimation and harmonic analysis, *Proc. IEEE*, *70*(9), 1055–1096, doi:10.1109/PROC.1982.12433.

Toda, S., R. S. Stein, G. C. Beroza, and D. Marsan (2012), Aftershocks halted by static stress shadows, *Nat. Geosci.*, *5*(6), 410–413, doi:10.1038/ngeo1465.

Trugman, D. T., and P. M. Shearer (2017a), Application of an improved spectral decomposition method to examine earthquake source scaling in southern California, *J. Geophys. Res. Solid Earth*, doi:10.1002/2017JB013971.

Trugman, D. T., and P. M. Shearer (2017b), GrowClust: A Hierarchical Clustering Algorithm for Relative Earthquake Relocation, with Application to the Spanish Springs and Sheldon, Nevada, Earthquake Sequences, *Seismol. Res. Lett.*, *88*(2A), 379–391, doi:10.1785/0220160188.

Vidale, J. E., W. L. Ellsworth, A. Cole, and C. J. Marone (1994), Variations in rupture process with recurrence interval in a repeated small earthquake, *Nature*, *368*(6472), 624–626, doi:10.1038/368624a0.

Walsh, F. R., and M. D. Zoback (2015), Oklahoma's recent earthquakes and saltwater disposal, *Sci. Adv.*, *1*(June), 1–9, doi:10.1126/sciadv.1500195.

Walsh, F. R., and M. D. Zoback (2016), Probabilistic assessment of potential fault slip related to injection-induced earthquakes: Application to north-central Oklahoma, USA, *Geology*, *44*(12), 991–994, doi:10.1130/G38275.1.

Way, H. S. K. (1983), Structural study of the Hunton Lime of the Wilzetta Field, T12–13N, R5E, Lincoln County, Oklahoma, pertaining to the exploration for hydrocarbons [M.S. thesis]: Stillwater, Oklahoma State University, Oklahoma State University.

Wells, D. L., and K. J. Coppersmith (1994), New Empirical Relationships among Magnitude, Rupture Length, Rupture Width, Rupture Area, and Surface Displacement, *Bull. Seismol. Soc. Am.*, *84*(4), 974–1002.

Wu, Q., and M. C. Chapman (2016), Stress drop and source scaling of recent earthquake sequences across the United States, *Seismol. Res. Lett.*, *88*(1), 224–262, doi:10.1785/0220160205.

Yeck, W. L., M. Weingarten, H. M. Benz, D. E. McNamara, E. A. Bergman, R. B. Herrmann, J. L. Rubinstein, and P. S. Earle (2016a), Far-field pressurization likely caused one of the largest injection induced earthquakes by reactivating a large preexisting basement fault structure, *Geophys. Res. Lett.*, *43*(19), 10,198-10,207, doi:10.1002/2016GL070861.

Yeck, W. L., G. P. Hayes, D. E. McNamara, J. L. Rubinstein, W. D. Barnhart, P. S. Earle, and H. M. Benz (2016b), Oklahoma experiences largest earthquake during ongoing regional wastewater injection hazard mitigation efforts, *Geophys. Res. Lett.*, doi:10.1002/2016GL071685.

Yeck, W. L., G. P. Hayes, D. E. McNamara, J. L. Rubinstein, W. D. Barnhart, P. S. Earle, and H. M. Benz (2016c), Oklahoma experiences largest earthquake during ongoing regional wastewater injection hazard mitigation efforts, *Geophys. Res. Lett.*, (September 2016), 711–717, doi:10.1002/2016GL071685.

Yenier, E., G. M. Atkinson, and D. F. Sumy (2017), Ground Motions for Induced Earthquakes in Oklahoma, , *107*(1), doi:10.1785/0120160114.

Zoback, M. D., and H.-P. Harjes (1997), Injection-induced earthquakes and crustal stress at 9 km depth at the KTB deep drilling site, Germany, *J. Geophys. Res.*, *102*(B8), 18477, doi:10.1029/96JB02814.

Zoback, M. D., and S. Hickman (1982), In situ study of the physical mechanisms controlling induced seismicity at Monticello Reservoir, South Carolina, *J. Geophys. Res. Solid Earth*, *87*(B8), 6959–6974, doi:10.1029/JB087iB08p06959.